



저작자표시 2.0 대한민국

이용자는 아래의 조건을 따르는 경우에 한하여 자유롭게

- 이 저작물을 복제, 배포, 전송, 전시, 공연 및 방송할 수 있습니다.
- 이차적 저작물을 작성할 수 있습니다.
- 이 저작물을 영리 목적으로 이용할 수 있습니다.

다음과 같은 조건을 따라야 합니다:



저작자표시. 귀하는 원저작자를 표시하여야 합니다.

- 귀하는, 이 저작물의 재이용이나 배포의 경우, 이 저작물에 적용된 이용허락조건을 명확하게 나타내어야 합니다.
- 저작권자로부터 별도의 허가를 받으면 이러한 조건들은 적용되지 않습니다.

저작권법에 따른 이용자의 권리는 위의 내용에 의하여 영향을 받지 않습니다.

이것은 [이용허락규약\(Legal Code\)](#)을 이해하기 쉽게 요약한 것입니다.

[Disclaimer](#) 

공학박사 학위논문

유기물 활물질을 활용한 고성능
레독스 흐름 전지 개발에 관한 연구

**Exploitation of redox-active organic materials for the
development of high performance redox flow
batteries**

2021 년 8 월

서울대학교 대학원

재료공학부

권 기 윤

유기물 활물질을 활용한 고성능 레독스 흐름
전지 개발에 관한 연구

**Exploitation of redox-active organic materials for the
development of high performance redox flow batteries**

지도 교수 강 기 석

이 논문을 공학박사 학위논문으로 제출함

2021 년 8 월

서울대학교 대학원

재료공학부

권 기 윤

권기윤 의 박사 학위논문을 인준함

2021 년 6 월

위 원 장	<u>이 동 환</u>
부위원장	<u>강 기 석</u>
위 원	<u>김 성 재</u>
위 원	<u>김 진 영</u>
위 원	<u>유 지 상</u>

Abstract

Exploitation of redox-active organic materials for the development of high performance redox flow batteries

Giyun Kwon

Department of Materials Science and Engineering

College of Engineering

The Graduate School

Seoul National University

Ever-growing demand for the sustainable energy resources is becoming one of the biggest global interests to this date due to the environmental concerns from the use of fossil fuel. However, their intermittent energy supply is clearly limiting the efficient utilization of the resources, thus the large-scale energy storage systems (ESSs) should be paired for round-the-clock energy accessibility. Among many ESSs, redox flow battery (RFB), utilizing energy-bearing liquid electrolytes, has gained significant attention because of its smart architecture; the spatial separation of electrolyte reservoir and battery cell allows power and energy to be decoupled, enabling to flexible control of the scale as needed. Therefore, substantial progress has been made in RFB fields for the application of ESSs.

In particular, the research on redox-active material for RFBs is believed to be significantly crucial since it has a major impact on the battery performances. In this regard, beginning with Fe/Cr redox couple, various types of redox-active

materials have been extensively investigated for the last decades. Representatively, V- and Zn/Br-based redox-active materials have shown great promise in research fields, and they have begun to be employed in the practical applications as well. Nevertheless, the use of these redox-active inorganic materials causes environmental concerns and cost issues. In addition, it is also claimed that they almost reach their theoretical limits (*i.e.* limited solubility and redox potential), thus the introduction of new redox chemistry is highly needed for the development of the high performance RFBs. Therefore, research trends in RFBs are moving forward to utilize sustainable and environmentally benign redox-active organic materials (ROMs).

As redox-active materials for RFBs, ROMs possesses differentiated advantages compared to conventional ones. ROMs are potentially cost effective and environmentally friendly since they are mainly composed of earth abundant elements such as C, H, O, and N. Furthermore, tuning various physical properties, such as solubility and redox potential, is feasible through the organic synthesis, which offers the diversification of redox-active material selection and a great promise for high performance RFBs. Despite the novel advantages, the researches on the organic RFBs are infancy and their battery performances are still far behind conventional RFBs.

Therefore, research on a new ROM design strategy is highly required in order to catch up or outperform the conventional RFBs and eventually demonstrate the practically feasible systems. Herein, I suggest strategies of enhancing battery performances by exploiting novel ROMs. To achieve high energy density as an effective way, a multi-redox molecule is introduced into RFB systems, which is designed by inspiration of bio-systems. Differentiated from the conventional ROMs which are capable of single electron redox reaction, the use of multi-redox molecule enables double capacity at the given concentration and its validity is successfully

proven by customized flow cell followed by the systematic analysis. Furthermore, molecular tuning for the solubility enhancement is conducted by reasonably introducing flexible side chains, which shows great promise for the practically feasible system. In the aspect of cycling performance, a ROM with many resonance structures, which is effective for charge distribution, is investigated for highly durable RFBs. Lastly, the fundamental understanding of the electrochemical reactions in organic RFBs is carried out with *in-operando* visualization technique. These researches of various design strategies of ROMs along with the in-depth understanding is believed to provide research insight to extensively broaden the research area.

Keywords: Rechargeable batteries, Redox flow batteries, Redox-active organic materials, Organic redox flow batteries, Electrochemistry

Student Number: 2016-20765

Contents

List of Figures	ix
-----------------------	----

Chapter 1. Introduction	1
1.1. Research motivation and objectives	1
1.2 Research history based on redox-active materials for RFBs	4
1.3 Scope and aim of Thesis	6

Chapter 2. Demonstration of high energy density organic redox flow batteries exploiting novel multi-redox molecules	8
2.1 Novel strategy of exploiting a multi-redox molecule in organic redox flow batteries	8
2.1.1 Research background	8
2.1.2 Experimental method	12
2.1.2.1 Preparation of materials	12
2.1.2.2 Characterization	12
2.1.2.3 Electrochemical measurements	12
2.1.2.4 Computational details	14
2.1.3 Results and discussions	15

2.1.3.1 A multi-redox molecule, DMPZ	15
2.1.3.2 Investigation of the electrochemical kinetics of DMPZ/FL ..	18
2.1.3.3 Cycling of the DMPZ/FL flow cell.....	22
2.1.3.4 The colour change of DMPZ for the estimation of the state of charge	32
2.1.4 Concluding remarks.....	40
2.1.5 References.....	41
2.2 Enhancement of energy density through the molecular modification.....	48
2.2.1 Research background.....	48
2.2.2 Experimental method.....	52
2.2.2.1 Preparation of materials	52
2.2.2.2 Synthesis and characterization.....	52
2.2.2.3 Electrochemical measurements	52
2.2.2.4 Computational details	57
2.2.3 Results and discussions.....	58
2.2.3.1 Bio-inspired redesign of catholyte material.....	58
2.2.3.2 Characterization of BMEPZ catholyte	66
2.2.3.3 Electrochemical performance of BMEPZ/FL flow cell	76
2.2.4 Concluding remarks.....	86
2.2.5 References.....	87

Chapter 3. Rational design of an organic material with exceptional chemical stability for highly stable organic redox

flow batteries	95
3.1 Research background	95
3.2 Experimental method	98
3.2.1 Preparation of materials and characterization	98
3.2.2 Electrochemical measurements	99
3.2.3 Computational details	100
3.3 Results and discussions	102
3.3.1 Design of TPA derivative for a stable catholyte (3MTPA)	102
3.3.2 Kinetic properties of 3MTPA catholyte	108
3.3.3 Stability of 3MTPA in the charged state	112
3.3.4 Performance of 3MTPA under high temperature.....	115
3.3.5 Long-term flow cell performance of 3MTPA	118
3.4 Concluding remarks	124
3.5 References	125

**Chapter 4. In-depth understanding of redox flow battery
through in-operando visualization technique**

4.1 Research background	133
4.2 Experimental method	137
4.2.1 Fabrication of cell and preparation of materials	137
4.2.2 Electrochemical measurements	138
4.2.3 Numerical model details	139
4.3 Results and discussions	144

4.3.1 Concept of microfluidic membrane-free RFB (MFRFB)	144
4.3.2 In-operando visualization of mass- and charge-transfer in MFRFB	146
4.3.3 Electrokinetic analysis of MFRFB for mass- and charge-transfer..	150
4.3.4 Enhancing battery performance by the redesign of the electrode geometry	155
4.4 Concluding remarks	158
4.5 References	159

Chapter 5. Conclusion..... 165

Chapter 6. Abstract in Korean 168

List of Figures

Figure 1.1. Schematic configuration of RFB on discharge and charge process.
.....7

Figure 2.1. Electrochemical reaction of DMPZ and FL. a) Molecular structures and redox mechanisms of DMPZ and FL. b) Schematic illustration of energy storage in DMPZ/FL flow battery and cell configuration. c) CV curves of 10 mM ROMs in supporting electrolyte of 0.1 M LiTFSI in MeCN at a scan rate of 100 mV s⁻¹: DMPZ (green line), FL (orange line), mixture of FL and DMPZ (blue line). 17

Figure 2.2. Electrochemical kinetics of DMPZ, DMPZ⁺, and FL from RDE studies with 1.0 mM ROMs in 0.5 M LiTFSI in MeCN. a) Linearly fitted Levich plots of limiting current (*i_L*) as a function of the square root of the rotation rates ($\omega^{-1/2}$). b), Linearly fitted plots of logarithm of kinetics-controlled current ($\log i_k$) vs. overpotential (η). c) Kinetic parameter comparison for typical redox-active materials in RFB system in terms of the kinetic rate constant (*k₀*) and diffusion coefficient (*D*): this work (orange stars) and reported RFBs (green circles).20

Figure 2.3. LSV curves of a) DMPZ, b) DMPZ⁺, and c) FL for rotation rates of 300–1500 rpm at a scan rate of 5 mV s⁻¹. Linearly fitted Koutecky–Levich plots at various overpotentials for d) DMPZ, e) DMPZ⁺, and f) FL.21

Figure 2.4. Electrochemical performance of DMPZ/FL flow cell. a) Cell voltage vs. time for 1st and 10th cycles at 20 mA cm⁻². b) Energy comparison of typical redox-

active materials in RFB; the dashed area denotes the contribution of the 2nd redox reaction. * The energy density of the positive electrode compartment (energy density per volume) is determined by the intrinsic redox activity of the molecule (energy density per mole) and its solubility in the solvent (mole per volume). In order to emphasize the importance of the multi-redox reaction with respect to enhancing the intrinsic redox activity of molecules, we used the term ‘energy density per mole’ here instead of ‘energy density per volume’. Our intention is to decouple the engineering the intrinsic redox activity and the solubility. c) Cycling efficiencies and capacities with respect to cycle number. d) Molecular orbital energies of ROMs and MeCN. Note that the energy states of DMPZ change with the oxidation due to the relaxation effect of the molecules.26

Figure 2.5. Cell voltage vs. time curves for the first 10 cycles at 20 mA cm⁻², which showed the same electrochemical behavior in cycling.28

Figure 2.6. *Ex situ* Raman analysis of DMPZ in the positive electrode compartment demonstrating the reversible appearance and disappearance of several peaks. The vibrational modes corresponding to these peaks play important roles in the redox reaction of DMPZ.29

Figure 2.7. Cycling efficiencies and capacities with respect to cycle number for the electrolytes (13 mL on each side) containing FL (20 mM) and DMPZ (10 mM) in the supporting electrolyte of 0.5 M LiTFSi in MeCN. The current density of 20 mA cm⁻² was applied and the theoretical capacity is 0.54 A h L⁻¹.30

Figure 2.8. UV-vis spectra of DMPZ⁺ in the electrolytes of the positive electrode

compartment at the SOC 50, captured at 0, 2, 6 and 24 h after sampling. The colour and absorption spectra show little change over 24 hours.31

Figure 2.9. Prediction of SOC. Analysis of colour changes of DMPZ as a function of the SOC using UV–vis spectroscopy; the dotted arrows point to the corresponding colours of the electrolytes in the positive electrode compartment. Four pieces of Celgard 4560 were used to minimize the crossover and accurately measure the SOC, resulting in CE of >99%.34

Figure 2.10. Linearly fitted plot of the absorbance of the peaks at 521 and 660 nm as a function of the SOC. Before SOC 50, the intensity of the peak at 660 nm linearly increased as the green colour became deeper and the DMPZ^+ concentration increased. After SOC 50, the peak intensity at 660 nm reversibly decreased and the peak intensity at 521 nm rapidly increased as the dark green colour changed to red and DMPZ^+ was oxidized to DMPZ^{2+}35

Figure 2.11. Plot of the average discharge voltage as a function of the current density for different mean linear flow velocities. As the current density increases, the cell polarization is getting worse. While there is no distinct difference at the low current densities, faster mass transport leads to much lower cell polarization at the high current densities.36

Figure 2.12. Cycling efficiencies and capacities with respect to cycle number using asymmetric cycling with 100 mA cm^{-2} on charging and 20 mA cm^{-2} on discharging. Widened voltage cut off of 0.5 V and 2.8 V was used to activate the second redox reaction due to the high polarization. Despite the high current density of 100 mA

cm⁻², material utilization of >70% was achieved at the first cycle.37

Figure 2.13. Representative charge-discharge curves for DMPZ/FL flow cell with coulombic and energy efficiencies at different concentrations. The capacity is proportional to the concentration of the active material. As the concentration increases, coulombic efficiency is slightly decreased because more crossover of the active material occurs at longer cycling times.38

Figure 2.14. Volumetric energy density comparison of typical redox-active organic materials in nonaqueous RFB. Li hybrid organic RFB exhibits the highest energy density based on high cell voltage and concentration. Among all organic RFB, DBMMB/FL redox couple shows the highest values. Despite the half concentration, DMPZ/FL redox couple exhibits the same energy density with TEMPO/MePh redox couple, indicating multi-redox molecule has a great potential on high energy density RFB after its solubility is improved.39

Figure 2.15. A new multi-electron redox catholyte material with enhanced solubility, BMEPZ. a) The rational molecular design strategy of BMEPZ inspired by biological redox systems. b) Schematic illustration of all-organic full-flow battery containing BMEPZ/FL electrolytes and CV curves of the redox couple at a scan rate of 100 mV s⁻¹.62

Figure 2.16. Redox core structures and reaction mechanisms of the phenazine biomolecules: a) methanophenazine, b) pyocyanin, and c) DMPZ. Redox potential of DMPZ vs. NHE was linearly converted using ferrocene/ferrocenium redox couple as an internal reference of 0.66 V vs. NHE.63

Figure 2.17. Synthetic route of BMEPZ.	64
Figure 2.18. CV curves of the ROMs at a scan rate of 100 mV s ⁻¹ : DMPZ (gray line), BMEPZ (pink line), FL (purple line), and the mixture of BMEPZ and FL with ferrocene as an internal reference (blue line).	65
Figure 2.19. Characterization of BMEPZ. a) Representative charge–discharge curve for bulk-electrolysis test of BMEPZ. b) Coulombic efficiencies and capacities for bulk-electrolysis test of BMEPZ with respect to cycle number. c) Linearly fitted Levich plots of limiting current (<i>i</i> _L) as a function of the square root of the rotation rate ($\omega^{-1/2}$). d) Linearly fitted plots of logarithm of kinetics-controlled current (log <i>i</i> _k) as a function of overpotential (η). e) Comparison of kinetic parameters (kinetic rate constant (<i>k</i> ₀) and diffusion coefficient (<i>D</i>)) of reported redox-active materials in RFB system: this work (blue stars) and reported RFBs (pink circles).	70
Figure 2.20. LSV curves of a) BMEPZ and b) BMEPZ ⁺ for rotation rates of 300–1500 rpm at a scan rate of 5 mV s ⁻¹ . Linearly fitted Koutecký-Levich plots of c) BMEPZ and d) BMEPZ ⁺ at various overpotentials.	71
Figure 2.21. Scan-rate dependence CV study for a) BMEPZ and b) FL, and Randles-Sevcik plot of c) BMEPZ and d) FL.	72
Figure 2.22. Investigation of redox mechanism of BMEPZ. a) <i>Ex situ</i> Raman analysis for BMEPZ in catholyte, demonstrating the reversible appearance and disappearance of several peaks. b) NPA of BMEPZ, BMEPZ ⁺ , and BMEPZ ²⁺ . The depth of the pink color denotes the extent of the charge change. c) Molecular geometries of BMEPZ, BMEPZ ⁺ , and BMEPZ ²⁺	73

Figure 2.23. Charge distribution calculations of BMEPZ, BMEPZ ⁺ , and BMEPZ ²⁺ using natural population analysis (NPA).	74
Figure 2.24. Frontier molecular orbital (FMO) energies of BMEPZ, BMEPZ ⁺ , BMEPZ ²⁺ , and MeCN. Note that the energy states of BMEPZ change with the oxidation due to the relaxation effect of the molecules.	75
Figure 2.25. Electrochemical performance of flow cell of 50 mM BMEPZ and 0.1 M FL. a) Representative cell voltage vs. time profile at a current density of 20 mA cm ⁻² . The inset shows the color change of the catholyte as a function of the SOC. b) Cycling efficiencies and capacities with respect to cycle number.	80
Figure 2.26. UV-vis spectra corresponding to the colors of the BMEPZ catholyte at the given SOCs.	81
Figure 2.27. Charge–discharge curves for 0.05 M BMEPZ and 0.1 M FL with respect to the cycle number.	82
Figure 2.28. UV–vis spectra of BMEPZ ⁺ in the catholyte at the SOC 50, obtained at 0, 12, and 24 h after sampling. The color and spectra of the catholyte solution are well maintained over 24 hours.	83
Figure 2.29. Electrochemical performance of BMEPZ/FL flow cell at high concentrations. a) Typical charge–discharge curves at different concentrations. b) Cycling efficiencies and capacities for 0.1 M BMEPZ and 0.2 M FL with respect to cycle number. c) Cycling efficiencies and capacities for 0.4 M BMEPZ and 0.8 M FL with respect to cycle number. d) Energy density plot of typical redox-active materials in organic RFBs. The molar energy density is the volumetric energy density	

divided by the cycling concentration. 84

Figure 2.30. ^1H - (top) and ^{13}C -NMR (bottom) spectra of BMEPZ in C_6D_6 . 85

Figure 3.1. Synthetic route of 3MTPA. In a flame-dried two-necked round bottom flask, *p*-anisidine (1.00 g, 8.12 mmol), 4-bromoanisole (3.80 g, 20.3 mmol), sodium tert-butoxide (1.95 g, 20.3 mmol), and bis(tri-tert-butylphosphine)palladium(0) (80.0 mg, 0.16 mmol) were dissolved in freshly distilled toluene (30 ml). The solution was refluxed and stirred overnight. After cooling to room temperature, the reaction mixture was poured into water and extracted three times with dichloromethane. The organic layer was dried over anhydrous MgSO_4 and purified by column chromatography on silica gel with ethyl acetate/*n*-hexane (1:19 v/v) as an eluent. Recrystallization from methanol afforded a yellow powder. Yield: 73% (2.00 g), ^1H -NMR (500 MHz, CDCl_3) δ (ppm): 6.96 (s, 6H), 6.79 (d, $J = 8.5$ Hz, 6H), 3.77 (s, 9H); ^{13}C -NMR (125 MHz, CDCl_3) δ (ppm): 115.12, 142.10, 125.03, 114.69, 55.71; HRMS (EI): calc. for $\text{C}_{42}\text{H}_{27}\text{N}_3\text{O}_3$ (M^+), 335.1521; found, 335.1517 104

Figure 3.2. Highly stable catholyte 3MTPA. a) Resonance structures of 3MTPA. b) HOMO/LUMO and SOMO plots for 3MTPA and 3MTPA^+ , respectively, with isovalue of 0.02 (the green and red colors denote opposite signs of the wave function). c) Molecular orbital energies of 3MTPA, 3MTPA^+ , and MeCN. d) CV curve of 3MTPA at a scan rate of 100 mV s^{-1} 105

Figure 3.3. Molecular orbital plots for the representative ROMs, MEEPT and

TEMPO. Note that there are noticeable changes of molecular orbitals and geometric structures for the redox reactions, as indicated by arrows and circles. 106

Figure 3.4. CV curve of TPA at the scan rate of 100 mV s^{-1} , exhibiting irreversible redox reaction of TPA. 107

Figure 3.5. Kinetic study of 3MTPA. a) LSV curves of 3MTPA for various rotation rates. b) Linearly fitted Levich plots of limiting current (i_L) in terms of the square root of the rotation rate ($\omega^{-1/2}$). c) Linearly fitted plots of logarithm of kinetics-controlled current ($\log i_k$) as a function of overpotential (η). d) Comparison of kinetic parameters of reported redox-active materials in RFB system for the kinetic rate constant (k_0) and diffusion coefficient (D): this work (yellow stars) and reported RFBs (green circles). e) Molecular geometries of 3MTPA and 3MTPA⁺ with reorganization energy (λ). 110

Figure 3.6. Linearly fitted Koutecký-Levich plots of 3MTPA with respect to the overpotentials. 111

Figure 3.7. Investigation of chemical stability of 3MTPA in the charged state. a) Illustration of experimental procedures for storage of the charged species. Charge/discharge curves of symmetric cell using typical ROMs with/without b) 24 h or c) 168 h storage of charged species. d) Flow cell cycling of 10 mM 3MTPA at a current density of 20 mA cm^{-2} with 24 h rest in the middle of 100 cycles. . 114

Figure 3.8. Redox behavior of 3MTPA under high temperature. a) Charge/discharge curves of symmetric cell using typical ROMs with/without 168 h storage of charged species at a high temperature of 50°C . b) Rate capability of

3MTPA at a high temperature of 50°C.	116
Figure 3.9. Completely soluble 2.0 M 3MTPA in MeCN at the high temperature of 50°C.	117
Figure 3.10. Electrochemical performance of flow cell using 3MTPA. a) Schematic illustration of symmetric flow battery exploiting 3MTPA. b) Representative charge/discharge curve for 0.05 M 3MTPA at current density of 60 mA cm ⁻² . c) Cycling efficiencies and capacities for 0.05 M 3MTPA with respect to cycle number. d) Typical electrochemical profile for 0.3 M 3MTPA at current density of 100 mA cm ⁻² . e) Cycling efficiencies and capacities for 0.3 M 3MTPA with respect to cycle number. f) Charge/discharge curves for 0.3 M 3MTPA at current densities from 40 to 140 mA cm ⁻² . g) Flow cell cycling performance plot of typical redox-active materials in ORFBs.	120
Figure 3.11. 500 MHz ¹ H-NMR spectrum of 3MTPA in CDCl ₃	122
Figure 3.12. 125 MHz ¹³ C-NMR spectrum of 3MTPA in CDCl ₃	123

Figure 4.1. a) The microscale fabrication process of the MFRFB device. b) The photo of assembled MFRFB device connected to electrical source. c) The microscopic view of observation area for current study.	145
--	-----

Figure 4.2. Kinetic study of 3MTPA. a) The cyclic voltammetry of multi-redox couple. b) Voltage and capacity profile of BMEPZ in terms of charge transfer. c) In-operando visualization of electrochemical reaction in terms of charge transfer. d)	
--	--

Voltage and capacity profile of BMEPZ in terms of mass transfer. e) In-operando visualization of electrochemical reaction in terms of mass transfer. 149

Figure 4.3. a) Schematic of MFRFB and theoretical regions that affect battery performance. b) Numerical results of concentration profiles of BMEPZ for single redox reaction. c) Numerical results of concentration profiles of BMEP for multi-redox reaction. d) Image of scaling analysis for concentration boundary layer of BMEPZ²⁺ at 10 μ L/min and 0.14 mA. e) Comparison of experimental, numerical and analytical slopes of concentration boundary layer relation. 154

Figure 4.4. a) Comparison of electrochemical performance with respect to the geometric configuration of electrode. b) Phase diagram of required flow rate depending on the aspect ratio of cell for various active-materials in RFBs with corresponding diffusion coefficients. 157

Chapter 1. Introduction

1.1 Research motivation and objectives

With ever-increasing global commitment to mitigate climate change, combined with rapid developments in certain critical technologies, it is believed that a global transition from fossil fuel to renewable energy is inevitable. The fossil fuel, at the same time, is still the vast majority source of the world's produced electricity. Although the sustainable energy sources, such as solar and wind, are becoming increasingly affordable and extensively deployed, they are acutely required the combination of reliable and cost-effective energy storage system (ESS) to mitigate their intermittency and achieve the round-the-clock energy supply. Among several energy conversion and storage technologies, the choice of rechargeable batteries, which show high energy efficiency, can be natural based on their great success in powering portable electronic devices. Redox flow batteries (RFBs), in particular, have been considered suitable for grid storage because of its clever architecture.

Differentiated from the conventional batteries, RFB is a liquid-type battery system, utilizing energy-bearing liquid electrolytes in which redox-active materials are dissolved. As shown in Figure 1.1, it is composed of three parts of cell, reservoirs, and pumps; the liquid electrolytes are pumped from the external reservoirs through the cell where electrodes are separated by membrane. Notably, the electrochemical reaction usually occurs on the electrode surface without damaging the internal structure, thus making it more suitable for long life cycling. Furthermore, the

independent control of the energy capacity (reservoir size) and the power rating (the active area inside stacks) based on the unique architecture of RFBs enables significant advantages such as excellent scalability, flexible modular design, effective thermal management, and better ensured security, which makes RFBs suitable for economically viable EES applications.

In this regard, there has been a rapid increase in the volume of research on RFBs. Most studies, especially, have focused on redox-active materials that majorly determine the battery performances and great progress has been achieved for last decades. Nevertheless, there are still numerous challenges, including cost and environmental issues for inorganic-based RFBs or unsatisfied electrochemical performances of organic-based RFBs. The aim of this dissertation is to present various strategies to develop high-performance RFBs by addressing limitations from the redox-active materials accompanied by the in-depth understanding of RFB technology.

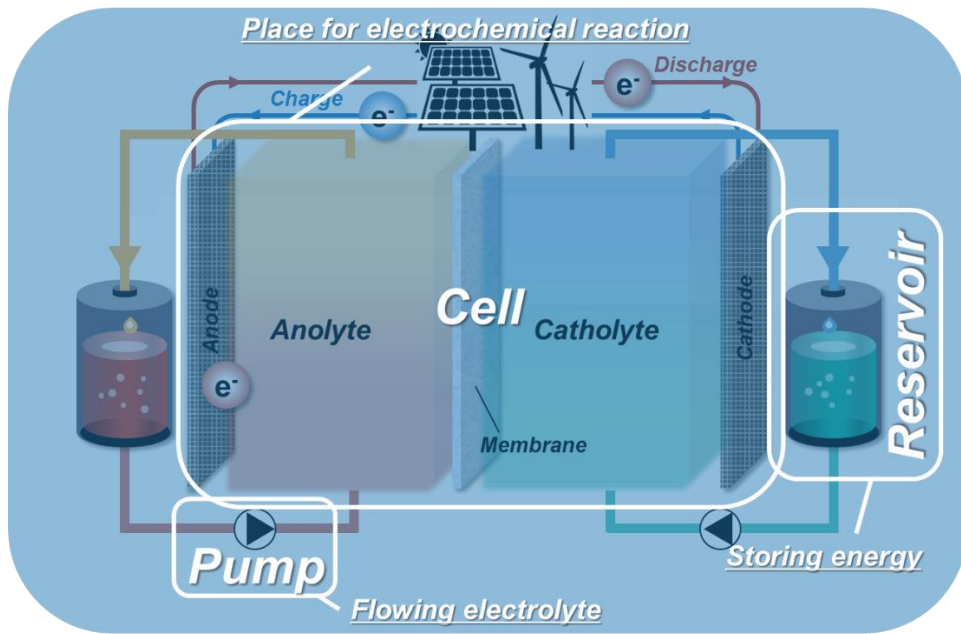


Figure 1.1. Schematic configuration of RFB on discharge and charge process.

1.2 Research history based on redox-active materials for RFBs

Among numerous components of RFB, the exploration of redox-active material with high reversibility, which has major impact on the battery performances, is thus believed to be at the heart for developing advanced RFB technology. In this regard, beginning with Fe/Cr-based RFB developed by NASA, various redox couples have been extensively investigated for last decades. Representatively, all vanadium-based RFBs (VRFBs), exploiting the four different oxidation states, and Zn/Br-based RFBs begin to be deployed for commercial application due to their decent battery performance. However, the high system cost and relatively low energy density of VRFBs are still unsatisfactory. In addition, there are still remaining challenges for Zn/Br-based RFBs, including dendrite growth, slow kinetics, and safety issues. Therefore, the investigation of new redox chemistry can be an alternative opportunity to overcome the limitations in the conventional RFBs.

In the very recent years, redox-active organic materials (ROMs) have drawn intense research attention for the development of next-generation RFBs. Among countless organic materials, ROMs are organic materials that can undergo reversible redox reaction via conjugated molecular structure accompanied by the change of charge states, and, in a simple way, most ROMs are classified into two intrinsic types of p- and n-type according to their redox behaviors; the p-type corresponds to the ROM that undergoes oxidation first, and the n-type corresponds to the ROM that undergoes reduction first. Different from the inorganic-based redox-active materials, such ROMs possess novel advantages for the application of RFBs.

Generally, organic RFBs (ORFBs) are potentially green, safe, and cost-effective systems because they are mainly composed of earth-abundant elements such as C, H, O, and N. Moreover, while the theoretical performance limits are almost reached in the conventional RFBs, the use of ROMs presents tremendous potential and design flexibility with a diverse range of molecular structures and their corresponding electrochemical mechanisms. Most importantly, ROMs present significant leeway in overall RFB design as needed, since their chemical tunability through the organic synthesis enables the flexible control of various physical properties such as redox potential and solubility, which directly affects electrochemical performances. Despite their great potentials of ROMs, the research of ORFBs are still infancy and there are faced problems to be addressed such as relatively low energy density and cycle performance.

1.3 Scope and aim of Thesis

In this study, I suggest various design strategies of exploiting novel ROMs for the demonstration of high-performance ORFBs beyond conventional inorganic-based RFBs. Here, I present rationally designed ROMs to effectively address remaining challenges in ORFBs and their applicability is evaluated based on the combined study of various electrochemical analysis and computational method. Moreover, fundamental understanding of reaction mechanism of RFB is conducted using novel ROM and advanced analysis technique under consideration of electrochemistry and hydrodynamics.

Chapter 2 excavates the exploitation of novel multi-electron-redox molecules as a new class of ROMs for the dramatic enhancement of energy density in ORFBs. The use of multi-electron-redox material in RFB is the ideal choice because it can boost capacity without deteriorating other properties such as viscosity and ionic conductivity of electrolyte. 5,10-dihydro-5,10-dimethylphenazine (DMPZ) is rationally designed inspired by the double-electron redox activity of phenazine derivative in the bio-system. The applicability of reversible double-redox activity in RFB system is verified using customized flow cell accompanied by the redox mechanism of DMPZ. Moreover, the further engineering of solubility is carried out to enhance the energy density by introducing flexible side chains. Therefore, multi-electron redox molecule with the desirable solubility, 5,10-bis(2-methoxyethyl)-5,10-dihydrophenazine (BMEPZ), is successfully synthesized, which is recorded one of the highest energy density among reported ORFBs.

Chapter 3 describes molecular design with high chemical stability in all charged states for the development of highly durable ORFBs. Highly reactive radical species which is generated during redox reactions is believed to induce significant deterioration of the system stability. To prevent undesirable side reaction resulted from the high charge density localized on a few atoms in the molecule, the delocalization of charge via whole molecular skeleton is effective. I focused on triphenylamine (TPA) motif, whose charge state can be significantly delocalized because of its large conjugation area and many resonance structures. Furthermore, three methoxy chains are introduced to para-position of TPA (*i.e.* 3MTPA), to block the additional dimerization. The great stability of 3MTPA is evaluated for the charged state storage experiments, and long-term flow cell cycling is successfully demonstrated without noticeable capacity degradation.

Chapter 4 represents the fundamental understanding of RFB system using novel ROM with advanced analysis technique. Since electrochemistry and hydrodynamics should be considered for understanding of the RFB system, the direct observation of various phenomena occurring during battery operation is critically required. *In-operando* visualization of electrochemical reaction during battery operation is demonstrated using transparent microfluidic cell. Especially, the use of DMPZ which undergoes reversible two-stage of color changes depending on the charge states enables the visual analysis in terms of charge- and mass-transfer. Moreover, the in-depth understating based on the combined study of numerical and analytical analysis presents the rational cell geometry design.

Chapter 2. Demonstration of high energy density organic redox flow batteries exploiting novel multi-redox molecules

2.1 Novel strategy of exploiting a multi-redox molecule in organic redox flow batteries

(The essence of this chapter has been published in *Joule*. Reproduced with permission from [Kwon, G. *et al.*, *Joule* **2018**, 2, 1771-1782] Copyright (2018) Elsevier)

2.1.1 Research background

Concerns over fossil fuel depletion and greenhouse gas emissions have led to a high demand for sustainable energy resources such as solar and wind power in recent years; however, their full utilization in electric generation is partly limited by the intermittent nature of their supply.^{1,2} To overcome this issue, large-scale energy storage systems (ESSs) are needed, with rechargeable batteries being considered the most affordable choice.³ Among rechargeable batteries, redox flow batteries (RFBs) have received intense interest as one of the most attractive candidates for these applications because of their easy scale-up combined with cost-effectiveness and design flexibility that can decouple power and energy for diverse purposes.⁴⁻¹⁰ In

particular, recent developments with non-aqueous systems employing redox-active organic materials (ROMs) have provided a path toward the development of high-energy-density RFBs, while conventional aqueous RFBs have suffered from the low energy density arising from the narrow electrochemical voltage window limited by water electrolysis.^{7,11-13} Moreover, the potential low costs and chemical/structural diversity of ROMs offer improvements over those of transition-metal-based redox active materials such as vanadium, chrome, or zinc commonly used for conventional RFBs.¹⁴⁻¹⁶

Several important high-performance non-aqueous RFBs have been recently reported such as systems based on 2,2,6,6-tetramethyl-1-piperidinyloxy (TEMPO) and 2,5-di-tert-butyl-1-methoxy-4-[2'-methoxyethoxy]benzene (DBMMB), which presented impressively higher energy density and cell voltage (>1.6 V) than transition-metal-based aqueous systems.¹⁷⁻²³ In particular, DBMMB exhibited redox activity at 0.73 V (vs. Ag/Ag⁺) in acetonitrile (MeCN) solvent-based electrolyte, delivering $\approx 60 \text{ W h mol}^{-1}$ when combined with 9-fluorenone (FL), which is the highest value among non-aqueous organic RFBs reported to date.¹⁹ In attempts to achieve higher energy densities, increasing the concentration of these ROMs in the electrolyte has been a general and effective strategy so that it can contain more amount of redox active materials per system volume.^{17,21,24} For instance, Wei *et al.* demonstrated that the energy density of RFBs can be systematically improved by increasing the concentration of TEMPO up to 2.0 M.¹⁷ Milshtein *et al.* successfully showed that the energy density could be further enhanced by tailoring the solubility

of N-ethylphenothiazine in MeCN through chemical modification.²¹ Although this approach of exploiting a high-concentration electrolyte is simple and effective, there are unfavorable trade-offs such as increased electrolyte viscosity and high cell resistance; in addition, it often leads to the precipitation of salts, which causes the failure of the system.^{17,20,25,26} Furthermore, non-aqueous RFBs can be more vulnerable to these trade-offs because of the intrinsically lower ionic conductivity of the non-aqueous electrolyte compared with its aqueous counterparts, which typically results in inferior power capability of the system.^{20,27,28}

Herein, we propose that multi-electron ROMs can offer an alternative route for the preparation of high-energy-density RFBs. Unlike doubling the electrolyte concentration, for instance, which would easily result in the solubility limit being exceeded or significant reduction in the kinetics, the utilization of the double-redox activity from a single ROM would approximately double the energy density without negatively affecting the electrolyte properties. Nevertheless, the use of a second-electron redox reaction in most ROMs has been often shown to be irreversible or to promote severe degradation because of the poor chemical stability of the ROMs at highly oxidized states in the solution.^{20,21} Even though there are a few reports on candidates for multi-redox ROMs in recent years, they have not been demonstrated for full flow cell system.^{29,30} In this work, we introduce a novel multi-electron-redox phenazine molecule, 5,10-dihydro-5,10-dimethylphenazine (DMPZ), as a new class of ROMs for the positive electrode compartment and demonstrate it for all organic flow system. Double-redox activities are observed, with the second-electron redox

potential being one of the highest values reported for ROMs, and these reactions are remarkably reversible in conventional non-aqueous medium for RFBs with fast kinetics and chemical stability, thereby resulting in the highest energy density per mole among RFBs reported thus far.

2.1.2 Experimental method

2.1.2.1 Preparation of materials

DMPZ was purchased from TCI Chemicals (Japan). Bis(trifluoromethane)sulfonimide lithium salt (LiTFSI), MeCN (anhydrous), and FL were purchased from Sigma–Aldrich and used without further purification. The microporous separator (Celgard 4560) was purchased from Wellcos (Korea) and treated under vacuum at 70°C for 24 h to remove moisture.

2.1.2.2 Characterization

To prevent air contamination, all the samples were prepared and sealed in an Ar-filled glove box. The electrolytes containing FL (20 mM) and DMPZ (10 mM) in the supporting electrolyte of 0.5 M LiTFSI in MeCN were used. For the UV–vis spectroscopy analysis, absorption spectra of the electrolytes in the positive electrode compartment (diluted in MeCN, 5% v/v) were obtained using a UV–vis spectrometer (Agilent Technologies, Cary 5000) with an optical glass cuvette (Quartz; Hellma®).

Raman spectra (LabRAM HR Evolution, Horiba) were recorded using capillary tubes (inner diameter of 1.1–1.2 mm) with continuous-wave linearly polarized lasers (wavelengths: 532, 633 nm). The laser beam was focused using a 100× objective lens, resulting in a spot diameter of approximately 1 μm. The acquisition time and number of accumulations were 10 s and 5 s, respectively.

2.1.2.3 Electrochemical measurements

The solutions were prepared and the electrochemical tests were performed in an Ar-filled glove box under an inert atmosphere (<0.5 ppm O₂, H₂O). CVs of FL,

DMPZ, and the mixture of FL and DMPZ (10 mM each) were obtained using a supporting electrolyte of 0.1 M LiTFSI in MeCN. A three-electrode system (Pt counter electrode, Ag/AgNO₃ reference electrode, Au working electrode) was employed with a scan rate of 100 mV s⁻¹.

In the RDE test, a three-electrode system (Pt counter electrode, Ag/AgNO₃ reference electrode, glassy carbon working electrode with 5-mm diameter) was employed for the LSV tests. The DMPZ⁺ solution was prepared from the DMPZ solution under constant-voltage mode at 0.2 V vs. Ag/Ag⁺. The working electrode was rotated from 300 to 1500 rpm (in increments of 300 rpm) using a modulated speed rotator (AFMSRX; PINE). The LSV tests were conducted with 1.0 mM ROMs in 0.5 M LiTFSI in MeCN at a scan rate of 5 mV s⁻¹. The kinematic viscosity (ν) of the 0.5 M LiTFSI in MeCN was measured to be 0.59 mm² s⁻¹ following ASTM D445 in Koptri (Korea). Using the slopes of the linearly fitted Levich plots (Figure 2.2a) and the Levich equation (eq 1), the diffusion coefficients (D) of the ROMs were calculated (the slopes of DMPZ, DMPZ⁺, and FL were determined to be 1.74 × 10⁻⁵, 1.18 × 10⁻⁵, and -1.32 × 10⁻⁵ A rad^{-1/2} s^{1/2}, respectively).

$$i_L = 0.62nFAD^{2/3}\omega^{1/2}\nu^{-1/6}C_0 \quad (1)$$

Here, n is the number of electrons transferred ($n = 1$), F is the Faradaic constant ($F = 96485 \text{ C mol}^{-1}$), A is the electrode area ($A = 0.2 \text{ cm}^2$), and C_0 is the concentration of ROMs ($C_0 = 1.0 \text{ mM}$).

A custom flow cell with backing plates (polyethylene-coated fiber glass), flow fields (polytetrafluoroethylene (PTFE)), and gaskets (PTFE) was fabricated

using materials purchased from ILDO F&C (Korea). The flow cells were assembled with carbon felts (XF30A; TOYOBO, Korea) as electrodes at both the anode and cathode side with two pieces of microporous separators (Celgard 4560) sandwiched in between. The active size of the flow cell was 2.0-cm wide \times 2.0-cm long (4 cm²), and norprene tubing (Masterflex) was used. The electrolytes (13 mL on each side) containing FL (0.1 M) and DMPZ (50 mM) in the supporting electrolyte of 0.5 M LiTFSI in MeCN were flowed through the felt electrodes at a flow rate of 80 mL min⁻¹ using a pump (ShenChen). The uniform volumetric porosity and the height of the carbon felts are 95% and 4.3 mm, and accordingly the mean linear flow velocity of electrolyte past the electrode surface is calculated to be 1.63 cm s⁻¹.^{31,32} Flow cell tests were performed at room temperature in constant-current mode using a battery test system (WBCS 3000; WonA Tech, Korea). The volumetric energy density were calculated based on the electrolyte volume of the positive compartment (13 mL).

2.1.2.4 Computational details

The Gaussian 09 quantum chemistry package³³ was used for spin-unrestricted density functional theory (DFT)-type calculations, which included geometry optimization, energy evaluation, eigenvalue calculation, and vibration mode prediction of the molecules.

2.1.3 Results and discussions

2.1.3.1 A multi-redox molecule, DMPZ

The phenazines are a group of biomolecules involved in the metabolism of living organisms, where various electron-transfer reactions occur, and are capable of performing redox reactions.³⁴⁻⁴⁰ DMPZ, a methylated phenazine at both nitrogen atoms in the pyrazine ring, is known to exhibit reversible two-step reactions of single-electron redox on the diazabutadiene motif in the heterocyclic system.⁴¹⁻⁴³ Inspired by its electrochemical activity not only in aqueous biological systems but also in non-aqueous medium with high redox potential and chemical stability,⁴¹⁻⁴⁴ we explored here the double-redox activities of DMPZ for use as a positive electrode material in RFBs. The molecular structure of the redox DMPZ is presented in Figure 2.1a along with the expected half-cell positive electrode reaction. The figure also shows the half-cell negative electrode reaction of 9-fluorenone (FL), which we employed for preparing an all-organic RFB.¹⁹ Because of the expected multi-redox capability of DMPZ, a molar ratio of 1:2 DMPZ:FL was used in the construction of a flow cell comprising the DMPZ (positive electrode) and FL (negative electrode) using a supporting electrolyte of MeCN,¹⁹ which is schematically illustrated in Figure 2.1b. A microporous membrane was adopted for the mixed electrolyte, in which both DMPZ and FL were dissolved, to alleviate the crossover of the ROMs.^{19,45-47} It should be noted that the low-donor-number MeCN (14.1) was employed in utilizing the multi-electron redox reaction of DMPZ because the reversible second redox reaction of DMPZ was hindered in high-donor-number

solvents such as dimethyl sulfoxide (DMSO, 29.8) with the demethylation reaction.⁴² The electrochemical reaction of the cell begins with DMPZ being first oxidized upon charge (blue arrow), providing two electrons; DMPZ²⁺ is then reversibly reduced to DMPZ during discharge (red arrow).

Cyclic voltammograms (CVs) were obtained for DMPZ and FL to investigate the redox activities and potentials of the redox couple in the MeCN electrolyte. As observed in Figure 2.1c, DMPZ (green line) displays two reversible redox peaks with average redox potentials of -0.15 and 0.61 V vs. Ag/Ag⁺, which are on a par with or higher than those of other reported ROMs, and FL (orange line) exhibits a reversible redox activity with an average potential of -1.39 V (vs. Ag/Ag⁺), which is consistent with previous observations.^{18,21,48,49} It is noteworthy that the second redox potential of 0.61 V (vs. Ag/Ag⁺) for DMPZ is one of the highest values reported for ROMs to date. We obtained an additional CV for the mixture of DMPZ and FL to confirm the compatibility of these two redox species in the electrolyte during oxidation and reduction. The blue line in the CV of Figure 2.1c indicates that DMPZ and FL maintain the same redox potentials with currents equivalent to those of the individual cases, implying the absence of apparent side reactions among DMPZ/DMPZ⁺/DMPZ²⁺ and FL/FL⁻. Based on the CVs, it is expected that a flow battery using a DMPZ/FL couple would harvest high theoretical cell voltages of 1.24 and 2 V.

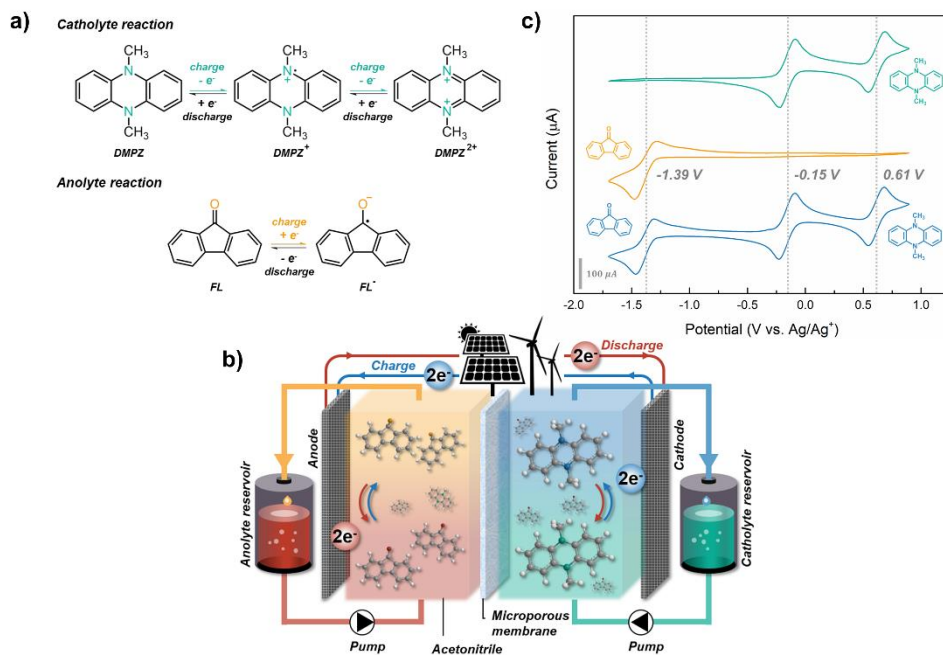


Figure 2.1. Electrochemical reaction of DMPZ and FL. a) Molecular structures and redox mechanisms of DMPZ and FL. b) Schematic illustration of energy storage in DMPZ/FL flow battery and cell configuration. c) CV curves of 10 mM ROMs in supporting electrolyte of 0.1 M LiTFSI in MeCN at a scan rate of 100 mV s⁻¹: DMPZ (green line), FL (orange line), mixture of FL and DMPZ (blue line).

2.1.3.2 Investigation of the electrochemical kinetics of DMPZ/FL

The electrochemical kinetic properties of DMPZ in the electrolyte were examined using a series of rotating disk electrode (RDE) tests, as shown in Figure 2.2. As DMPZ undergoes multi-electron redox reactions, both the DMPZ and DMPZ⁺ species were considered and treated as individual entities in the analysis. The linear sweep voltammetry (LSV) curves for DMPZ, DMPZ⁺, and FL reveal that the mass-transport-controlled limiting currents (i_L) increase with increasing rotation rates (ω) in the range of 300–1500 rpm (Figure 2.3a–c). The mass-transfer-controlled kinetics were then analyzed using the Levich equation, which determines how fast the mass diffuses to the electrode in the Nernst diffusion layer.⁵⁰ From the well-fitted Levich plots, which show the linear relationship between i_L and the square root of ω (Figure 2.2a), the diffusion coefficients (D) of DMPZ, DMPZ⁺, and FL were calculated to be 1.58×10^{-5} , 8.82×10^{-6} , and 1.05×10^{-5} cm² s⁻¹, respectively (a detailed description of the calculations is provided in the electrochemistry section of the Methods). In addition, the charge-transfer-controlled kinetics, which contribute to the reaction rate of the electrode, were investigated using the Koutecky–Levich equation.⁵⁰ The Koutecky–Levich plots at different overpotentials (η) were extrapolated to determine the kinetic-controlled currents (i_k) (Figure 2.3d–f). From the linearly fitted plots of $\log i_k$ vs. the overpotentials in Figure 2.2b, the logarithms of the exchange currents ($\log i_0$) were determined to be -3.25 for DMPZ, -3.98 for DMPZ⁺, and -3.65 for FL, yielding kinetic rate constants (k_0) of 2.97×10^{-2} , 5.53×10^{-3} , and 1.18×10^{-2} cm s⁻¹, respectively. It is worth noting that DMPZ has one of

the highest kinetic rate constants of known ROMs. Figure 2.2c displays both the mass- and charge-transfer-controlled kinetic parameters of DMPZ, DMPZ⁺, and FL (orange stars) on a logarithm scale for comparison with previously reported redox-active materials in RFBs (green closed circles). Notably, the DMPZ/FL couple displayed outstanding kinetic characteristics in terms of both D and k_0 , exceeding those of other species, which implies that the observed fast kinetic parameters would have a positive effect on the cell polarization and energy efficiency, as illustrated later in detail.

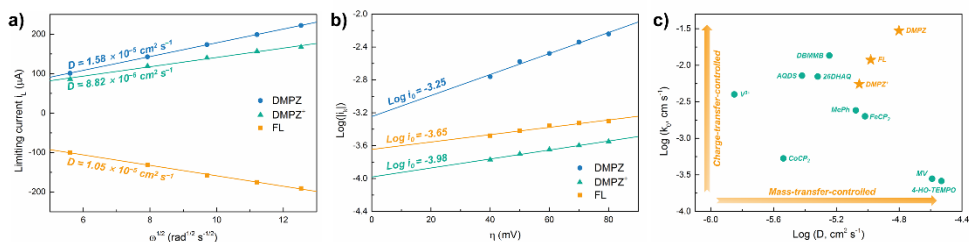


Figure 2.2. Electrochemical kinetics of DMPZ, DMPZ⁺, and FL from RDE studies with 1.0 mM ROMs in 0.5 M LiTFSI in MeCN. a) Linearly fitted Levich plots of limiting current (i_L) as a function of the square root of the rotation rates ($\omega^{-1/2}$). b), Linearly fitted plots of logarithm of kinetics-controlled current ($\log i_k$) vs. overpotential (η). c) Kinetic parameter comparison for typical redox-active materials in RFB system in terms of the kinetic rate constant (k_0) and diffusion coefficient (D): this work (orange stars) and reported RFBs (green circles).

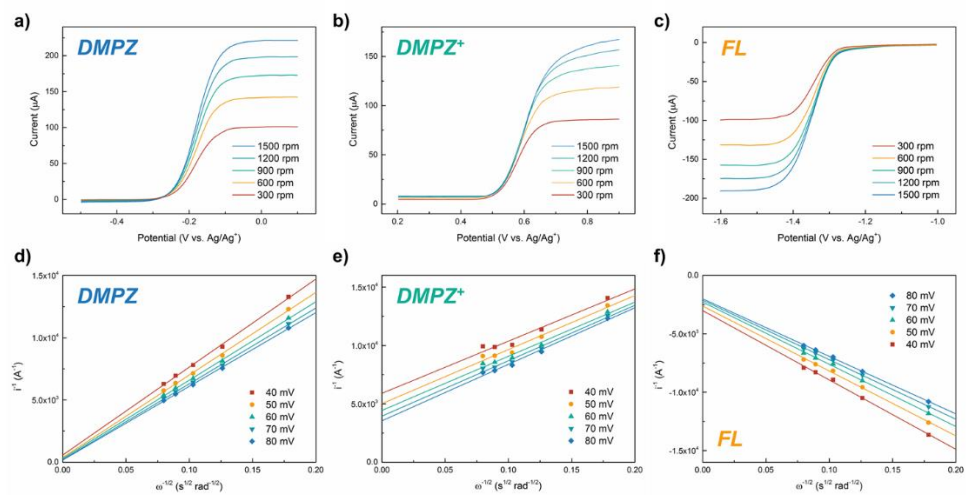


Figure 2.3. LSV curves of a) DMPZ, b) DMPZ⁺, and c) FL for rotation rates of 300–1500 rpm at a scan rate of 5 mV s⁻¹. Linearly fitted Koutecky–Levich plots at various overpotentials for d) DMPZ, e) DMPZ⁺, and f) FL.

2.1.3.3 Cycling of the DMPZ/FL flow cell

The electrochemical performance of flow cells employing a DMPZ positive electrode material and FL negative electrode material was investigated using a custom cell, the design of which is described in the Methods. Figure 2.4a presents representative voltage vs. time curves for the first and tenth cycles at 20 mA cm^{-2} (Figure 2.5). Two well-defined plateaus were observed at 1.2 and 2 V, which are consistent with the CV results in Figure 2.1c. Given the same lengths of the plateaus, it can be inferred that the two single-electron reactions contribute equally to the redox reaction and capacity. The Raman spectroscopy analysis in Figure 2.6 supports the view that the changes in the local bonding of DMPZ are reversible upon charging and discharging. The reversible bonding is associated with the vibrational modes of C–N–C and C=C bonds around the diazabutadiene, in agreement with the reported redox mechanism,⁴² confirming the two-step multi-redox reactions in DMPZ during the flow cell operation (Table S1). To compare the performance of the DMPZ/FL flow cell with that of reported RFBs, the theoretical energy densities of RFBs employing both aqueous and non-aqueous medium are plotted in Figure 2.4b for the same concentration of ROMs. Figure 2.4b shows that DMPZ (vs. FL) presents the highest theoretical and practical energy density among reported redox couples for both aqueous and non-aqueous RFBs, even exceeding those of recently reported RFBs based on DBMMB with the highest energy demonstrated thus far.¹⁹ It is worth noting that for DMPZ, the energy density contributed from the second redox reaction is considerably larger than that contributed from the first redox reaction because of

the higher second redox potential with the same redox capacity, which results in DMPZ outperforming the other materials with respect to the energy density.

Figure 2.4c shows the energy efficiencies and capacity retention of the RFBs employing the DMPZ as a positive electrode material. The flow cell maintained a high coulombic efficiency (CE) of $\approx 90\%$ and a voltage efficiency of 78% over 30 cycles, yielding a respectable energy efficiency (EE) of $\approx 70\%$. Considering the high applied current density of 20 mA cm^{-2} , the observed efficiency indicates rapid kinetics in the electrochemical reaction, which outperforms other non-aqueous flow cells and even comparable to those of some aqueous systems.^{15,18,19,24,51} The fast electrochemical reactions are attributed to the observed high kinetic rate constants (k_0) and diffusion coefficients (D) of the DMPZ and FL, as demonstrated in Figure 2.2. Stable cycling was also achieved for the flow cell without noticeable capacity fading, with retention of $\approx 98\%$ of the initial capacity (2.43 A h L^{-1}) after 30 cycles and capacity retention of $\approx 90\%$ was obtained after 80 cycles in the dilute condition (Figure 2.7). Note that the initial capacity of 2.43 A h L^{-1} is close to the theoretical capacity of 2.68 A h L^{-1} , indicating $>90\%$ utilization of the ROM. The stable cycle performance of the multi-redox flow cell is mainly attributed to the chemical stability and compatibility of the DMPZ^{2+} in the electrolyte, whereas most ROMs with the second oxidation tend to destabilize the system, leading to deterioration of the cycle performance.^{20,21,52} To comprehend the chemical stability of the redox couples in the given MeCN-based electrolyte, the electronic structures of DMPZ, DMPZ^+ , DMPZ^{2+} , FL, and FL^- were compared with that of

MeCN using density functional theory (DFT) calculations, as illustrated in Figure 2.4d. It was observed that the energy levels of the lowest unoccupied molecular orbital (LUMO) of DMPZ and the singly occupied molecular orbital (SOMO) of the radical DMPZ^+ were both higher than the highest occupied molecular orbital (HOMO) level of MeCN. More importantly, the LUMO level of DMPZ^{2+} was located above the HOMO level of MeCN, indicating that the electron transfer from MeCN to DMPZ in any oxidation state during the battery operation is unfavorable, thus implying the electrochemical stability of DMPZ. Similarly, the electron transfer from DMPZ in any oxidation state to MeCN is energetically limited because the HOMO (or SOMO) levels of DMPZ and DMPZ^{2+} (or DMPZ^+) are lower than the LUMO level of MeCN. Notably, although the electron transfer from FL to MeCN or from MeCN to FL is not likely because of their relative energy levels, similar to the case of DMPZ, there is a chance for the recombination between DMPZ^+ and FL^- because of the higher SOMO level of FL^- than that of DMPZ^+ , suggesting the electron transfer from FL^- to DMPZ^+ . Although this type of recombination is rather expected in mixed electrolyte systems, it is interesting to observe that DMPZ^{2+} can be relatively more stable than DMPZ^+ against the recombination with FL^- because of the fully occupied HOMO level and the LUMO level that is slightly higher than the SOMO level of DMPZ^+ . This finding may imply that the use of double-redox ROMs is not necessarily less stable against the self-discharge of RFBs exploiting mixed electrolyte systems despite the higher oxidation states of ROMs that may more strongly attract the counter ROMs. These theoretical calculations support the

observed chemical and electrochemical stability of the MeCN-based flow cell with the double-redox DMPZ combined with FL. The time dependent degradation of radical species as a form of DMPZ^+ is also investigated using UV-vis spectroscopy because the stability of intermediate radicals is critically important in the RFB system utilizing ROMs.^{21,53,54} Interestingly, we observed the absorption spectra of the radical species is well maintained even after 24 hours, which implies DMPZ^+ has a superior radical stability (Figure 2.8).

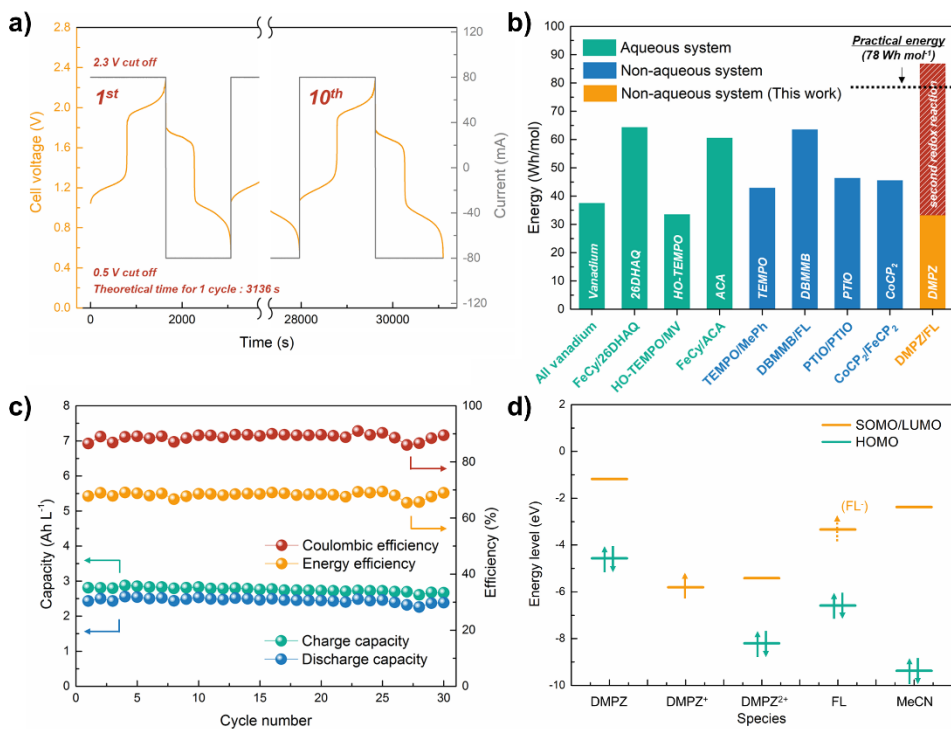


Figure 2.4. Electrochemical performance of DMPZ/FL flow cell. a) Cell voltage vs. time for 1st and 10th cycles at 20 mA cm⁻². b) Energy comparison of typical redox-active materials in RFB; the dashed area denotes the contribution of the 2nd redox reaction. * The energy density of the positive electrode compartment (energy density per volume) is determined by the intrinsic redox activity of the molecule (energy density per mole) and its solubility in the solvent (mole per volume). In order to emphasize the importance of the multi-redox reaction with respect to enhancing the intrinsic redox activity of molecules, we used the term ‘energy density per mole’ here instead of ‘energy density per volume’. Our intention is to decouple the engineering the intrinsic redox activity and the solubility. c) Cycling efficiencies and capacities

with respect to cycle number. d) Molecular orbital energies of ROMs and MeCN.

Note that the energy states of DMPZ change with the oxidation due to the relaxation effect of the molecules.

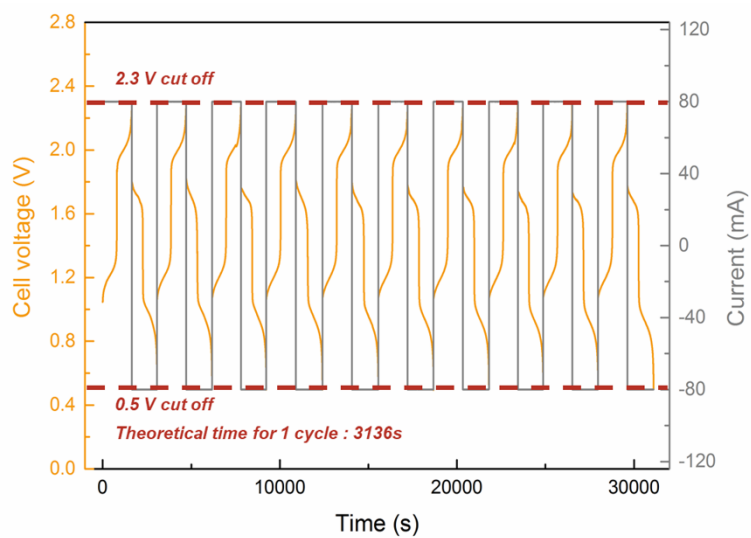


Figure 2.5. Cell voltage vs. time curves for the first 10 cycles at 20 mA cm^{-2} , which showed the same electrochemical behavior in cycling.

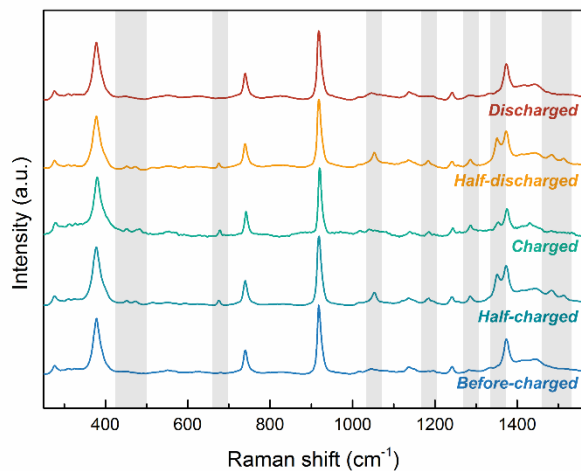


Figure 2.6. *Ex situ* Raman analysis of DMPZ in the positive electrode compartment demonstrating the reversible appearance and disappearance of several peaks. The vibrational modes corresponding to these peaks play important roles in the redox reaction of DMPZ.

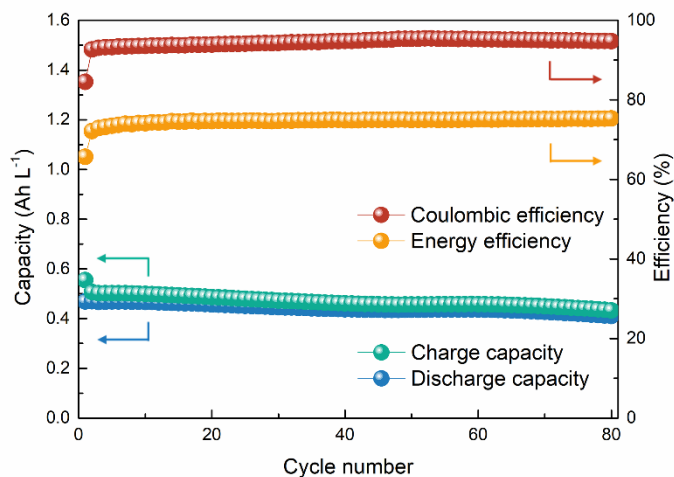


Figure 2.7. Cycling efficiencies and capacities with respect to cycle number for the electrolytes (13 mL on each side) containing FL (20 mM) and DMPZ (10 mM) in the supporting electrolyte of 0.5 M LiTFSi in MeCN. The current density of 20 mA cm⁻² was applied and the theoretical capacity is 0.54 A h L⁻¹.

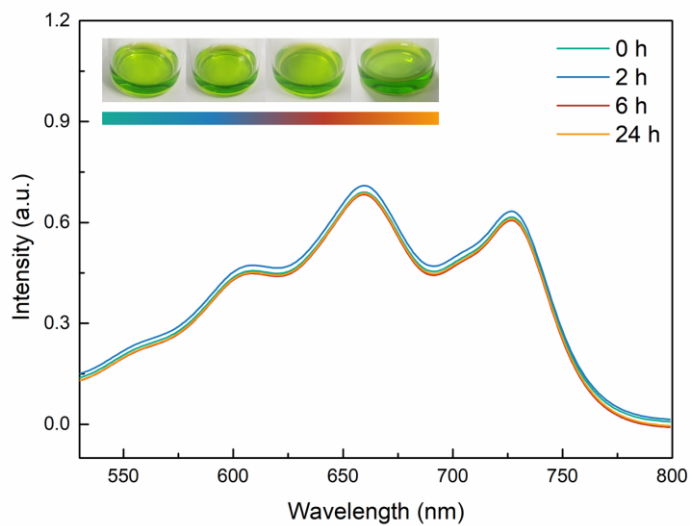


Figure 2.8. UV-vis spectra of DMPZ⁺ in the electrolytes of the positive electrode compartment at the SOC 50, captured at 0, 2, 6 and 24 h after sampling. The colour and absorption spectra show little change over 24 hours.

2.1.3.4 The colour change of DMPZ for the estimation of the state of charge

One of the interesting properties of the DMPZ/FL flow battery is that the state of charge (SOC) can be visually and precisely estimated by probing the colour change of DMPZ. Close monitoring of the SOC is critical in a battery system to prevent potential safety issues such as gas evolution.⁵⁵ Moreover, for new large-scale applications such as electric vehicles and ESSs, this monitoring becomes more vital because it informs the user when to charge and prevents the overcharging of batteries. Although electron spin resonance (ESR) spectroscopy has been used to determine the SOC in RFBs,¹⁷ it is not practically viable, and for multi-electron ROMs, there is not a one-to-one correspondence between the radical concentration of these ROMs and the SOC. Taking advantage of the marked colour change of DMPZ from yellow to green, orange, and red at different charged states, simple and rapid prediction of the SOC was possible. In the quantitative analysis, UV-vis spectroscopy enabled accurate measurement of the SOC based on Beer's law.⁵⁶ Figure 2.9 presents the UV-vis spectra and colour changes of DMPZ in the positive electrode compartment as a function of the SOC (with a step size of SOC 25). Colour changes were observed during two stages in the charging process and were attributed to the double-redox reaction of DMPZ. In the first stage (SOC 0 to 50), during which the DMPZ^+ concentration increased, the yellow colour became green, and in the UV-vis spectra (left in the figure), the intensities of the three peaks in the range of 580–750 nm gradually increased. In the second stage (SOC 50 to 100), during which DMPZ^+ was

oxidized to DMPZ^{2+} , the dark green colour became orange and finally red. In this stage, the peak intensities in the range of 580–750 nm decreased, and new peaks appeared in the range of 500–560 nm. Reversible changes of the colour and UV–vis spectra were also observed upon discharging, providing further confirmation of these changes. For the quantitative determination of the SOC, we selected two representative peaks at 660 and 521 nm in the UV–vis spectra for the reference, which were correlated to the concentrations of DMPZ^+ and DMPZ^{2+} depending on the SOC. Linear relationships between the absorbance and SOC were clearly observed for both peaks in each stage (*i.e.*, the first and second redox reactions), confirming that the accurate estimation of the SOC is possible in a DMPZ/FL flow battery (Figure 2.10).

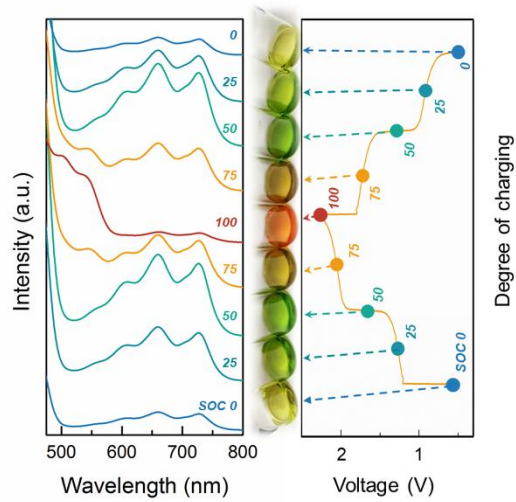


Figure 2.9. Prediction of SOC. Analysis of colour changes of DMPZ as a function of the SOC using UV–vis spectroscopy; the dotted arrows point to the corresponding colours of the electrolytes in the positive electrode compartment. Four pieces of Celgard 4560 were used to minimize the crossover and accurately measure the SOC, resulting in CE of >99%.

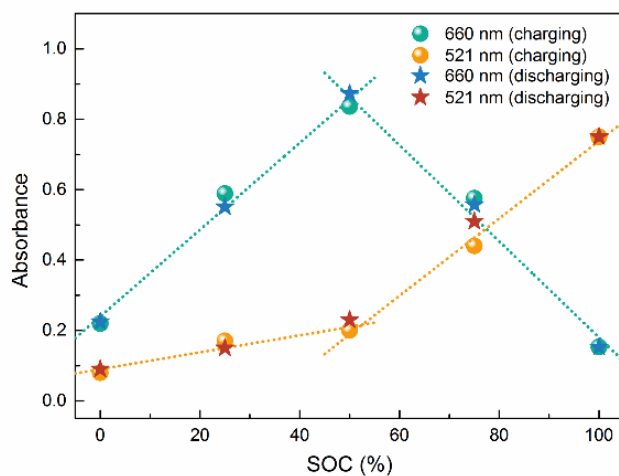


Figure 2.10. Linearly fitted plot of the absorbance of the peaks at 521 and 660 nm as a function of the SOC. Before SOC 50, the intensity of the peak at 660 nm linearly increased as the green colour became deeper and the DMPZ^+ concentration increased. After SOC 50, the peak intensity at 660 nm reversibly decreased and the peak intensity at 521 nm rapidly increased as the dark green colour changed to red and DMPZ^+ was oxidized to DMPZ^{2+} .

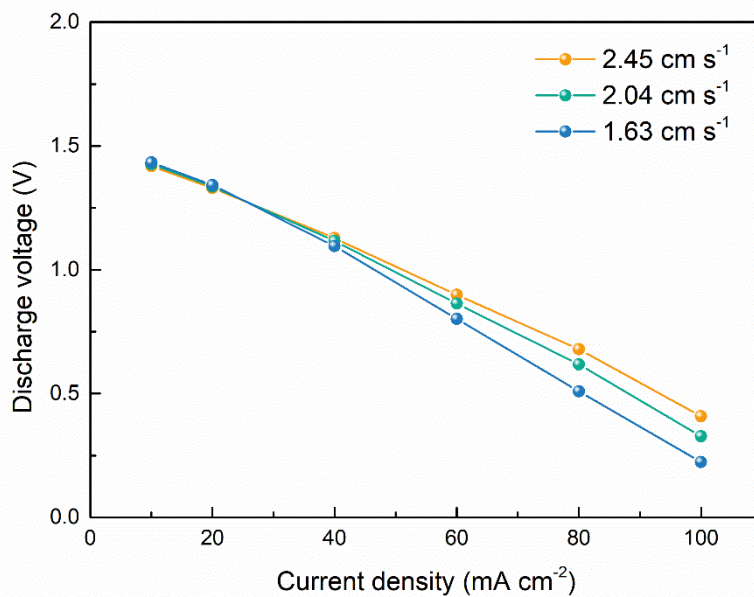


Figure 2.11. Plot of the average discharge voltage as a function of the current density for different mean linear flow velocities. As the current density increases, the cell polarization is getting worse. While there is no distinct difference at the low current densities, faster mass transport leads to much lower cell polarization at the high current densities.

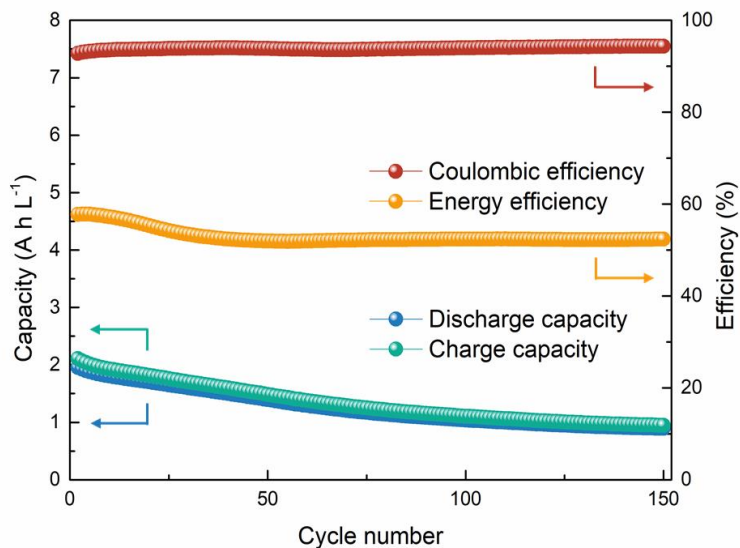


Figure 2.12. Cycling efficiencies and capacities with respect to cycle number using asymmetric cycling with 100 mA cm^{-2} on charging and 20 mA cm^{-2} on discharging. Widened voltage cut off of 0.5 V and 2.8 V was used to activate the second redox reaction due to the high polarization. Despite the high current density of 100 mA cm^{-2} , material utilization of $>70\%$ was achieved at the first cycle.

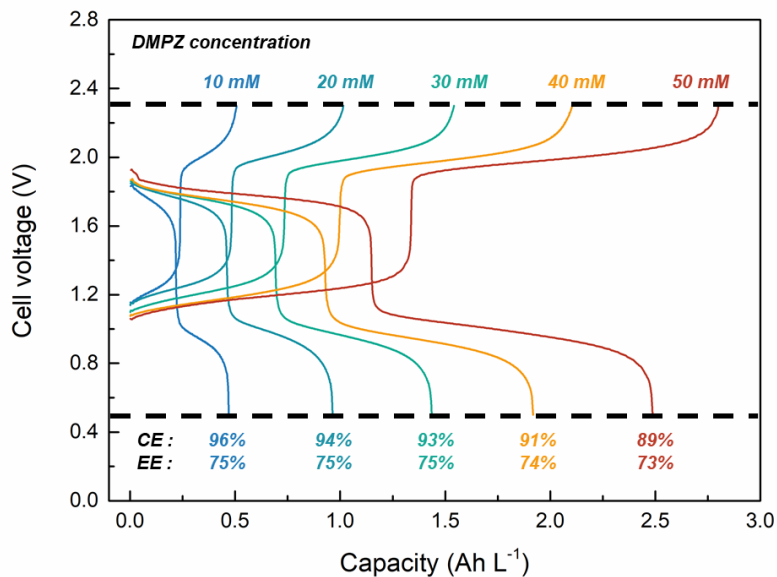


Figure 2.13. Representative charge-discharge curves for DMPZ/FL flow cell with coulombic and energy efficiencies at different concentrations. The capacity is proportional to the concentration of the active material. As the concentration increases, coulombic efficiency is slightly decreased because more crossover of the active material occurs at longer cycling times.

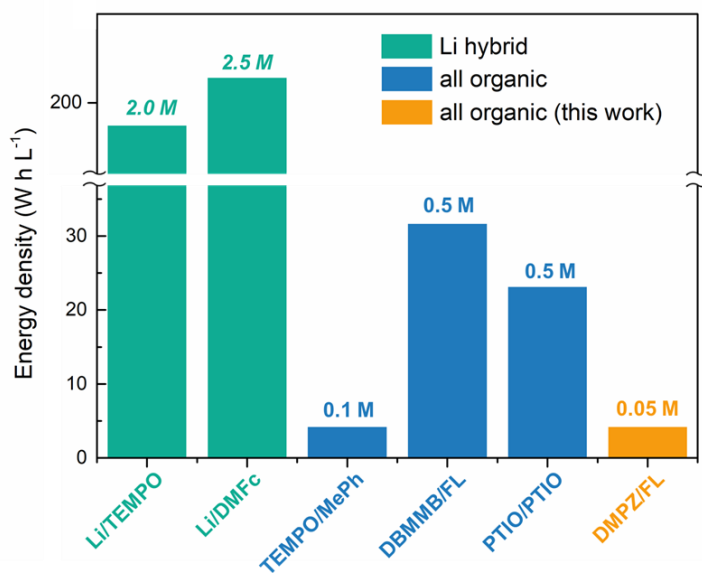


Figure 2.14. Volumetric energy density comparison of typical redox-active organic materials in nonaqueous RFB. Li hybrid organic RFB exhibits the highest energy density based on high cell voltage and concentration. Among all organic RFB, DBMMB/FL redox couple shows the highest values. Despite the half concentration, DMPZ/FL redox couple exhibits the same energy density with TEMPO/MePh redox couple, indicating multi-redox molecule has a great potential on high energy density RFB after its solubility is improved.

2.1.4 Concluding remarks

In summary, we employed, for the first time, a multi-electron redox DMPZ as a promising positive electrode material for high-energy-density RFBs. This novel ROM exhibited two reversible redox reactions at high redox potentials of -0.15 and 0.61 V vs. Ag/Ag⁺ and presented outstanding electrochemical kinetic properties for both the mass- and charge-transfer reactions. The DMPZ/FL flow cell exhibited two well-defined voltage plateaus at 1.2 and 2 V with superior material utilization (>90%) and remarkable chemical stability, delivering the highest energy per mole among reported aqueous and non-aqueous RFBs. In addition, the quantitative estimation of the SOC was possible based on the distinct colour change of DMPZ in two stages, offering an additional advantage of the system. While the solubility of DMPZ (≈ 60 mM) is not sufficient for direct application to ESSs, future efforts will aim to utilize the highly soluble version of DMPZ through the chemical modification; especially, we will focus on tailoring the molecular structure of DMPZ such as by attaching methoxy or ethoxy group to DMPZ to improve the solubility in MeCN-based solvents.²¹ These findings on this multi-electron redox material provide a potential new pathway for the design of high-energy-density RFBs and practically feasible ESSs.

2.1.5 References

- 1 Dunn, B., Kamath, H. & Tarascon, J.-M. Electrical energy storage for the grid: a battery of choices. *Science* **334**, 928-935 (2011).
- 2 Yang, Z. *et al.* Electrochemical energy storage for green grid. *Chem. Rev.* **111**, 3577-3613 (2011).
- 3 Zhao, H., Wu, Q., Hu, S., Xu, H. & Rasmussen, C. N. Review of energy storage system for wind power integration support. *Appl. Energy* **137**, 545-553 (2015).
- 4 Nguyen, T. & Savinell, R. F. Flow batteries. *Electrochem. Soc. Interface* **19**, 54 (2010).
- 5 Soloveichik, G. L. Flow batteries: current status and trends. *Chem. Rev.* **115**, 11533-11558 (2015).
- 6 Darling, R. M., Gallagher, K. G., Kowalski, J. A., Ha, S. & Brushett, F. R. Pathways to low-cost electrochemical energy storage: a comparison of aqueous and nonaqueous flow batteries. *Energy Environ. Sci.* **7**, 3459-3477 (2014).
- 7 Wang, W. *et al.* Recent progress in redox flow battery research and development. *Adv. Funct. Mater.* **23**, 970-986 (2013).
- 8 Leung, P. *et al.* Progress in redox flow batteries, remaining challenges and their applications in energy storage. *RSC Adv.* **2**, 10125-10156 (2012).
- 9 De Leon, C. P., Frías-Ferrer, A., González-García, J., Szánto, D. & Walsh, F. C. Redox flow cells for energy conversion. *J. Power Sources* **160**, 716-

- 732 (2006).
- 10 Arenas, L., de León, C. P. & Walsh, F. Engineering aspects of the design, construction and performance of modular redox flow batteries for energy storage. *Journal of Energy Storage* **11**, 119-153 (2017).
 - 11 Noack, J., Roznyatovskaya, N., Herr, T. & Fischer, P. The chemistry of redox-flow batteries. *Angew. Chem., Int. Ed.* **54**, 9776-9809 (2015).
 - 12 Gong, K., Fang, Q., Gu, S., Li, S. F. Y. & Yan, Y. Nonaqueous redox-flow batteries: organic solvents, supporting electrolytes, and redox pairs. *Energy Environ. Sci.* **8**, 3515-3530 (2015).
 - 13 Leung, P. *et al.* Recent developments in organic redox flow batteries: A critical review. *J. Power Sources* **360**, 243-283 (2017).
 - 14 Brushett, F. R., Vaughey, J. T. & Jansen, A. N. An all-organic non-aqueous lithium-ion redox flow battery. *Adv. Energy Mater.* **2**, 1390-1396 (2012).
 - 15 Song, Z. & Zhou, H. Towards sustainable and versatile energy storage devices: an overview of organic electrode materials. *Energy Environ. Sci.* **6**, 2280-2301 (2013).
 - 16 Jia, C. *et al.* High-energy density nonaqueous all redox flow lithium battery enabled with a polymeric membrane. *Sci. Adv.* **1**, e1500886 (2015).
 - 17 Wei, X. *et al.* TEMPO-based catholyte for high-energy density nonaqueous redox flow batteries. *Adv. Mater.* **26**, 7649-7653 (2014).
 - 18 Li, Z. *et al.* Electrochemical properties of an all-organic redox flow battery using 2, 2, 6, 6-tetramethyl-1-piperidinyloxy and N-methylphthalimide.

- Electrochem. Solid State Lett.* **14**, A171-A173 (2011).
- 19 Wei, X. *et al.* Radical compatibility with nonaqueous electrolytes and its impact on an all-organic redox flow battery. *Angew. Chem., Int. Ed.* **54**, 8684-8687 (2015).
- 20 Wei, X. *et al.* A high-current, stable nonaqueous organic redox flow battery. *ACS Energy Lett.* **1**, 705-711 (2016).
- 21 Milshtein, J. D. *et al.* High current density, long duration cycling of soluble organic active species for non-aqueous redox flow batteries. *Energy Environ. Sci.* **9**, 3531-3543 (2016).
- 22 Milshtein, J. D., Barton, J. L., Darling, R. M. & Brushett, F. R. 4-acetamido-2, 2, 6, 6-tetramethylpiperidine-1-oxyl as a model organic redox active compound for nonaqueous flow batteries. *J. Power Sources* **327**, 151-159 (2016).
- 23 Park, S.-K. *et al.* Electrochemical properties of a non-aqueous redox battery with all-organic redox couples. *Electrochem. Commun.* **59**, 68-71 (2015).
- 24 Takechi, K., Kato, Y. & Hase, Y. A highly concentrated catholyte based on a solvate ionic liquid for rechargeable flow batteries. *Adv. Mater.* **27**, 2501-2506 (2015).
- 25 Duan, W. *et al.* “Wine-Dark Sea” in an Organic Flow Battery: Storing Negative Charge in 2, 1, 3-Benzothiadiazole Radicals Leads to Improved Cyclability. *ACS Energy Lett.* **2**, 1156-1161 (2017).
- 26 Kosswattaarachchi, A. M. & Cook, T. R. Concentration-dependent charge-

- discharge characteristics of non-aqueous redox flow battery electrolyte combinations. *Electrochim. Acta* **261**, 296-306 (2018).
- 27 Winsberg, J. *et al.* Poly (TEMPO)/Zinc Hybrid-Flow Battery: A Novel, “Green,” High Voltage, and Safe Energy Storage System. *Adv. Mater.* **28**, 2238-2243 (2016).
- 28 Winsberg, J., Hagemann, T., Janoschka, T., Hager, M. D. & Schubert, U. S. Redox-Flow Batteries: From Metals to Organic Redox-Active Materials. *Angew. Chem., Int. Ed.* **56**, 686-711 (2016).
- 29 Sevov, C. S. *et al.* Physical organic approach to persistent, cyclable, low-potential electrolytes for flow battery applications. *J. Am. Chem. Soc.* **139**, 2924-2927 (2017).
- 30 Kim, H.-s., Lee, K.-J., Han, Y.-K., Ryu, J. H. & Oh, S. M. A comparative study on the solubility and stability of p-phenylenediamine-based organic redox couples for non-aqueous flow batteries. *J. Power Sources* **348**, 264-269 (2017).
- 31 Park, S.-K. *et al.* The influence of compressed carbon felt electrodes on the performance of a vanadium redox flow battery. *Electrochim. Acta* **116**, 447-452 (2014).
- 32 Arenas, L. F., de León, C. P. & Walsh, F. C. Mass transport and active area of porous Pt/Ti electrodes for the Zn-Ce redox flow battery determined from limiting current measurements. *Electrochim. Acta* **221**, 154-166 (2016).
- 33 Frisch, M. *et al.* GAUSSIAN09, Gaussian, Inc., Wallingford, CT,

- USA,(2009). *Google Scholar* (2016).
- 34 Rabaey, K., Boon, N., Höfte, M. & Verstraete, W. Microbial phenazine production enhances electron transfer in biofuel cells. *Environ. Sci. Technol.* **39**, 3401-3408 (2005).
- 35 Wang, Y., Kern, S. E. & Newman, D. K. Endogenous phenazine antibiotics promote anaerobic survival of *Pseudomonas aeruginosa* via extracellular electron transfer. *J. Bacteriol.* **192**, 365-369 (2010).
- 36 Mavrodi, D. V., Blankenfeldt, W. & Thomashow, L. S. Phenazine compounds in fluorescent *Pseudomonas* spp. biosynthesis and regulation. *Annu. Rev. Phytopathol.* **44**, 417-445 (2006).
- 37 Laursen, J. B. & Nielsen, J. Phenazine natural products: biosynthesis, synthetic analogues, and biological activity. *Chem. Rev.* **104**, 1663-1686 (2004).
- 38 Chen, J.-J. *et al.* Manipulation of microbial extracellular electron transfer by changing molecular structure of phenazine-type redox mediators. *Environ. Sci. Technol.* **47**, 1033-1039 (2012).
- 39 White, J. R. & Dearman, H. H. Generation of free radicals from phenazine methosulfate, streptonigrin, and riboflavin in bacterial suspensions. *Proc. Natl. Acad. Sci.* **54**, 887-891 (1965).
- 40 Lee, B. *et al.* Exploiting Biological Systems: Toward Eco-Friendly and High-Efficiency Rechargeable Batteries. *Joule* **2**, 61-75 (2017).
- 41 Lim, H.-D. *et al.* Rational design of redox mediators for advanced Li-O₂

- batteries. *Nat. Energy* **1**, 16066 (2016).
- 42 Lee, M. *et al.* Multi-electron redox phenazine for ready-to-charge organic batteries. *Green Chem.* **19**, 2980-2985 (2017).
- 43 Nelson, R., Leedy, D., Seo, E. & Adams, R. N. Anodic oxidation of 5, 10-dihydro-5, 10-dimethylphenazine. *Z. Anal. Chem.* **224**, 184-196 (1966).
- 44 Lee, S. *et al.* Recent Progress in Organic Electrodes for Li and Na Rechargeable Batteries. *Adv. Mater.*, 1704682 (2018).
- 45 Zhang, H., Zhang, H., Li, X., Mai, Z. & Zhang, J. Nanofiltration (NF) membranes: the next generation separators for all vanadium redox flow batteries (VRBs)? *Energy Environ. Sci.* **4**, 1676-1679 (2011).
- 46 Wei, X. *et al.* Microporous separators for Fe/V redox flow batteries. *J. Power Sources* **218**, 39-45 (2012).
- 47 Lopez-Atalaya, M., Codina, G., Perez, J., Vazquez, J. & Aldaz, A. Optimization studies on a Fe/Cr redox flow battery. *J. Power Sources* **39**, 147-154 (1992).
- 48 Wang, W. *et al.* Anthraquinone with tailored structure for a nonaqueous metal-organic redox flow battery. *Chem. Commun.* **48**, 6669-6671 (2012).
- 49 Duan, W. *et al.* A symmetric organic-based nonaqueous redox flow battery and its state of charge diagnostics by FTIR. *J. Mater. Chem. A* **4**, 5448-5456 (2016).
- 50 Bard, A. J. & Faulkner, L. R. *Fundamentals and Applications* (Springer, 2002).

- 51 Saraidaridis, J. D., Bartlett, B. M. & Monroe, C. W. Spectroelectrochemistry of Vanadium Acetylacetonate and Chromium Acetylacetonate for Symmetric Nonaqueous Flow Batteries. *J. Electrochem. Soc.* **163**, A1239-A1246 (2016).
- 52 Huang, J. *et al.* The lightest organic radical cation for charge storage in redox flow batteries. *Sci. Rep.* **6**, 32102 (2016).
- 53 Beh, E. S. *et al.* A neutral pH aqueous organic–organometallic redox flow battery with extremely high capacity retention. *ACS Energy Lett.* **2**, 639-644 (2017).
- 54 Chen, H., Cong, G. & Lu, Y.-C. Recent Progress in Organic Redox Flow Batteries: Active Materials, Electrolytes and Membranes. *Journal of Energy Chemistry* (2018).
- 55 Ding, C., Zhang, H., Li, X., Liu, T. & Xing, F. Vanadium flow battery for energy storage: prospects and challenges. *J. Phys. Chem. Lett.* **4**, 1281-1294 (2013).
- 56 Cannon, C. & Butterworth, I. Beer's law and spectrophotometer linearity. *Anal. Chem.* **25**, 168-170 (1953).

2.2 Enhancement of energy density through the molecular modification

(The essence of this chapter has been published in *Joule*. Reproduced with permission from [Kwon, G. *et al.*, *Chem* **2019**, 5, 2642-2656] Copyright (2019) Elsevier)

2.2.1 Research background

With the ever-increasing global demand for the development of greener and sustainable energy sources to mitigate the environmental concerns associated with fossil fuels, renewable energy sources such as solar and wind power are becoming affordable and broadly deployed. To achieve round-the-clock energy delivery, however, these power sources must be paired with scalable energy storage systems (ESSs) owing to the significant mismatch between the energy supply and demand.^{1,2} Redox flow batteries (RFBs), which utilize redox-active materials dissolved in separate electrolytes, are considered some of the most promising ESSs for modern grid markets, and decoupling the energy and power is regarded facile for RFB systems.³⁻⁸ With the aim of pursuing the development of green energy technology, research on RFBs has also shifted from conventional metal-based redox-active materials such as vanadium and zinc to redox-active organic materials (ROMs), which are naturally abundant and potentially cost effective, safe, and chemically tunable.⁹⁻¹¹ In particular, recent studies on non-aqueous all-organic RFBs (NORFBs) have demonstrated the great promise for achieving high energy densities in these

systems without the concerns associated with water electrolysis, which typically limits the working voltage to a narrow range and thus leads to a rather low energy density in aqueous RFBs.¹²⁻¹⁷

Despite the great potential of organic RFBs, their practical energy density remains very low.¹⁰ The energy density of ROM-based RFBs is dependent on the following three factors: i) the selection of the anolyte and catholyte and their corresponding redox potential difference, (ii) the amount of ROMs dissolved, and iii) the number of electrons participating in the redox reaction per ROM. Extensive research in recent years has led to the identification of various promising ROMs, such as quinone and viologen derivatives, that can be used as anolytes (*i.e.*, n-type or reduction type).¹⁸⁻²⁶ For these anolyte ROMs, remarkable performance enhancements in terms of the solubility and multi-electron redox activity have been achieved.^{23,27,28} Nevertheless, only a limited number of ROMs have been reported as promising catholyte materials (*i.e.*, p-type or oxidation type).^{8,29} Research on these p-type (oxidation type) ROMs is still in its infancy, and high-energy organic RFBs can only be realized when anolytes are coupled with appropriate catholytes.^{12,25,30,31} Moreover, p-type ROMs capable of multi-electron redox reactions are even rarer because their oxidized states, such as dications, are often highly unstable in solution.¹³

Considering a realistic limit of the ROM concentration in non-aqueous media,^{15,32} exploiting multi-electron redox from a single p-type ROM is indispensable to achieve high energy density at a given concentration.³³ Several

attempts have very recently been made to utilize multi-electron redox p-type ROMs as catholytes.³⁴⁻³⁶ For instance, Kowalski *et al.* demonstrated that the chemical stability of the dication state of phenothiazine-based molecules can be enhanced by introducing methoxy groups at the *para* positions to the nitrogen atom of the phenothiazine core. Accordingly, the second redox reaction of the phenothiazine catholyte can be utilized reversibly in a non-aqueous bulk electrolysis cell.³⁵ However, critical challenges in multi-electron redox catholyte ROMs must be addressed, such as their low solubility (<0.1 M) and lack of long-term stability in flow cell.^{35,36} To realize high-energy-density RFBs, there is thus an urgent demand for the development of new p-type ROMs capable of stable and reversible multi-electron redox that exhibit high solubility.

In this report, we present a high-energy-density NORFB by exploiting a multi-electron redox p-type ROM as a catholyte; this ROM was rationally designed by mimicking the energy transduction in living organisms. This newly synthesized phenazine-based molecule, 5,10-bis(2-methoxyethyl)-5,10-dihydrophenazine (BMEPZ), undergoes double-redox reactions at high redox potentials with enhanced solubility in non-aqueous media. Its redox mechanism is carefully investigated using spectroscopic tools combined with a computational method. Its multi-electron redox reactions are revealed to be remarkably reversible in acetonitrile (MeCN) solution and highly stable in all redox states. In addition, this molecule outperforms previously reported ROMs in terms of its mass- and charge-transfer kinetics. A full-flow RFB, in which BMEPZ is dissolved as a catholyte at concentrations of up to

0.4 M, is prepared and exhibits stable cycle performance, delivering the highest energy densities ($\sim 17 \text{ Wh L}^{-1}$) among NORFBs reported thus far. We believe that our material design can pave the way for the practical use of NORFB by reducing its performance gap with the state-of-the-art vanadium-based RFBs and aqueous all-organic RFBs (AORFBs).³⁷⁻³⁹

2.2.2 Experimental method

2.2.2.1 Preparation of materials

MeCN (anhydrous) and FL were purchased from Sigma–Aldrich and used without further purification. The microporous separator (Celgard 4560) and LiTFSI were purchased from Wellcos (Korea) and TCI Chemicals (Japan) and were treated under vacuum at 70 °C for 24 h to remove moisture. Tetrahydrofuran (THF) was distilled using sodium/benzophenone before use. All the other reagents and solvents were obtained from Sigma-Aldrich and Alfa Aesar Co. and used as received without further purification. All the glassware, syringes, magnetic stirring bars, and needles were thoroughly dried in a convection oven. The reactions were monitored using thin layer chromatography (TLC) using commercial TLC plates (silica gel 60 F254, Merck Co.).

2.2.2.2 Synthesis and characterization

The 5,10-dihydrophenazine (**1**) was prepared following reported procedures.⁴⁰ Phenazine (3 g, 16.6 mmol) was dissolved in ethanol (75 mL), and the solution was heated to boiling. An aqueous solution (300 mL) containing Na₂S₂O₄ (30 g, 0.17 mol) was added to the boiling solution. The solution turned purple immediately after mixing; then, a greenish white precipitate formed. The precipitated solid was collected by filtration, washed with water, and dried in vacuo to afford 2.7 g of a greenish white solid. Because of its instability in air, the solid was stored under nitrogen without further purification and characterized.

In a flame-dried two-necked 100-mL round bottom flask, **1** (1 g, 5.5 mmol)

was dissolved in freshly distilled THF (12 mL). To this solution, 1.6 M n-butyl lithium (n-BuLi) in hexane (9.5 mL, 15.4 mmol) was added dropwise over 30 min at room temperature. After an orange precipitate was formed, 2-chloroethyl methyl ether (3.5 mL, 38.5 mmol) was added. Subsequently, the orange precipitate disappeared, forming a reddish-brown solution. The solution was stirred overnight, and the reaction mixture was then poured into water and extracted three times with ethyl acetate. The organic layer was dried over anhydrous MgSO₄ and purified using column chromatography on neutral alumina with ethyl acetate/n-hexane (1:19 v/v) as an eluent to give a light-yellow powder. Yield: 78.2% (1.28 g), ¹H-NMR (300 MHz, C₆D₆) δ(ppm): 6.60-6.57 (m, 4H), 6.31-6.28 (m, 4H), 3.43 (t, *J* = 6.3 Hz, 4H), 3.25 (t, *J* = 6.3 Hz, 4H), 2.99 (s, 6H). ¹³C-NMR (125 MHz, C₆D₆) δ(ppm): 137.75, 111.84, 69.15, 59.03, 46.35. Anal. calcd. for C₁₈H₂₂N₂O₂: C, 72.46; H, 7.43; N, 9.39; found: C, 72.42; H, 7.43; N, 9.38; HRMS (EI⁺): calcd. for C₁₈H₂₂N₂O₂ (M⁺), 298.1681; found, 298.1684. (Figure 2.30)

¹H-NMR and ¹³C-NMR spectra were recorded on a Bruker Avance-300 and Avance-500 NMR spectrometer, respectively. High-resolution mass spectra (HRMS) were obtained using a JEOL JMS-700 instrument. Elemental analysis was conducted using a Thermo Fisher Scientific Flash 2000 elemental analyzer.

In the solubility measurement, 30.2 mg of BMEPZ powders was fully dissolved in 2 mL MeCN to make a 0.05 M solution first. Then, to the solution, the same amount (30.2 mg) of BMEPZ powders was repeatedly added until it gets saturated without further dissolution.

Raman spectra (LabRAM HR Evolution, Horiba) were recorded using capillary tubes (inner diameter of 1.1–1.2 mm) with continuous-wave linearly polarized lasers (wavelength: 532 nm). The laser beam was focused using a 50× objective lens, resulting in a spot diameter of approximately 1 μm . The acquisition time and number of accumulations were 10 s and 5, respectively.

For the UV–vis spectroscopy analysis, absorption spectra of the electrolytes in the positive electrode compartment (diluted in MeCN, 5% v/v) were obtained using a UV–vis spectrometer (Agilent Technologies, Cary 5000) with an optical glass cuvette (Quartz; Hellma®). Electrolytes containing 10 mM BMEPZ and 20 mM FL in the supporting electrolyte of 0.5 M LiTFSI in MeCN were used.

2.2.2.3 Electrochemical measurements

For the electrochemical measurements, the solutions were prepared and evaluated in an Ar-filled glove box under an inert atmosphere (<0.5 ppm O_2 , H_2O). CV curves of DMPZ, BMEPZ, FL, and the mixture of BMEPZ and FL (10 mM each) were obtained using 0.1 M LiTFSI in MeCN as a supporting electrolyte. A three-electrode system (a Pt counter electrode, a Ag/AgNO₃ reference electrode, and Au working electrode) was employed, and a scan rate of 100 mV s^{-1} was used. Ferrocene (5 mM) was used as an internal reference.

For the bulk-electrolysis test, a commercially available bulk electrolysis cell (MF-1056) was used. The cycling experiment used an electrolyte consisting of 1 mM BEMPZ and 0.5 M LiTFSI in MeCN (30 mL) and was stirred at 1400 rpm. A three-electrode system (a Pt counter electrode, Ag/AgNO₃ reference electrode, and

reticulated vitreous carbon working electrode) was employed at a current of 1.608 mA (1C).

For the RDE test, a three-electrode system (a Pt counter electrode, Ag/AgNO₃ reference electrode, and glassy carbon working electrode with 5-mm diameter) was employed for the LSV tests. The BMEPZ⁺ solution was prepared by oxidizing the BMEPZ solution in the bulk-electrolysis experiment under a cut-off voltage of -0.11 V vs. Fc/Fc⁺. The working electrode was rotated from 300 to 1500 rpm (in increments of 300 rpm) using a modulated speed rotator (AFMSRX; PINE). The LSV tests were conducted with 1.0 mM ROMs in 0.5 M LiTFSI in MeCN at a scan rate of 5 mV s⁻¹. The kinematic viscosity (ν) of the 0.5 M LiTFSI in MeCN was measured to be 0.59 mm² s⁻¹ following the standard test method ASTM D445 in Korea Polymer Testing & Research Institute (Koptri, Korea). Using the slopes of the linearly fitted Levich plots (Figure 2.19c) and the Levich equation (eq. 1), the diffusion coefficients (D) of the ROMs were calculated (the slopes of BMEPZ and BMEPZ⁺ were determined to be 1.30×10^{-5} and 1.38×10^{-5} A rad^{-1/2} s^{1/2}, respectively). Using the Koutecký–Levich equation (eq. 2), Koutecký–Levich plots (Figure 2.20c, d) were obtained at different overpotentials, and the kinetic rate constants of the ROMs were calculated using eq. 3.

$$i_L = 0.62nFAD^{2/3}\omega^{1/2}\nu^{-1/6}C_0 \quad (1)$$

$$\frac{1}{i} = \frac{1}{i_k} + \frac{1}{0.62nFAD^{2/3}\omega^{1/2}\nu^{-1/6}C_0} \quad (2)$$

$$i_0 = nFAk_0C_0 \quad (3)$$

Here, n is the number of electrons transferred ($n = 1$), F is the Faraday constant

($F = 96485 \text{ C mol}^{-1}$), A is the electrode area ($A = 0.2 \text{ cm}^2$), and C_0 is the concentration of the ROM ($C_0 = 1.0 \text{ mM}$).

For the scan-rate dependence CV study, CV curves of BMEPZ and FL (10 mM each) were obtained using 0.5 M LiTFSI in MeCN as a supporting electrolyte at the following scan-rates: 25, 50, 100, 200, and 300 mV s^{-1} . Randles-sevcik equation (eq. 4) was used to calculate the diffusion coefficients of ROM.

$$i_p = 0.4463nFAC \left(\frac{nFSD}{RT} \right)^{\frac{1}{2}} \quad (4)$$

Here, A is the electrode area ($A = 7.07 \text{ mm}^2$), C is the concentration of the ROM ($C = 10 \text{ mM}$), and s is the scan-rate, respectively.

A custom flow cell with backing plates (polyethylene-coated fiber glass), flow fields (polytetrafluoroethylene (PTFE)), and gaskets (PTFE) was fabricated using materials purchased from ILDO F&C (Korea). The flow cells were assembled with carbon felt (XF30A; TOYOBO, Korea) as electrodes at both the anode and cathode side with four pieces of microporous separators (Celgard 4560) sandwiched in between. The active size of the flow cell was 2.0-cm wide \times 2.0-cm long (4 cm^2), and norprene tubing (Masterflex) was used. The mixed electrolytes (13 mL in each half-cell side) containing both BMEPZ and FL with the supporting electrolyte of 0.5 M LiTFSI in MeCN were flowed through the felt electrodes at a flow rate of 80 mL min^{-1} using a pump (ShenChen). In the case of 0.4 M BMEPZ cell test, 0.8 M FL and 1.0 M LiTFSI were used as the anolyte and the supporting electrolyte, respectively. Flow cell tests were performed at a current density of 20 mA cm^{-2} in constant-current mode using a battery test system (WBCS 3000; WonA Tech, Korea), and free 20

cycles (5 cycles for 0.4 M BMEPZ and 0.8 M FL cell test) were conducted in advance for initial equilibration of the flow setup. The volumetric energy density was calculated based on the entire electrolyte volume (26 mL).

2.2.2.4 Computational details

Spin-unrestricted density functional theory (DFT)-type calculations were performed using the Gaussian 09 package,⁴¹ including geometry optimization, energy evaluation, eigenvalue calculation, NPA calculation, and vibration property prediction for each molecule. The Becke–Lee–Yang–Parr (B3LYP) hybrid exchange-correlation functional⁴²⁻⁴⁴ and triple-zeta valence polarization (TZVP) basis set^{45,46} were used for the entire calculation, which have been demonstrated to reproduce experimental results well.^{36,47-49} To model the solvation environment of acetonitrile (dielectric constant = 38.8), the polarizable continuum model (PCM) scheme, implicit solvation model, was introduced for the entire calculation. The lowest unoccupied molecular orbital (LUMO) and solely occupied molecular orbital (SOMO) denote the adiabatic LUMO/SOMO.

2.2.3 Results and discussions

2.2.3.1 Bio-inspired redesign of catholyte material

In biosystems, common redox active molecules are known to undergo multi-electron redox reactions in the electron transport chains. Among such biological redox systems, methanophenazine is known to act as a redox mediator in a respiratory chain of archaea *Methanosarcina mazei* Gö1.⁵⁰ The methanophenazine can transport two electrons accompanying translocation of two protons through reversible reduction reactions (see Figure 2.15a).⁵¹ The redox core structure of the methanophenazine consists of a pyrazine core bearing two imine-like nitrogen ($-N=$) atoms. By accepting two electrons with two protons, the pyrazine core is reduced to form a dihydrophenazine (see the core structures and details of the redox reactions in Figure 2.16a), offering a redox potential of approximately -165 mV vs. NHE. Because of its suitable potential as an anolyte, several derivatives possessing the pyrazine core were recently utilized as anolytes for AORFBs coupled with a $Fe(CN)_6$ catholyte.⁵² Pyocyanin, a redox-active molecule involved in the electron-transfer reactions of *Pseudomonas aeruginosa* bacteria,⁵³ bears a similar core structure as methanophenazine but has a substituent in the core, delivering much higher redox potential in its deprotonation of NADH (Figure 2.15a and Figure 2.16b).^{54,55} Similar to the pyrazine core, the methylpyrazinium moiety as a redox core also undergoes a reduction by two electrons; however, only one proton is involved to form a methylhydrophenazine because the quaternized N can be reduced to a tertiary amine-like N without a proton. In contrast to the proton compensation for the

pyrazine/dihydropyrazine couple, this methylated-pyrazine-core redox couple (*i.e.*, methylpyrazinium/methyl-hydropyrazine) can bear a positive charge in its oxidized form.

Comparison of these two bio redox systems led us to speculate that the absence of the charge-relief process resulting from methylation likely leads to a higher redox potential ($E_{1/2} = -40$ mV vs. NHE) of pyocyanin,⁵⁵ and we anticipated that an additional methylation on the other imine-like N of the pyrazinium core would further increase the redox potential. Indeed, we observed that 5,10-dimethyldihydrophenazine (DMPZ) could undergo redox reactions at higher potentials ($E_{1/2} = -0.26$ and 0.50 V vs. Fc/Fc^+ , ~ 0.40 and 1.16 V vs. NHE, see Figure 2.16c) between a dimethylpyrazine dication/dimethylpyrazine redox core couple.^{36,48} Moreover, because of the increased redox potential, in contrast to methanophenazine and pyocyanin, DMPZ naturally exists in its reduced form (neutral form) and reversibly undergoes two stepwise single-electron oxidations to form a stable dication (*i.e.*, p-type redox) and is thus suitable for use as a catholyte. Nevertheless, the intrinsically low solubility of DMPZ (~ 60 mM in MeCN) has been a critical bottleneck for its practical application in RFBs.³⁶ Despite its high redox potential and multi-electron redox capability, the actual energy densities of RFBs employing DMPZ as a catholyte are far from practical application.

To this end, we attempted to re-tailor the DMPZ molecules to improve their solubility while maintaining the reversible and stable redox capability and succeeded in obtaining a new derivative, BMEPZ, that bears two flexible 2-methoxyethyl

chains instead of the methyl groups (see step 4 in Figure 2.15a). It was expected that the flexibility and bulkiness of the alkyl ether chains would not only improve the solubility but also enhance the stability of the dication form by spatially hindering the redox-active N atoms from undergoing side reactions.⁵⁶⁻⁵⁸ Synthesis of BMEPZ was performed starting with reduction of phenazine using $\text{Na}_2\text{S}_2\text{O}_4$, followed by N-substitution of both amino groups with 2-chloroethylmethyl ether. The molecular structure of the synthesized BMEPZ was characterized using nuclear magnetic resonance (NMR) spectroscopy, high-resolution mass spectroscopy (HRMS), and elemental analysis (see the experimental section and Figure 2.17 for the synthetic details and reaction schemes). The newly synthesized BMEPZ exhibited enhanced solubility in MeCN as high as 0.5 M, which is one order of magnitude greater than that of the original DMPZ. To confirm that the substitution that improved the solubility did not reduce its original redox capability, we conducted cyclic voltammetry (CV) measurements of BMEPZ in MeCN solution. As shown in Figure 2.18, BMEPZ displayed two reversible redox peaks at voltages of -0.29 and 0.50 V vs. Fc/Fc^+ , which are identical to those of DMPZ. The electrochemical properties of BMEPZ will be discussed in further detail in the following sections.

To construct the all-organic RFB, the commercially available 9-fluorenone (FL) was employed as a typical anolyte ROM; FL undergoes an n-type redox reaction at -1.50 V vs. Fc/Fc^+ .¹² Because FL is highly soluble and undergoes one-electron redox reaction with good reversibility in MeCN, we could avoid unnecessary complexity in evaluating the redox activities of BMEPZ in the flow cell.¹² Figure

2.15b shows the redox activities of BMEPZ and FL in a mixed electrolyte along with the molecular structures for the corresponding redox states. In the CV measurement, the mixed electrolyte showed three reversible redox peaks with redox potentials and current levels identical to those of the corresponding redox peaks of each material in the separate electrolytes (Figure 2.18). Thus, the redox behaviors of the two ROMs were unaffected by each other in any redox states in the mixed electrolyte system.^{12,59} According to the CV results, the all-organic RFB exploiting the BMEPZ/FL redox couple is expected to offer the cell voltages of 1.21 and 2.00 V.

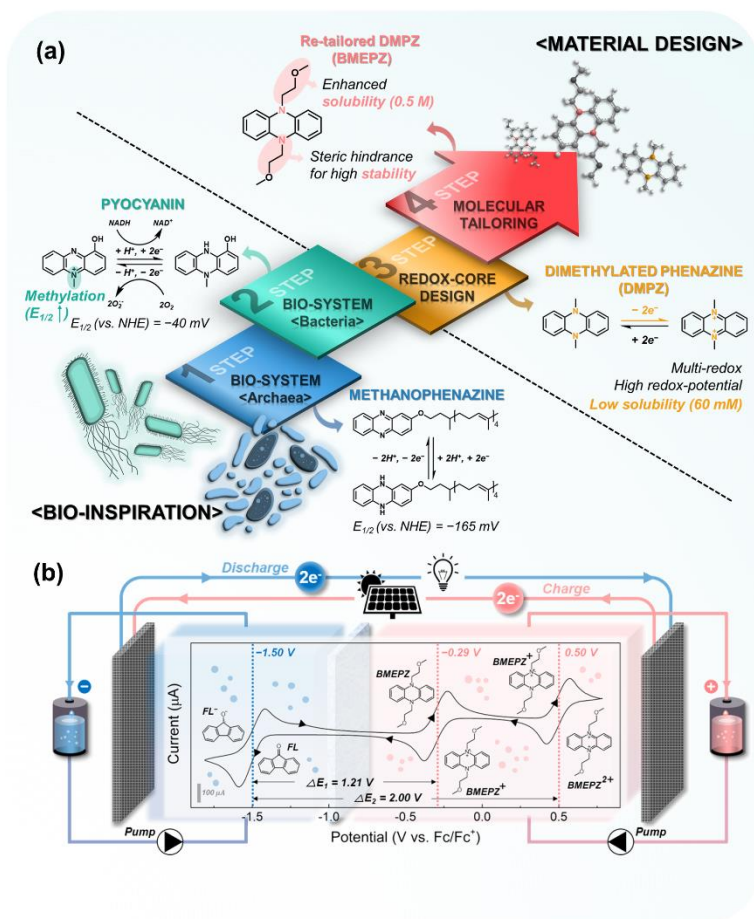


Figure 2.15. A new multi-electron redox catholyte material with enhanced solubility, BMEPZ. a) The rational molecular design strategy of BMEPZ inspired by biological redox systems. b) Schematic illustration of all-organic full-flow battery containing BMEPZ/FL electrolytes and CV curves of the redox couple at a scan rate of 100 mV s^{-1} .

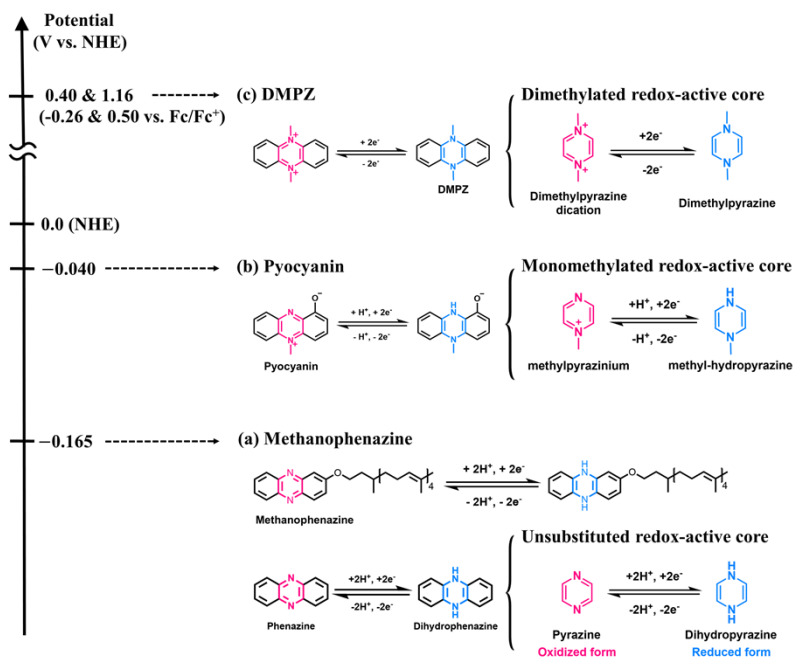


Figure 2.16. Redox core structures and reaction mechanisms of the phenazine biomolecules: a) methanophenazine, b) pyocyanin, and c) DMPZ. Redox potential of DMPZ vs. NHE was linearly converted using ferrocene/ferrocenium redox couple as an internal reference of 0.66 V vs. NHE.

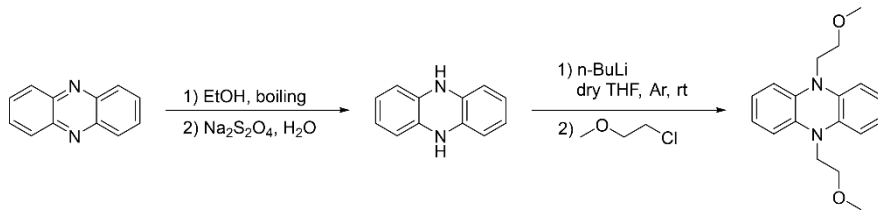


Figure 2.17. Synthetic route of BMEPZ.

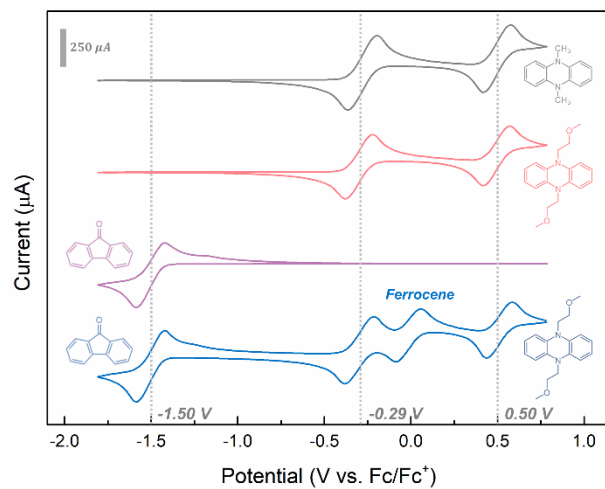


Figure 2.18. CV curves of the ROMs at a scan rate of 100 mV s^{-1} : DMPZ (gray line), BMEPZ (pink line), FL (purple line), and the mixture of BMEPZ and FL with ferrocene as an internal reference (blue line).

2.2.3.2 Characterization of BMEPZ catholyte

We conducted bulk electrolysis and rotating disk electrode (RDE) experiments to investigate the intrinsic electrochemical properties of the newly synthesized BMEPZ molecule. Bulk electrolysis was appropriate to investigate the inherent redox ability and stability of BMEPZ under convection without considering the anolyte in the actual RFB system. As shown in Figure 2.19a, BMEPZ exhibits two distinct plateaus on charge and discharge at potentials consistent with the observations from the CV measurements. In addition, the measured capacity (1.573 mAh) was remarkably close to the theoretical value (1.608 mAh), indicating that all the BMEPZ molecules effectively contributed to the two-step reactions of each single-electron redox. Moreover, highly stable cycling was observed without any noticeable capacity fading, as shown in Figure 2.19b, implying that the multi-redox reactions of BMEPZ are reversible. The RDE tests revealed the kinetic properties of the BMEPZ and BMEPZ⁺ species with respect to the mass-diffusion and charge-transfer rates. In the linear sweep voltammetry (LSV) curves, the mass-transfer-controlled limiting currents (i_L) increased with increasing rotation rate (ω) in the range of 300–1500 rpm (Figure 2.20a, b). Figure 2.19c shows that the linear relationship between i_L and the square root of ω was well-fitted by the Levich equation;⁶⁰ the diffusion coefficients (D) of BMEPZ and BMEPZ⁺ were calculated to be 1.02 and $1.12 \times 10^{-5} \text{ cm}^2 \text{ s}^{-1}$, respectively (a detailed description of the calculations is provided in the electrochemistry section of the Methods section). The kinetic-controlled currents (i_k) at different overpotentials (η) were also determined

by extrapolation in the Koutecký–Levich plots (Figure 2.20c, d).⁶⁰ The logarithms of the exchange currents ($\log i_0$) were determined to be -3.65 for BMEPZ and -3.28 for BMEPZ⁺ in the linearly fitted plots of $\log i_k$ vs. η (Figure 2.19d), yielding kinetic rate constants (k_0) of 1.18×10^{-2} and $2.77 \times 10^{-2} \text{ cm s}^{-1}$, respectively. Notably, even though BMEPZ is bulkier than DMPZ, the kinetics of BMEPZ were on par with or even faster than those of DMPZ (D of 1.58×10^{-5} and $8.82 \times 10^{-6} \text{ cm}^2 \text{ s}^{-1}$, respectively, and k_0 of 2.97×10^{-2} and $5.53 \times 10^{-3} \text{ cm s}^{-1}$, respectively, for DMPZ and DMPZ⁺).³⁶ In Figure 2.19e, the kinetic parameters for BMEPZ, BMEPZ⁺, and FL (blue stars) are compared with those of previously reported materials for RFBs (pink circle dots) on a logarithmic scale. It is noteworthy that the BMEPZ/FL redox couple exceeds the others in terms of both mass- and charge-transfer kinetics, implying that the redox couple would be favorable for a low-polarization and high-efficiency RFB. In addition, a scan-rate dependent CV study was conducted to verify the reversibility of BMEPZ/FL redox couple. As shown in Figure 2.21, the current ratio between cathodic and anodic peaks of both BMEPZ and FL was almost unity in the CV curves, implying their superior reversibility. The redox couple showed the peak separations ranging from 80 to 100 mV with respect to the scan-rate. Furthermore, Randles-Sevcik equation was used to determine their diffusion coefficients.⁶¹ The diffusion coefficients of BMEPZ, BMEPZ⁺, and FL were calculated to be 8.86×10^{-6} , 1.16×10^{-5} , and $1.05 \times 10^{-5} \text{ cm}^2 \text{ s}^{-1}$, respectively, which are consistent with those from the RDE study.

Raman spectroscopy and natural population analysis (NPA) were

conducted to verify the redox mechanism of the BMEPZ molecule. In Figure 2.22a, the reversible changes of the local bonding of BMEPZ (pink areas) upon charging and discharging are shown. Notably, the peak changes mainly corresponded to the vibrational modes of C–N–C and C=C bonds in the reduced diazabutadiene motif (N–C=C–N), which is consistent with the previous observation for DMPZ (Table S1).^{36,48} In addition, the NPA enabled visualization of the changes of the charge distribution of BMEPZ during the redox reaction. From the results for BMEPZ, BMEPZ⁺, and BMEPZ²⁺ (Figure 2.23), the change of the charge was plotted for each atom as colors ranging from white to pink, as shown in Figure 2.22b. The most drastic color changes were observed at the nitrogen atoms, followed by the conjugated carbons in the benzene rings, implying that the redox reaction of BMEPZ mainly occurs in the diazabutadiene motif. This finding supports the idea that the flexible side chains substituted to elevate the solubility did not affect the general redox mechanisms.

To explore the origin of the chemical stability of the BMEPZ molecule at all redox states in the given MeCN-based electrolyte, density functional theory (DFT) calculations were conducted for BMEPZ, BMEPZ⁺, BMEPZ²⁺, and MeCN. It was observed that the energy levels of the lowest unoccupied molecular orbital (LUMO) of BMEPZ and the singly occupied molecular orbital (SOMO) of the radical BMEPZ⁺ were located above the highest occupied molecular orbital (HOMO) level of MeCN. More importantly, even the LUMO level of BMEPZ²⁺ was higher than the HOMO level of MeCN, indicating that the electron transfer from MeCN to BMEPZ

in any oxidation state during the battery operation is prohibited. Similarly, the electron transfer from BMEPZ in any oxidation state to MeCN is energetically unfavorable because the HOMO (or SOMO) levels of BMEPZ and BMEPZ²⁺ (or BMEPZ⁺) are lower than the LUMO level of MeCN. The above theoretical calculations indicate that parasitic side reactions based on electron transfer between BMEPZ and MeCN are less likely to occur during battery operation (Figure 2.24).

In addition, the structural changes in the optimized geometries of BMEPZ during the redox reactions were observed. As shown in Figure 2.22c, the neutral BMEPZ has bent conformation with an angle of 144.2° between the two phenyl ring planes. The radical cation and dication, in contrast, show almost planar geometries with the angles of 171.2° and 175.4°, respectively. It can be speculated that the planar molecular geometries of the radical cation and dication effectively delocalized the additional charges, leading to the remarkable redox stability of BMEPZ.^{62,63} It is noteworthy that many p-type ROMs except BMEPZ tend to be very unstable when they are oxidized by two electrons, resulting in fast decay of the cycle performance.^{13,30}

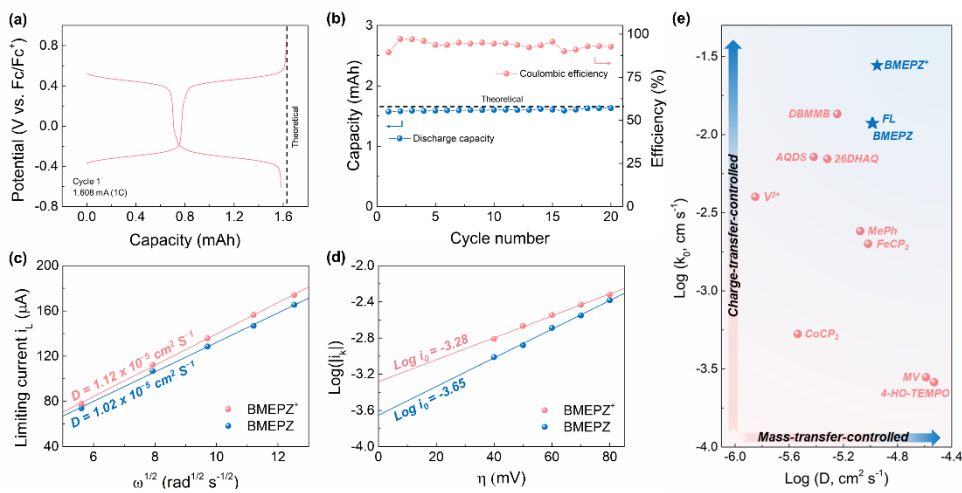


Figure 2.19. Characterization of BMEPZ. a) Representative charge–discharge curve for bulk-electrolysis test of BMEPZ. b) Coulombic efficiencies and capacities for bulk-electrolysis test of BMEPZ with respect to cycle number. c) Linearly fitted Levich plots of limiting current (i_L) as a function of the square root of the rotation rate ($\omega^{-1/2}$). d) Linearly fitted plots of logarithm of kinetics-controlled current ($\log i_k$) as a function of overpotential (η). e) Comparison of kinetic parameters (kinetic rate constant (k_0) and diffusion coefficient (D)) of reported redox-active materials in RFB system: this work (blue stars) and reported RFBs (pink circles).

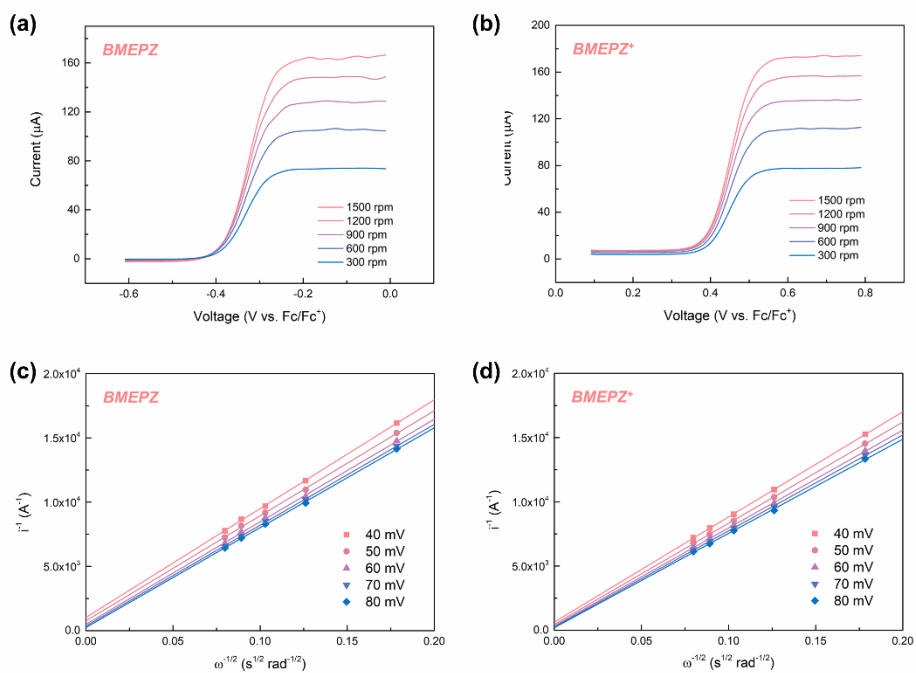


Figure 2.20. LSV curves of a) BMEPZ and b) BMEPZ⁺ for rotation rates of 300–1500 rpm at a scan rate of 5 mV s⁻¹. Linearly fitted Koutecký-Levich plots of c) BMEPZ and d) BMEPZ⁺ at various overpotentials.

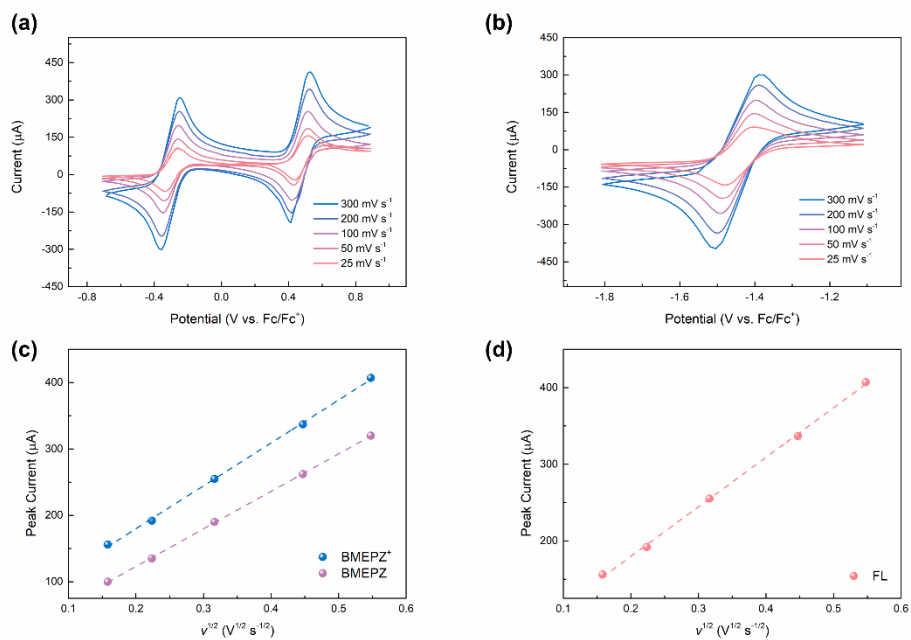


Figure 2.21. Scan-rate dependence CV study for a) BMEPZ and b) FL, and Randles-Sevcik plot of c) BMEPZ and d) FL.

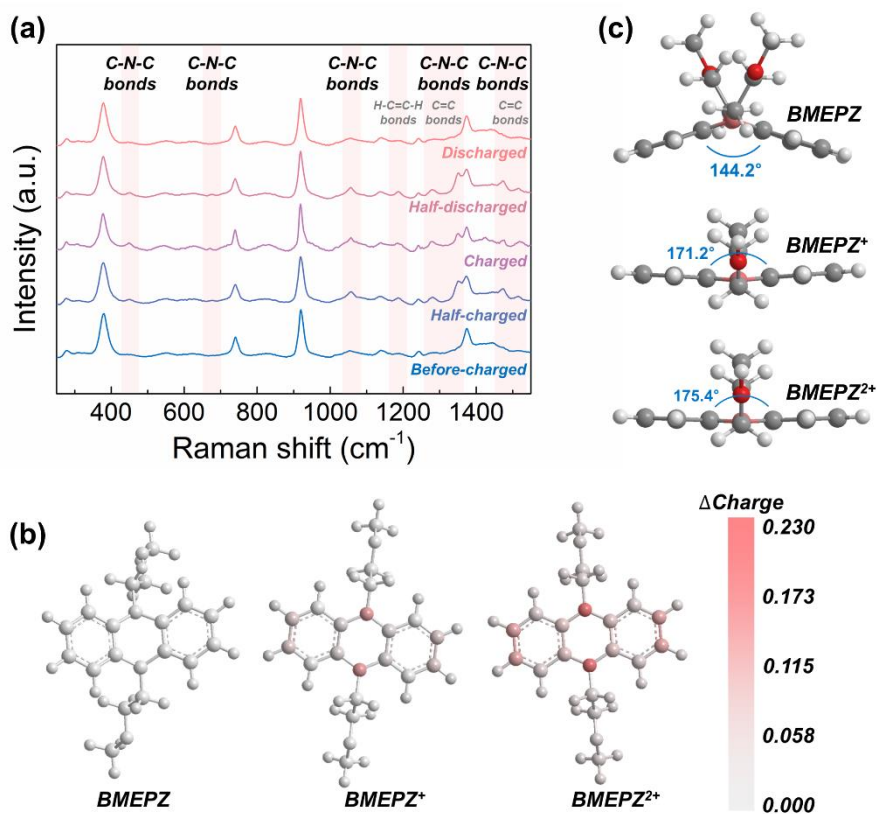


Figure 2.22. Investigation of redox mechanism of BMEPZ. a) *Ex situ* Raman analysis for BMEPZ in catholyte, demonstrating the reversible appearance and disappearance of several peaks. b) NPA of BMEPZ, BMEPZ⁺, and BMEPZ²⁺. The depth of the pink color denotes the extent of the charge change. c) Molecular geometries of BMEPZ, BMEPZ⁺, and BMEPZ²⁺.

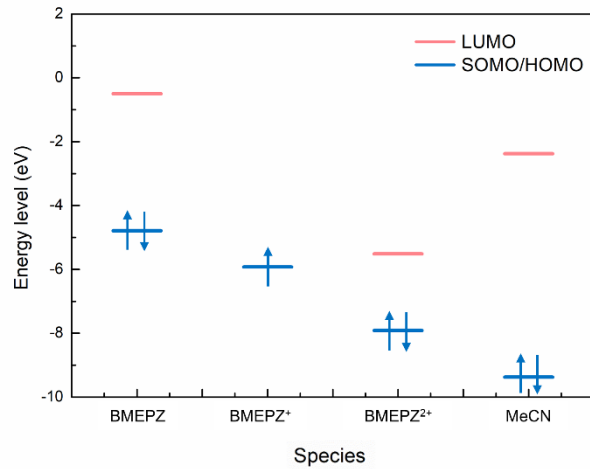


Figure 2.24. Frontier molecular orbital (FMO) energies of BMEPZ, BMEPZ⁺, BMEPZ²⁺, and MeCN. Note that the energy states of BMEPZ change with the oxidation due to the relaxation effect of the molecules.

2.2.3.3 Electrochemical performance of BMEPZ/FL flow cell

Cycling tests of flow cells employing BMEPZ as the catholyte and FL as the anolyte were performed using a custom flow cell (see the Methods section for further details) to investigate the electrochemical performance in a near-practical system. Figure 2.25a presents a representative charge–discharge curve for the dilute condition of 0.05 M BMEPZ and 0.1 M FL in a supporting electrolyte of 0.5 M bis(trifluoromethane)sulfonimide lithium salt (LiTFSI) in MeCN at a current density of 20 mA cm^{-2} . The flow cell exhibited two well-defined plateaus at cell voltages of 1.2 and 2.0 V, which is consistent with the expectations from the CV curves in Figure 2.15b. The plateaus of the same length at each voltage indicate that the two single-electron redox reactions of BMEPZ contribute equally to the cell capacity in the flow cell system. Additionally, we observed the color changes of the catholyte during redox reactions, which are presented as a function of the state of charge (SOC) with a step size of SOC 25 in Figure 2.25a. The color changes roughly occurred in two distinct stages, from yellow to green and from green to red, because of the double-redox reactions of BMEPZ, which could be quantitatively probed using UV–vis spectroscopy (Figure 2.26). The cycling efficiencies and capacity retention of the flow cell are plotted in Figure 2.25b. The cycling of the flow cell has a coulombic efficiency of $\sim 96\%$ with an energy efficiency of $\sim 70\%$, which were stably maintained over 200 cycles. Moreover, an initial discharge capacity of 2.08 Ah L^{-1} was achieved, which is close to the theoretical capacity of 2.67 Ah L^{-1} and yields a material utilization of $\sim 80\%$. Note that the initial capacity could be retained over 200

cycles (cycling time of ~129 h) with a capacity retention of 99.94% per cycle and 70% of theoretical capacity could be achieved after 200 cycles (Figure 2.27). We attribute this highly robust cycle performance of the cell to the high stability of BMEPZ⁺ radical cation in the electrolyte as well as the stable dication form of BMEPZ. Typically, organic radicals are often highly reactive and thus unstable, which is the key obstacle for improving the cycle performance in organic flow battery. In contrast, it is noteworthy that the UV-vis spectra of BMEPZ⁺ in the electrolyte were virtually unchanged over 24 hours (Figure 2.28), indicating that BMEPZ⁺ has superior radical stability.^{12,64}

We next performed a demonstration of the flow cell under the near-saturation condition of BMEPZ to investigate the electrochemical behavior under practical cell conditions. In Figure 2.29a, additional charge–discharge curves for flow cells using 0.1 M and 0.4 M BMEPZ are presented. A proportional elevation of the capacity was observed with respect to the concentration, and stable cycling of 99.94% per cycle was achieved for the 0.1 M BMEPZ flow cell in Figure 2.29b. In addition, the 0.4 M BMEPZ flow cell was successfully demonstrated with a material utilization of ~75% during discharge and a respectable capacity retention of 99.3% per cycle in Figure 2.29c. Despite the superior stability of BMEPZ at all redox states, the capacity decay in concentrated cell was non-negligible. Since longer cycling time was needed for the concentrated cell at the same current density, more ROM molecules would cross over through the microporous separator, represented by the low coulombic efficiency of 83%. Moreover, during the extended cycling time, the

FL radical anions at the charged state might have more chance to decay due to their rather short lifetime.¹² It can thus be expected that the development of membrane which can suppress the cross-over issue and using more stable anolyte material would improve cycle life in the concentrated cell. For comparison of the performance of the BMEPZ/FL flow cell with that of previously reported all-organic RFBs involving both aqueous and non-aqueous media, the theoretical energy densities of the RFBs at the cycling concentration are plotted in Figure 2.29d. The energy densities of the RFBs are presented with respect to the intrinsic activity of the redox couple (energy per mole) and its concentration in the solvent (energy per volume). With regard to the dynamic properties of solvents and cost issue, the molar energy density should be considered because ROMs with high molar energy densities are advantageous to deliver high energy densities using relatively low concentrations of ROMs. The figure shows that AORFBs (yellow areas) generally exhibit low intrinsic energy densities limited by the low cell voltage (<1.4 V); therefore, a high-concentration electrolyte is required to achieve a high volumetric energy density. For instance, Janoschka *et al.* demonstrated the high volumetric energy density (38 Wh L⁻¹), which is comparable to the vanadium RFBs; but it needed 2.0 M solutions of TEMPO derivative and methyl viologen.³⁹ In contrast, a relatively high molar energy density can be attained for NORFBs (purple areas) because of the wide electrochemical window. Furthermore, NORFBs using multi-redox ROMs present a promising pathway to realize high volumetric energy density with exceptionally high molar energy densities, as illustrated in blue areas. However, in practice, their

volumetric energy density rarely exceeds that of aqueous RFBs because of the relatively low cycling concentration limited by the dynamic properties of non-aqueous media and the lack of suitable membrane. As the multi-redox capability is combined with enhanced solubility in the BMEPZ/FL system, the volumetric energy density ($\sim 17 \text{ Wh L}^{-1}$) exceeded that of other NORFBs even at a lower concentration ($\sim 0.4 \text{ M}$), showing a great potential of multi-redox NORFB systems. It can be expected that further engineering to achieve solubility of phenazine derivatives over 1 M and the development of high performance membrane for non-aqueous system would enable the phenazine-based NORFB to outperform vanadium-based and aqueous organic systems.

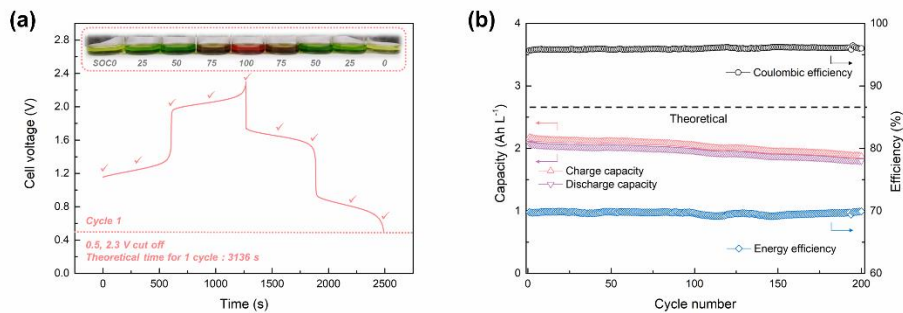


Figure 2.25. Electrochemical performance of flow cell of 50 mM BMEPZ and 0.1 M FL. a) Representative cell voltage vs. time profile at a current density of 20 mA cm⁻². The inset shows the color change of the catholyte as a function of the SOC. b) Cycling efficiencies and capacities with respect to cycle number.

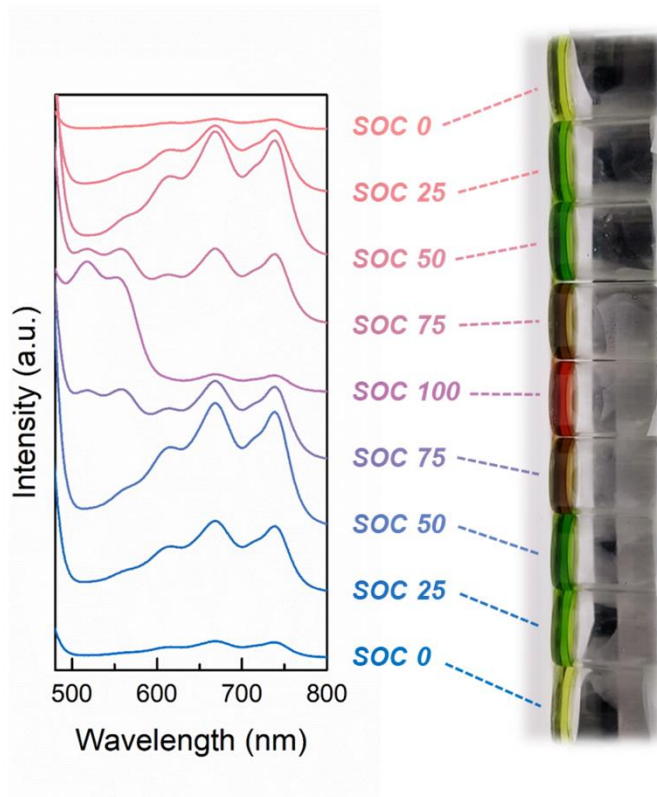


Figure 2.26. UV-vis spectra corresponding to the colors of the BMEPZ catholyte at the given SOC levels.

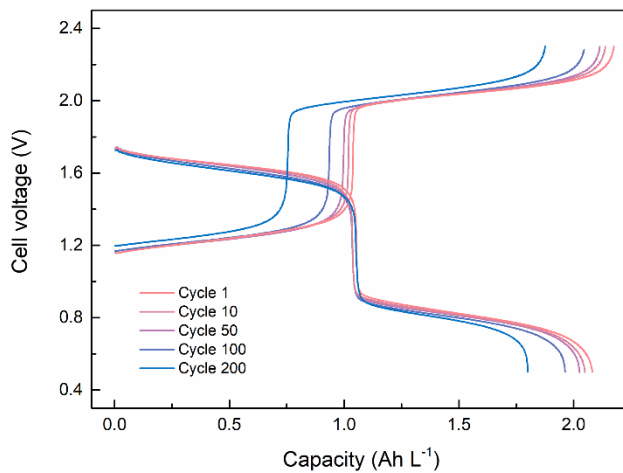


Figure 2.27. Charge–discharge curves for 0.05 M BMEPZ and 0.1 M FL with respect to the cycle number.

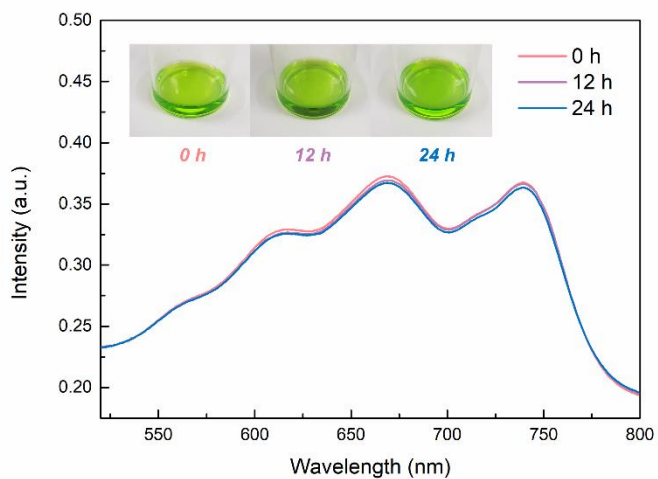


Figure 2.28. UV-vis spectra of BMEPZ⁺ in the catholyte at the SOC 50, obtained at 0, 12, and 24 h after sampling. The color and spectra of the catholyte solution are well maintained over 24 hours.

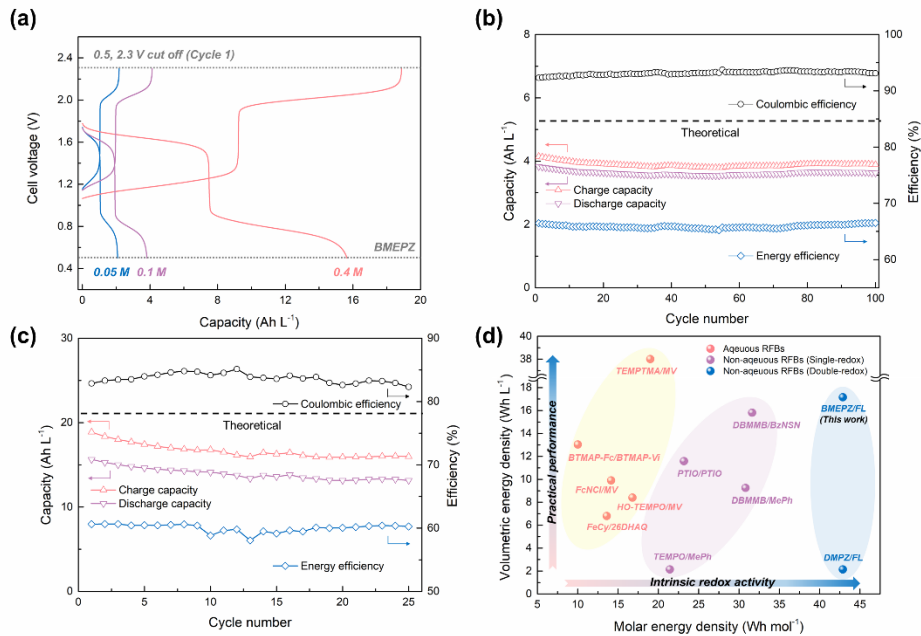


Figure 2.29. Electrochemical performance of BMEPZ/FL flow cell at high concentrations. a) Typical charge–discharge curves at different concentrations. b) Cycling efficiencies and capacities for 0.1 M BMEPZ and 0.2 M FL with respect to cycle number. c) Cycling efficiencies and capacities for 0.4 M BMEPZ and 0.8 M FL with respect to cycle number. d) Energy density plot of typical redox-active materials in organic RFBs. The molar energy density is the volumetric energy density divided by the cycling concentration.

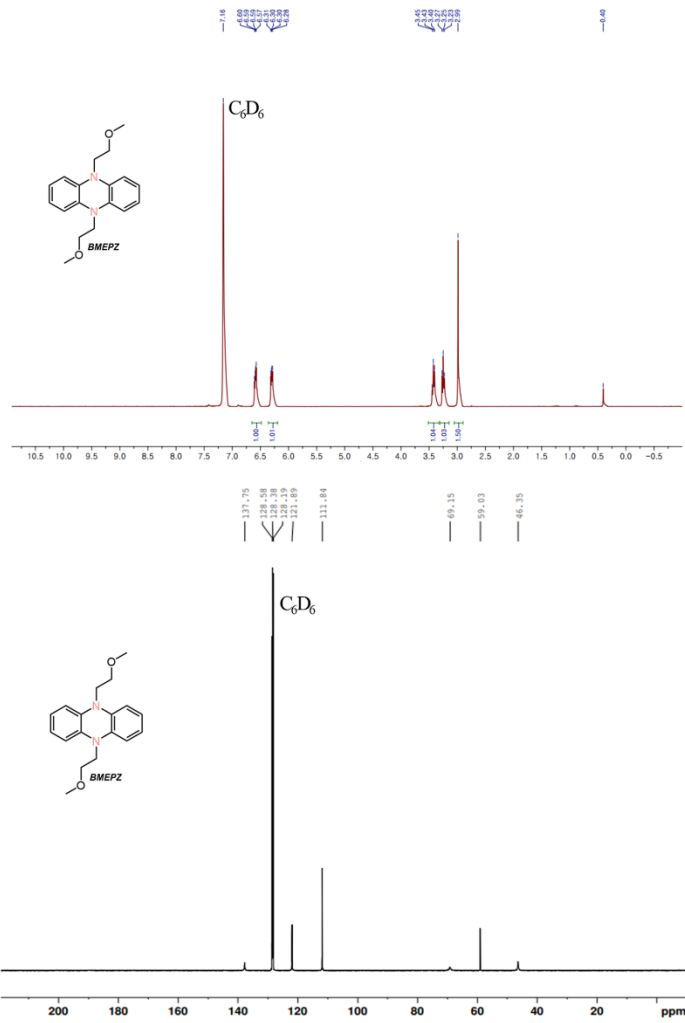


Figure 2.30. 1H - (top) and ^{13}C -NMR (bottom) spectra of BMEPZ in C_6D_6 .

2.2.4 Concluding remarks

We reported a multi-redox BMEPZ inspired by bio-systems as a promising catholyte material with the highest energy density demonstrated for organic RFBs. This ROM undergoes two reversible redox reactions at high redox potentials of -0.29 and 0.50 V vs. Fc/Fc^+ and exhibits outstanding electrochemical kinetics for the mass- and charge-transfer processes, retaining high solubility in non-aqueous media. An all-organic flow cell exploiting the BMEPZ/FL redox couple was successfully prepared with two well-defined voltage plateaus at 1.2 and 2 V and highly robust cycling owing to the remarkable chemical stability, delivering one of the highest energy density of reported NORFBs. Although further engineering of ROMs and the development of high performance membrane are still needed for practical application of this system, these findings on a new multi-electron redox material combined with the high solubility provide a breakthrough in the realization of high-energy-density RFBs.

2.2.5 References

- 1 Yang, Z. *et al.* Electrochemical energy storage for green grid. *Chem. Rev.* **111**, 3577-3613 (2011).
- 2 Dunn, B., Kamath, H. & Tarascon, J.-M. Electrical energy storage for the grid: a battery of choices. *Science* **334**, 928-935 (2011).
- 3 Soloveichik, G. L. Flow batteries: current status and trends. *Chem. Rev.* **115**, 11533-11558 (2015).
- 4 Wang, Y., He, P. & Zhou, H. Li-Redox Flow Batteries Based on Hybrid Electrolytes: At the Cross Road between Li-ion and Redox Flow Batteries. *Adv. Energy Mater.* **2**, 770-779 (2012).
- 5 Darling, R. M., Gallagher, K. G., Kowalski, J. A., Ha, S. & Brushett, F. R. Pathways to low-cost electrochemical energy storage: a comparison of aqueous and nonaqueous flow batteries. *Energy Environ. Sci.* **7**, 3459-3477 (2014).
- 6 Nguyen, T. & Savinell, R. F. Flow batteries. *Electrochem. Soc. Interface* **19**, 54 (2010).
- 7 Noack, J., Roznyatovskaya, N., Herr, T. & Fischer, P. The chemistry of redox-flow batteries. *Angew. Chem., Int. Ed.* **54**, 9776-9809 (2015).
- 8 Sevov, C. S., Samaroo, S. K. & Sanford, M. S. Cyclopropenium Salts as Cyclable, High-Potential Catholytes in Nonaqueous Media. *Adv. Energy Mater.* **7**, 1602027 (2017).
- 9 Winsberg, J., Hagemann, T., Janoschka, T., Hager, M. D. & Schubert, U. S.

- Redox-flow batteries: from metals to organic redox-active materials. *Angew. Chem., Int. Ed.* **56**, 686-711 (2017).
- 10 Wei, X. *et al.* Materials and systems for organic redox flow batteries: status and challenges. *ACS Energy Lett.* **2**, 2187-2204 (2017).
- 11 Park, M., Ryu, J., Wang, W. & Cho, J. Material design and engineering of next-generation flow-battery technologies. *Nature Reviews Materials* **2**, 16080 (2017).
- 12 Wei, X. *et al.* Radical compatibility with nonaqueous electrolytes and its impact on an all-organic redox flow battery. *Angew. Chem., Int. Ed.* **54**, 8684-8687 (2015).
- 13 Milshtein, J. D. *et al.* High current density, long duration cycling of soluble organic active species for non-aqueous redox flow batteries. *Energy Environ. Sci.* **9**, 3531-3543 (2016).
- 14 Ding, Y., Zhao, Y., Li, Y., Goodenough, J. B. & Yu, G. A high-performance all-metallocene-based, non-aqueous redox flow battery. *Energy Environ. Sci.* **10**, 491-497 (2017).
- 15 Duan, W. *et al.* “Wine-Dark Sea” in an organic flow battery: storing negative charge in 2, 1, 3-benzothiadiazole radicals leads to improved cyclability. *ACS Energy Lett.* **2**, 1156-1161 (2017).
- 16 Ding, Y., Li, Y. & Yu, G. Exploring bio-inspired quinone-based organic redox flow batteries: a combined experimental and computational study. *Chem* **1**, 790-801 (2016).

- 17 Chen, H., Zhou, Y. & Lu, Y.-C. Lithium-Organic Nanocomposite Suspension for High-Energy-Density Redox Flow Batteries. *ACS Energy Lett.* **3**, 1991-1997 (2018).
- 18 Zhao, Q., Zhu, Z. & Chen, J. Molecular engineering with organic carbonyl electrode materials for advanced stationary and redox flow rechargeable batteries. *Adv. Mater.* **29**, 1607007 (2017).
- 19 Kang, N. *et al.* Nanoparticulate iron oxide tubes from microporous organic nanotubes as stable anode materials for lithium ion batteries. *Angew. Chem., Int. Ed.* **51**, 6626-6630 (2012).
- 20 Benniston, A. C., Hagon, J., He, X., Yang, S. & Harrington, R. W. Spring Open Two-plus-Two Electron Storage in a Disulfide-Strapped Methyl Viologen Derivative. *Organic letters* **14**, 506-509 (2012).
- 21 Song, Z. & Zhou, H. Towards sustainable and versatile energy storage devices: an overview of organic electrode materials. *Energy Environ. Sci.* **6**, 2280-2301 (2013).
- 22 Lee, S. *et al.* Recent progress in organic electrodes for Li and Na rechargeable batteries. *Adv. Mater.*, 1704682 (2018).
- 23 Luo, J., Hu, B., Debruler, C. & Liu, T. L. A π -conjugation extended viologen as a two-electron storage anolyte for total organic aqueous redox flow batteries. *Angew. Chem., Int. Ed.* **57**, 231-235 (2018).
- 24 Lin, K. *et al.* Alkaline quinone flow battery. *Science* **349**, 1529-1532 (2015).
- 25 Liu, T., Wei, X., Nie, Z., Sprenkle, V. & Wang, W. A total organic aqueous

- redox flow battery employing a low cost and sustainable methyl viologen anolyte and 4-HO-TEMPO catholyte. *Adv. Energy Mater.* **6**, 1501449 (2016).
- 26 Yang, Z. *et al.* Alkaline Benzoquinone Aqueous Flow Battery for Large-Scale Storage of Electrical Energy. *Adv. Energy Mater.* **8**, 1702056 (2018).
- 27 Huskinson, B. *et al.* A metal-free organic–inorganic aqueous flow battery. *Nature* **505**, 195 (2014).
- 28 Kwabi, D. G. *et al.* Alkaline Quinone Flow Battery with Long Lifetime at pH 12. *Joule* **2**, 1894-1906 (2018).
- 29 Zhang, C. *et al.* Progress and prospects of next-generation redox flow batteries. *Energy Storage Mater.* **15**, 324-350 (2018).
- 30 Wei, X. *et al.* A high-current, stable nonaqueous organic redox flow battery. *ACS Energy Lett.* **1**, 705-711 (2016).
- 31 Wei, X. *et al.* TEMPO-based catholyte for high-energy density nonaqueous redox flow batteries. *Adv. Mater.* **26**, 7649-7653 (2014).
- 32 Zhang, J. *et al.* Solution Properties and Practical Limits of Concentrated Electrolytes for Nonaqueous Redox Flow Batteries. *J. Phys. Chem. C* **122**, 8159-8172 (2018).
- 33 Li, Z. & Lu, Y.-C. Redox Flow Batteries: Want More Electrons? Go Organic! *Chem* **4**, 2020-2021 (2018).
- 34 Kim, H.-s., Lee, K.-J., Han, Y.-K., Ryu, J. H. & Oh, S. M. A comparative study on the solubility and stability of p-phenylenediamine-based organic

- redox couples for non-aqueous flow batteries. *J. Power Sources* **348**, 264-269 (2017).
- 35 Kowalski, J. A. *et al.* A stable two-electron-donating phenothiazine for application in nonaqueous redox flow batteries. *J. Mater. Chem. A* **5**, 24371-24379 (2017).
- 36 Kwon, G. *et al.* Multi-redox molecule for high-energy redox flow batteries. *Joule* **2**, 1771-1782 (2018).
- 37 Li, L. *et al.* A stable vanadium redox-flow battery with high energy density for large-scale energy storage. *Adv. Energy Mater.* **1**, 394-400 (2011).
- 38 Kear, G., Shah, A. A. & Walsh, F. C. Development of the all-vanadium redox flow battery for energy storage: a review of technological, financial and policy aspects. *International journal of energy research* **36**, 1105-1120 (2012).
- 39 Janoschka, T., Martin, N., Hager, M. D. & Schubert, U. S. An Aqueous Redox-Flow Battery with High Capacity and Power: The TEMPTMA/MV System. *Angew. Chem., Int. Ed.* **55**, 14427-14430 (2016).
- 40 Sugimoto, A., Kotani, T., Tsujimoto, J. & Yoneda, S. Preparation and properties of electron donor acceptor complexes of the compounds having capto-dative substituents. *Journal of Heterocyclic Chemistry* **26**, 435-438 (1989).
- 41 Frisch, M. J. *et al.* Gaussian 09, revision A. 1. *Gaussian Inc. Wallingford CT* **27**, 34 (2009).

- 42 Lee, C., Yang, W. & Parr, R. G. Development of the Colle-Salvetti correlation-energy formula into a functional of the electron density. *Phys. Rev. B* **37**, 785-789, doi:10.1103/PhysRevB.37.785 (1988).
- 43 Becke, A. D. Density-functional thermochemistry. III. The role of exact exchange. *J. Chem. Phys.* **98**, 5648-5652 (1993).
- 44 Stephens, P., Devlin, F., Chabalowski, C. & Frisch, M. J. Ab initio calculation of vibrational absorption and circular dichroism spectra using density functional force fields. *The Journal of Physical Chemistry* **98**, 11623-11627 (1994).
- 45 Schäfer, A., Huber, C. & Ahlrichs, R. Fully optimized contracted Gaussian basis sets of triple zeta valence quality for atoms Li to Kr. *J. Chem. Phys.* **100**, 5829-5835, doi:10.1063/1.467146 (1994).
- 46 Klaumünzer, B., Kröner, D. & Saalfrank, P. (TD-) DFT calculation of vibrational and vibronic spectra of riboflavin in solution. *J. Phys. Chem. B* **114**, 10826-10834 (2010).
- 47 Lim, H.-D. *et al.* Rational design of redox mediators for advanced Li–O₂ batteries. *Nat. Energy* **1**, 16066 (2016).
- 48 Lee, M. *et al.* Multi-electron redox phenazine for ready-to-charge organic batteries. *Green Chem.* **19**, 2980-2985 (2017).
- 49 Hong, J. *et al.* Biologically inspired pteridine redox centres for rechargeable batteries. *Nat. Commun.* **5**, 5335 (2014).
- 50 Beifuss, U., Tietze, M., Bäumer, S. & Deppenmeier, U. Methanophenazine:

- structure, total synthesis, and function of a new cofactor from methanogenic archaea. *Angew. Chem., Int. Ed.* **39**, 2470-2472 (2000).
- 51 Pierson, L. S. & Pierson, E. A. Metabolism and function of phenazines in bacteria: impacts on the behavior of bacteria in the environment and biotechnological processes. *Applied microbiology and biotechnology* **86**, 1659-1670 (2010).
- 52 Hollas, A. *et al.* A biomimetic high-capacity phenazine-based anolyte for aqueous organic redox flow batteries. *Nat. Energy* **3**, 508-514 (2018).
- 53 Rada, B. & Leto, T. L. Pyocyanin effects on respiratory epithelium: relevance in *Pseudomonas aeruginosa* airway infections. *Trends in microbiology* **21**, 73-81 (2013).
- 54 Tietze, M. *et al.* Redox potentials of methanophenazine and CoB-S-S-CoM, factors involved in electron transport in methanogenic archaea. *Chembiochem* **4**, 333-335 (2003).
- 55 Wang, Y. & Newman, D. K. Redox reactions of phenazine antibiotics with ferric (hydr) oxides and molecular oxygen. *Environ. Sci. Technol.* **42**, 2380-2386 (2008).
- 56 Zhang, J. *et al.* Annulated Dialkoxybenzenes as Catholyte Materials for Non-aqueous Redox Flow Batteries: Achieving High Chemical Stability through Bicyclic Substitution. *Adv. Energy Mater.* **7**, 1701272 (2017).
- 57 Kowalski, J. A., Su, L., Milshtein, J. D. & Brushett, F. R. Recent advances in molecular engineering of redox active organic molecules for nonaqueous

- flow batteries. *Current Opinion in Chemical Engineering* **13**, 45-52 (2016).
- 58 Wang, W. *et al.* Anthraquinone with tailored structure for a nonaqueous metal–organic redox flow battery. *Chem. Commun.* **48**, 6669-6671 (2012).
- 59 Wei, X. *et al.* Microporous separators for Fe/V redox flow batteries. *J. Power Sources* **218**, 39-45 (2012).
- 60 Bard, A. J. & Faulkner, L. R. *Fundamentals and Applications* (Springer, 2002).
- 61 Compton, R. G. & Banks, C. E. *Understanding voltammetry* (World Scientific, 2011).
- 62 Chiykowski, V. A., Lam, B., Du, C. & Berlinguette, C. P. Comparative analysis of triarylamine and phenothiazine sensitizer donor units in dye-sensitized solar cells. *Chem. Commun.* **53**, 2367-2370 (2017).
- 63 Narayana, K. A. *et al.* N-Substituted Phenothiazine Derivatives: How the Stability of the Neutral and Radical Cation Forms Affects Overcharge Performance in Lithium-Ion Batteries. *ChemPhysChem* **16**, 1179-1189 (2015).
- 64 Armstrong, C. G. & Toghiani, K. E. Stability of molecular radicals in organic non-aqueous redox flow batteries: A mini review. *Electrochem. Commun.* **91**, 19-24 (2018).

Chapter 3. Rational design of an organic material with exceptional chemical stability for highly stable organic redox flow batteries

(The essence of this chapter has been published in *Energy Storage Materials*. Reproduced with permission from [Kwon, G. *et al.*, *Energy Storage Mater.* **2021**, 42, 185-192] Copyright (2021) Elsevier)

3.1 Research background

Global concerns over greenhouse gas emissions have driven increasing demands for a rapid transition from fossil fuels to renewable energy sources such as solar and wind power.¹ However, the associated intermittent energy supplies and geographical limitations critically restrict the efficient utilization of these power sources, requiring combination with large-scale energy storage systems (ESSs) to enable round-the-clock energy delivery.²⁻⁴ Among the various options for ESSs, redox flow batteries (RFBs) have been widely considered promising scalable systems.⁵⁻⁷ Because the storage of the active components can be decoupled from the electrochemical reaction sites in RFBs, decoupling of power and energy is feasible, which offers design flexibilities in the architecture of the ESSs for various applications.⁸ Extensive research efforts have led to the introduction of several types of RFBs beyond the conventional vanadium- or zinc/bromine-based RFBs.⁹ Organic RFBs (ORFBs), which use redox-active organic materials (ROMs), have shown

particularly great promise, benefiting from the unique features of ROMs such as cost effectiveness and chemical tunability.¹⁰ ROMs are composed of earth-abundant elements such as H, C, O, and N, and their synthetic tunability enables designed control of the solubility and voltage depending on the electrolytes in the RFBs.^{11,12}

Over the past decade, remarkable progress has been made in ORFBs, leading to significant improvements in their energy density and efficiency that have allowed them to compete with their inorganic-based counterparts.¹³ Nevertheless, the cycle performance of ORFBs remains far behind that of conventional RFBs and has been the critical hurdle for their practical application.¹⁴ It has been widely discussed that the highly reactive radical forms of ROMs, especially in the charged state, induce significant deterioration of the system stability and serve as one of the major contributors to the poor cycling performance of ORFBs.^{12,14,15} The high charge density typically localized on a few atoms in the molecule often leads to unstable charged states of ROMs, which are prone to undergoing undesirable chemical reactions such as molecular decomposition, dimerization, and side reactions with electrolytes.¹⁵⁻¹⁷ Many efforts have thus been made to enhance the chemical stability of ROMs, such as providing steric hindrance by introducing additional structural units to geometrically protect the ROMs from side reactions.¹⁸⁻²² However, the long-term cycling performance of ORFBs remains unsatisfactory, and such strategies generally require the additional introduction of bulky functional groups, which are often disadvantageous in terms of cost, solubility, and molecular kinetics.¹²

Identifying an intrinsically stable redox motif, whose charged state is resonance stabilized over the molecular structure, is one alternative route toward stable ORFBs.^{17,23} For this feature of ROMs, we paid particular attention to the molecular structure of triphenylamine (TPA) derivatives, which allow facile resonance delocalization of charge through π -electron systems and possess a large number of resonance structures.^{24,25} It has been widely reported that TPA structures can readily disperse the positive charge generated on the nitrogen atom over three adjacent phenyl rings upon redox reaction.²⁶⁻²⁸ In addition, as a result of their high stability in the charged state and hole-transport properties, they have been extensively employed in organic electronics,^{24,29,30} including organic light-emitting diodes (OLEDs)³¹⁻³³ and organic photovoltaics (OPVs).^{34,35} Moreover, it was presumed that the propeller-like molecular structures of TPA would effectively hinder intermolecular aggregation and would thus be easily dissolved in various organic solvents,³⁶ which would also be beneficial for RFB applications. With this motivation, herein, we present a novel catholyte that exploits a TPA-based molecule with augmented resonance stabilization, tris(4-methoxyphenyl)amine or 3MTPA, which is unprecedentedly stable in a charged state. It is demonstrated that through tailored end-capping of TPA using methoxy groups, 3MTPA can undergo a highly reversible redox reaction and become substantially soluble in an acetonitrile (MeCN) solvent. Careful comparisons with previously reported ROMs confirm that 3MTPA exhibits outstanding stability in various charged states with nearly no capacity decay even after 168 h storage at 50°C. We also demonstrate that in long-term flow cell

cycling, a symmetric cell using 3MTPA displays a markedly robust capacity retention of 99.998% per cycle over 1400 cycles, which is one of the highest cycling performances reported to date.

3.2 Experimental method

3.2.1 Preparation of materials and characterization

MeCN (anhydrous) and a microporous separator (Celgard 4560) were purchased from Sigma–Aldrich and Wellcos (Korea) and used without further purification. LiTFSI was purchased from TCI Chemicals and treated under vacuum at 70 °C for 24 h to remove moisture. All the starting materials and reagents for synthesis were purchased from commercial suppliers (Sigma–Aldrich, Alfa Aesar, or TCI Chemicals) and used without further purification. Toluene was distilled using sodium/benzophenone before use, and all the reactions were performed under an argon atmosphere. All the glassware, syringes, magnetic stirring bars, and needles were thoroughly dried in a convection oven. The reactions were monitored using thin layer chromatography (TLC) using commercial TLC plates (silica gel 60 F254, Merck Co.). The crude reaction mixtures were separated using silica gel column chromatography. ¹H-NMR and ¹³C-NMR spectra were recorded on a Bruker Avance-300 and Avance-500 NMR spectrometer, respectively. High-resolution mass spectrometry (HRMS) spectra were obtained using a JEOL JMS-700 instrument. In the solubility measurement, 67.1 mg of 3MTPA powder was first fully dissolved in 2 mL of MeCN to make a 0.1 M solution. Then, the same amount (67.1 mg) of 3MTPA powder was repeatedly added to the solution until it became saturated

without further dissolution.

3.2.2 Electrochemical measurements

The electrolytes were prepared and evaluated in an Ar-filled glove box (<0.5 ppm O₂, H₂O). CV curves of TPA and 3MTPA (10 mM each) were captured using a supporting electrolyte of 0.1 M LiTFSI in MeCN. A three-electrode system (Pt counter electrode, Ag/AgNO₃ reference electrode, and glassy carbon working electrode) was employed using a scan rate of 100 mV s⁻¹.

For the RDE experiment, a three-electrode system (Pt counter electrode, Ag/AgNO₃ reference electrode, and glassy carbon working electrode with 5-mm diameter) was employed for the LSV tests. Rotation rates from 300 to 1500 rpm (in increments of 300 rpm) were adopted using a modulated speed rotator (AFMSRX; PINE). The LSV curves were obtained with 1.0 mM 3MTPA in 0.5 M LiTFSI in MeCN at a scan rate of 5 mV s⁻¹. The kinematic viscosity (ν) of 0.59 mm² s⁻¹ was used for the supporting electrolyte of 0.5 M LiTFSI in MeCN.²¹ The diffusion coefficient (D) of 3MTPA was calculated using the Levich equation (eq. 1) based on the slope of 1.36×10^{-5} A rad^{-1/2} s^{1/2} in the Levich plot. The Koutecký–Levich plot was constructed at different overpotentials using the Koutecký–Levich equation (eq. 2), and the kinetic rate constant of 3MTPA was determined using eq. 3.

$$i_L = 0.62nFAD^{2/3}\omega^{1/2}\nu^{-1/6}C_0 \quad (1)$$

$$\frac{1}{i} = \frac{1}{i_k} + \frac{1}{0.62nFAD^{2/3}\omega^{1/2}\nu^{-1/6}C_0} \quad (2)$$

$$i_0 = nFAk_0C_0 \quad (3)$$

Here, n is the number of electrons transferred ($n = 1$), F is the Faraday constant

($F = 96485 \text{ C mol}^{-1}$), A is the electrode area ($A = 0.2 \text{ cm}^2$), and C_0 is the concentration of the ROM ($C_0 = 1.0 \text{ mM}$).

A custom flow cell used in previous work was adopted using a piece of microporous separator (Celgard 4560).²¹ The symmetric flow cell was demonstrated using the neutral ROM and charged ROM for each side in the supporting electrolyte of 0.5 M LiTFSI in MeCN (11 mL for each electrolyte) with a flow rate of 80 mL min^{-1} using a pump (ShenChen) and the constant-current mode using a battery test system (WBCS 3000; WonA Tech, Korea). The charged electrolytes were obtained by the electrochemical method using FL for 3MTPA, MEEPT, PTIO, and TEMPO, and the charged electrolyte of FL was obtained using MEEPT. For the storage experiments, a concentration of 10 mM for the ROMs and a current density of 10 mA cm^{-2} were used. The volumetric capacity was calculated based on the electrolyte volume of 11 mL.

3.2.3 Computational details

Spin-unrestricted density functional theory (DFT)-type calculations were performed for geometry optimization, energy evaluation, and eigenvalue calculation using the Gaussian 09 package.³⁷ All the calculations were performed at the Becke–Lee–Yang–Parr (B3LYP) level of theory³⁸⁻⁴⁰ with the triple-zeta valence polarization (TZVP) basis set.^{41,42} A polarizable continuum model (PCM)^{43,44} was introduced for the entire calculation to model the solvation environment of MeCN. All the optimized structures were confirmed by the absence of imaginary frequencies. The Mercury software package⁴⁵ was used to analyze the molecular distortion during

ionization, including analysis of the angle between intramolecular planes.
Reorganization energy denotes energy difference between vertical and adiabatic ionization energy of the molecule.

3.3 Results and discussions

3.3.1 Design of TPA derivative for a stable catholyte (3MTPA)

Starting from the TPA motif, we designed an appropriate derivative for RFB application by anchoring methoxy groups at the para-position to achieve (i) the end-capping effect to hinder the potential dimerization and (ii) desirable solubility in MeCN-based electrolytes.²⁶ Importantly, it was anticipated that the methoxy functionalization would induce the mesomeric radical cation stabilization, further enhancing the stability of TPA. Therefore, it is expected that the effective charge delocalization, the prevention of potential molecular coupling, and the mesomeric effect synergistically enable high stability of newly designed ROM. The synthetic scheme of the TPA-based molecule is depicted in Figure 3.1, and the final 3MTPA product exhibited significant solubility (~0.7 M) in MeCN (see Experimental section for details). As shown in Figure 3.2a, it is supposed that the radical generated at the nitrogen atom of 3MTPA⁺ can be dispersed at ortho-, meta-, para-positions in each benzene ring by the Lewis structures, resulting in the large conjugation area based on the resonance structures via three conjugated benzene rings. Particularly, methoxy groups are effective in providing mesomeric electron density to further stabilize radical cation of 3MTPA⁺ as shown in Figure 3.2a.

The effective charge delocalization in the designed 3MTPA could be hinted from the visualization of the highest occupied molecular orbital (HOMO) and singly occupied molecular orbital (SOMO) calculated for 3MTPA and 3MTPA⁺, respectively, in Figure 3.2b. It is first noted that no apparent charge localization is

observed at the nitrogen atom for 3MTPA⁺. Moreover, unlike other representative ROMs such as MEEPT or TEMPO that undergo noticeable alteration in their electronic and geometrical structures during the redox reaction (Figure 3.3), the change in the molecular orbitals of 3MTPA appeared to be negligible after oxidation. Thus, it can be inferred that the entire 3MTPA molecule is involved in the redox reactions to a similar extent, which would contribute to radical stabilization.⁴⁶ We also estimated the chemical/electrochemical stability of 3MTPA and 3MTPA⁺ in a MeCN-based electrolyte by comparing their molecular orbital energies, as shown in Figure 3.2c. Both the HOMO and SOMO levels of 3MTPA and 3MTPA⁺ were located within the electrochemical window of MeCN, indicating the redox stability of 3MTPA in the MeCN-based electrolyte. Indeed, we experimentally verified the stable redox activity of 3MTPA in MeCN by conducting cyclic voltammetry (CV), as shown in Figure 3.2d. The CV results confirm that anodic and cathodic reactions occur reversibly at approximately 0.22 V (vs. Ag/Ag⁺) in the MeCN-based supporting electrolyte. This is in stark contrast to the case for the bare TPA without the methoxy functionalization, which exhibited irreversible redox behavior in the same CV experiment (Figure 3.4). The irreversible reaction of the TPA is attributable to the dimerization mainly occurring in the para position after oxidation²⁷ and supports the efficacy of the methoxy functionalization in stabilizing the TPA motif in the electrochemical system.

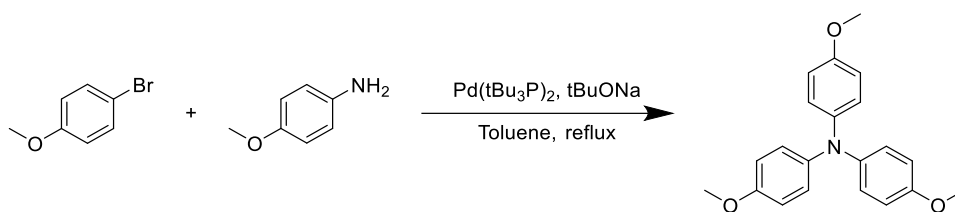


Figure 3.1. Synthetic route of 3MTPA. In a flame-dried two-necked round bottom flask, *p*-anisidine (1.00 g, 8.12 mmol), 4-bromoanisole (3.80 g, 20.3 mmol), sodium tert-butoxide (1.95 g, 20.3 mmol), and bis(tri-tert-butylphosphine)palladium(0) (80.0 mg, 0.16 mmol) were dissolved in freshly distilled toluene (30 ml). The solution was refluxed and stirred overnight. After cooling to room temperature, the reaction mixture was poured into water and extracted three times with dichloromethane. The organic layer was dried over anhydrous MgSO₄ and purified by column chromatography on silica gel with ethyl acetate/*n*-hexane (1:19 v/v) as an eluent. Recrystallization from methanol afforded a yellow powder. Yield: 73% (2.00 g), ¹H-NMR (500 MHz, CDCl₃) δ(ppm): 6.96 (s, 6H), 6.79 (d, J = 8.5 Hz, 6H), 3.77 (s, 9H); ¹³C-NMR (125 MHz, CDCl₃) δ(ppm): 115.12, 142.10, 125.03, 114.69, 55.71; HRMS (EI): calc. for C₄₂H₂₇N₃O₃ (M⁺), 335.1521; found, 335.1517

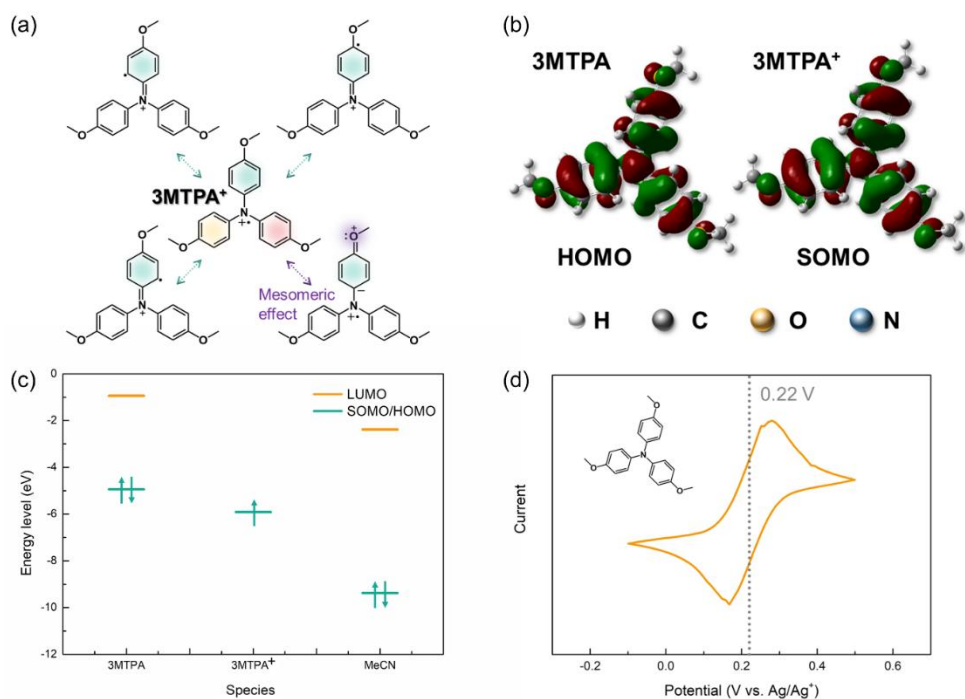


Figure 3.2. Highly stable catholyte 3MTPA. a) Resonance structures of 3MTPA. b) HOMO/LUMO and SOMO plots for 3MTPA and 3MTPA⁺, respectively, with isovalue of 0.02 (the green and red colors denote opposite signs of the wave function). c) Molecular orbital energies of 3MTPA, 3MTPA⁺, and MeCN. d) CV curve of 3MTPA at a scan rate of 100 mV s⁻¹.

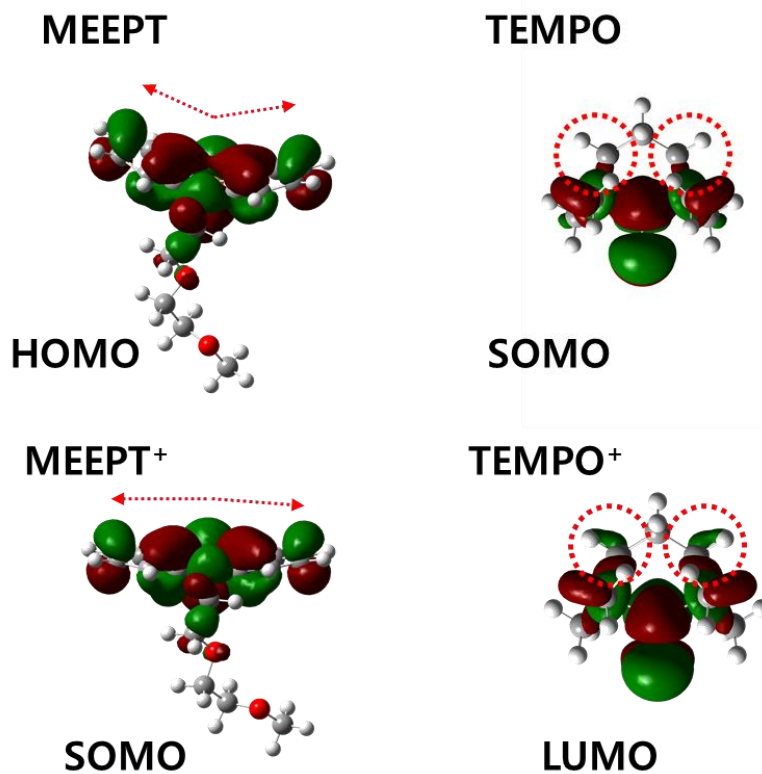


Figure 3.3. Molecular orbital plots for the representative ROMs, MEEPT and TEMPO. Note that there are noticeable changes of molecular orbitals and geometric structures for the redox reactions, as indicated by arrows and circles.

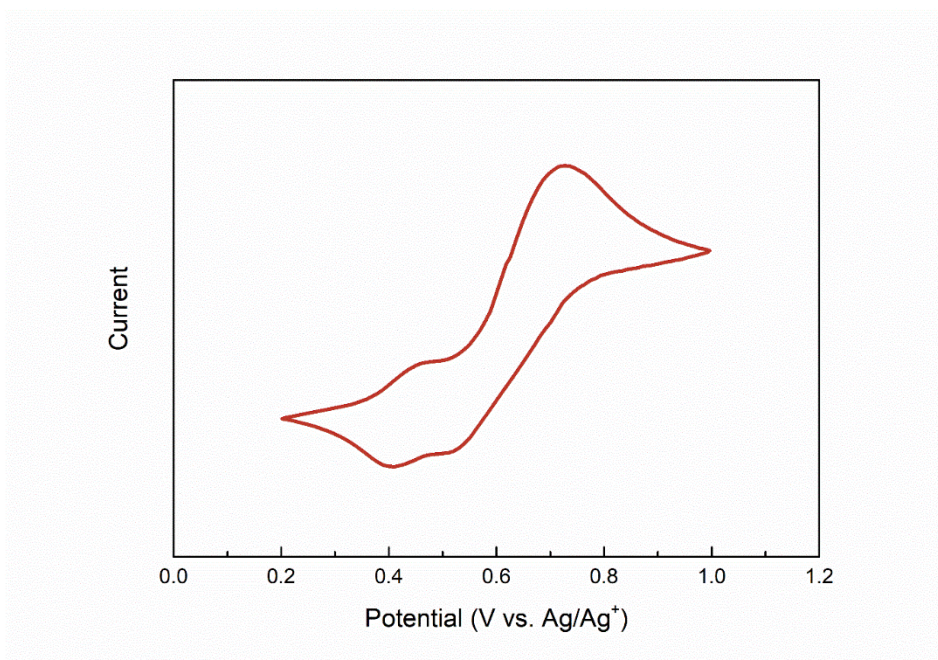


Figure 3.4. CV curve of TPA at the scan rate of 100 mV s^{-1} , exhibiting irreversible redox reaction of TPA.

3.3.2 Kinetic properties of 3MTPA catholyte

Inspired by the redox activity of 3MTPA, we attempted to further investigate the electrochemical and kinetic properties of the 3MTPA catholyte using rotating disk electrode (RDE) tests. The intrinsic kinetic parameters, including the diffusion coefficient and kinetic rate constant, were determined. Figure 3.5a presents the linear sweep voltammetry (LSV) curves captured with respect to the rotation rate (ω) in the range of 300–1500 rpm, which indicates the well-defined limiting current (i_L) at each ω . From the linear relationship between i_L and the square root of ω in Figure 3.5b, we calculated the diffusion coefficient (D) of 3MTPA to be $1.15 \times 10^{-5} \text{ cm}^2 \text{ s}^{-1}$ using the Levich equation⁴⁷. The charge-transfer-controlled kinetics were further analyzed, as shown in Figure 3.5c, by constructing Koutecký–Levich plots using the kinetic-controlled currents (i_k) for overpotentials (η) in the range of 40–80 mV (see more details in Figure 3.6). The exchange current ($\log i_0$) was shown to be approximately -3.21 , resulting in a kinetic rate constant (k_0) of $3.21 \times 10^{-2} \text{ cm s}^{-1}$. These values indicate that the kinetic properties of the 3MTPA catholyte are markedly superior in RFB systems. For quantitative comparison, the diffusion coefficients and kinetic rate constants of 3MTPA (yellow star) along with those of ROMs reported in RFBs (green circles) are presented on a logarithm scale in Figure 3.5d. It is apparent that 3MTPA outperforms the other redox-active materials in terms of kinetic properties with respect to both the mass- and charge-transfer rates. Notably, the kinetic rate constant of 3MTPA is one of the highest among reported ROMs.^{15,19,21,48-57} We attribute this intrinsically fast kinetic property to the negligible structural

reorganization of 3MTPA during the redox reaction. Consistent with the results of the HOMO and SOMO in Figure 3.2b, we observed that only a small structural change was involved in the oxidation of 3MTPA to 3MTPA⁺ as shown in Figure 3.5e. Reorganization energy for the oxidation of 3MTPA was small as 118 meV, indicating that rapid structural relaxation is possible during redox reactions.⁵⁸⁻⁶⁰ The minimal geometric change during the redox reaction of 3MTPA is speculated to aid in the fast charge-transfer kinetics.

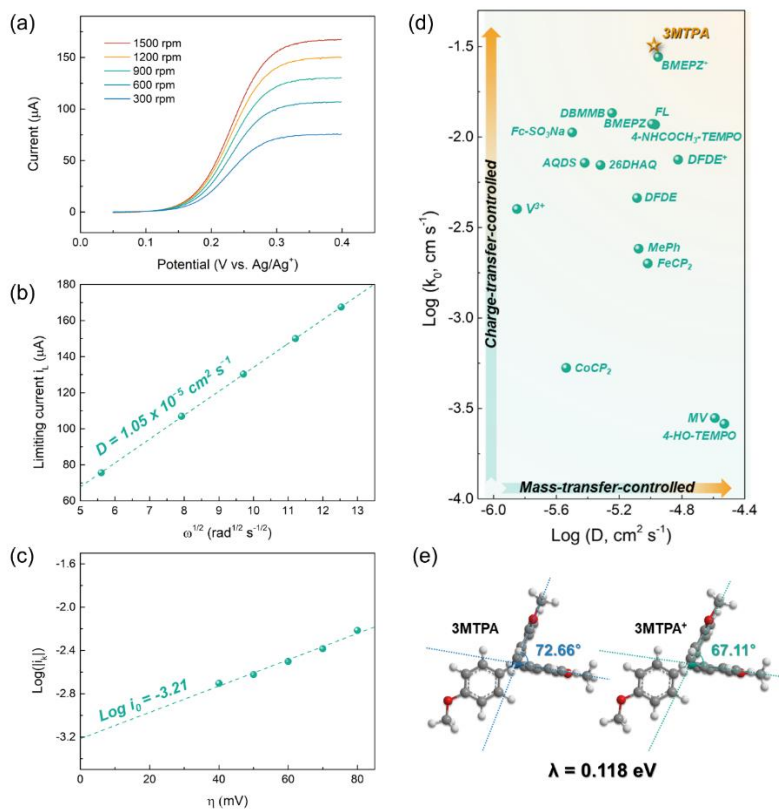


Figure 3.5. Kinetic study of 3MTPA. a) LSV curves of 3MTPA for various rotation rates. b) Linearly fitted Levich plots of limiting current (i_L) in terms of the square root of the rotation rate ($\omega^{-1/2}$). c) Linearly fitted plots of logarithm of kinetics-controlled current ($\log i_k$) as a function of overpotential (η). d) Comparison of kinetic parameters of reported redox-active materials in RFB system for the kinetic rate constant (k_0) and diffusion coefficient (D): this work (yellow stars) and reported RFBs (green circles). e) Molecular geometries of 3MTPA and 3MTPA⁺ with reorganization energy (λ).

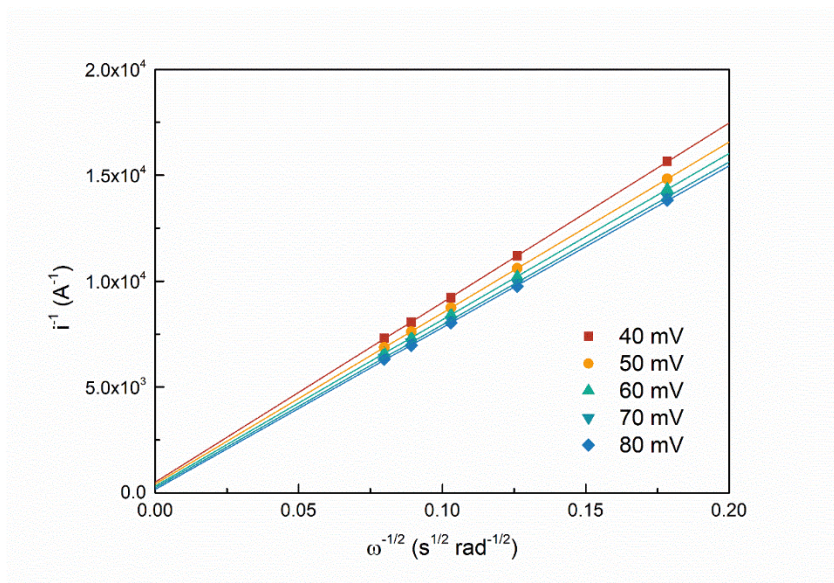


Figure 3.6. Linearly fitted Koutecký-Levich plots of 3MTPA with respect to the overpotentials.

3.3.3 Stability of 3MTPA in the charged state

The electrochemical stability of 3MTPA was carefully investigated by examining the capacity retention of a highly charged 3MTPA catholyte after prolonged storage at room temperature. Figure 3.7a schematically illustrates the experimental protocols; the 3MTPA catholyte was electrochemically charged to a full charge state and was divided into two symmetric cells containing the pristine 3MTPA as the counter electrode. Before constructing the cell, the catholyte in one of the two cells was stored at the charged state for a given time, and its deliverable capacity was compared with that of the catholyte without the delay, providing quantitative information about the extent of degradation occurring in the charged 3MTPA catholyte during the aging. We also conducted identical experiments for other ROMs including N-[2-(2-methoxyethoxy)ethyl]phenothiazine (MEEPT), 2-phenyl-4,4,5,5-tetramethylimidazoline-1-oxyl-3-oxide (PTIO), and 2,2,6,6-tetramethylpiperidinyloxy (TEMPO) for comparison. Figure 3.7b presents the discharge and charge profiles of the symmetric cells of the ROMs before (grey line) and after (blue line) aging, showing the time-dependent degradation of the charged species. Interestingly, the symmetric cell employing the 24-h-aged 3MTPA⁺ catholyte displayed almost identical capacity as that using the fresh 3MTPA⁺ catholyte, indicating that the 3MTPA catholyte is stable at a charged state. However, noticeable capacity losses of ~7% and ~4% were observed for PTIO and MEEPT, respectively, after 24 h of aging at room temperature. More notably, TEMPO, one of the representative catholytes in ORFBs, lost as much as 15% of its original capacity

by simply being stored at room temperature in the charged state. We additionally conducted a similar experiment on 9-fluorenone (FL), one of the most typical analytes in RFBs, which, to our surprise, exhibited even worse capacity degradation of ~69% after 24 h storage due to the poor radical stability of FL.

To further examine the chemical stability of charged ROMs over a longer period, a 1-week aging experiment (*e.g.*, 168 h storage) was performed for the charged 3MTPA and TEMPO catholytes, as shown in Figure 3.7c. The 3MTPA catholyte still retained full capacity without any loss even after 168 h of storage, whereas a significant capacity decay of ~38% was recorded for the TEMPO catholyte. The superior stability of the 3MTPA catholyte was further verified in the flow cell cycling, as depicted in Figure 3.7d. The symmetric flow cell employing 3MTPA exhibited robust cycle stability over 100 cycles without a noticeable loss of capacity. Even with 24 h of intermittent resting time after 50 cycles at a charged state, the capacity was well maintained, demonstrating the exceptional chemical stability of 3MTPA in the charged form benefiting from the synergistic stabilization effect as we intentionally designed.

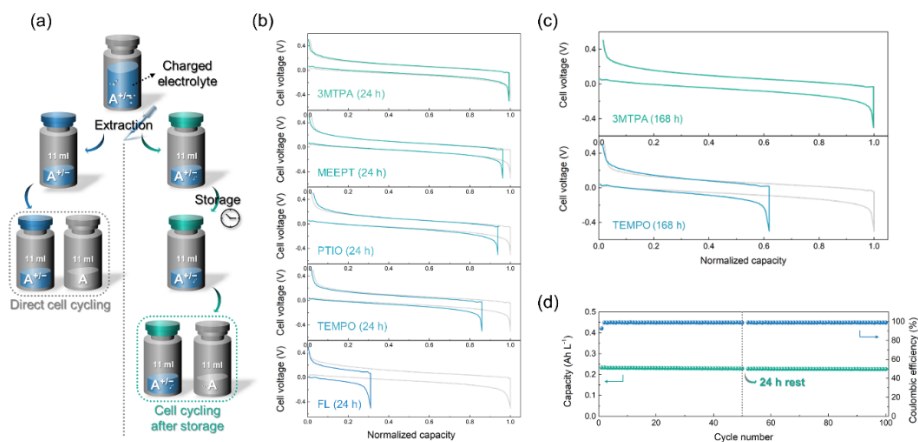


Figure 3.7. Investigation of chemical stability of 3MTPA in the charged state. a)

Illustration of experimental procedures for storage of the charged species.

Charge/discharge curves of symmetric cell using typical ROMs with/without b) 24

h or c) 168 h storage of charged species. d) Flow cell cycling of 10 mM 3MTPA at a

current density of 20 mA cm^{-2} with 24 h rest in the middle of 100 cycles.

3.3.4 Performance of 3MTPA under high temperature

Inspired by the remarkable chemical stability of 3MTPA, we further attempted to investigate the redox behavior of 3MTPA at high temperature. Flow cell cycling under high temperature conditions can be generally beneficial in terms of increased solubility of redox-active materials and fast kinetics;^{61,62} however, the cell cycling typically degrades more rapidly as the parasitic side reactions are simultaneously promoted at high temperature.^{18,62} We performed similar storage experiments with a storage time of 168 h at 50°C. Surprisingly, in contrast to the drastic capacity loss of TEMPO (less than 14% capacity retention after storage), 3MTPA successfully delivered capacity retention close to 100%, confirming the unprecedented chemical stability of 3MTPA even at elevated temperature (Figure 3.8a).

The stability of 3MTPA could allow high temperature flow cell operation, aiding in the achievement of high rate-capability and energy density with enhanced solubility. Figure 3.8b exemplifies that the flow cell of 3MTPA at 50°C could operate at the exceptionally high current density of 200 mA cm⁻², delivering cycling capacity of 5.61 Ah L⁻¹, which corresponds to ~70% of the theoretical capacity. This result is attributable to the intrinsically fast kinetics of 3MTPA and the stability at the high temperature condition, which are hardly achievable with other ROMs. Moreover, it should be noted that 3MTPA can exhibit significantly increased solubility of over 2.0 M in MeCN at 50°C (Figure 3.9), which is another merit for high-energy-density RFBs.

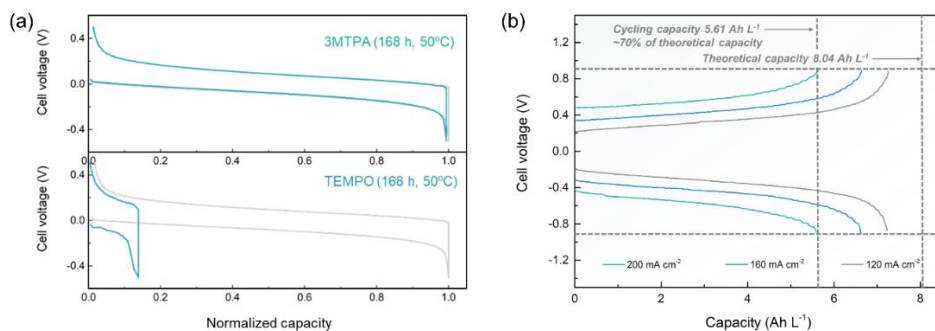


Figure 3.8. Redox behavior of 3MTPA under high temperature. a) Charge/discharge curves of symmetric cell using typical ROMs with/without 168 h storage of charged species at a high temperature of 50°C. b) Rate capability of 3MTPA at a high temperature of 50°C.



Figure 3.9. Completely soluble 2.0 M 3MTPA in MeCN at the high temperature of 50°C.

3.3.5 Long-term flow cell performance of 3MTPA

Finally, we investigated the long-term electrochemical performance/stability of the 3MTPA/3MTPA⁺ catholyte by cycling a custom flow cell, as illustrated in Figure 3.10a. Figure 3.10b presents a representative electrochemical profile of the symmetric cell employing 0.05 M 3MTPA in the supporting electrolyte of 0.5 M bis(trifluoromethane)sulfonimide lithium salt (LiTFSI) in MeCN at a current density of 60 mA cm⁻². The flow cell exhibited a well-defined plateau in the charge/discharge curve, indicating the reversible reaction of 3MTPA/3MTPA⁺. A discharge capacity of 1.14 Ah L⁻¹ was delivered, which corresponds to material utilization of ~85% considering the theoretical capacity of 1.34 Ah L⁻¹. We observed that the cell could be stably operated for extended cycle numbers, as shown in Figure 3.10c. The capacity loss was only 2.71% after 1400 cycles, which translates into an impressive capacity retention of 99.998% per cycle. Additionally, we tested the flow cell using a higher concentration system of 0.3 M 3MTPA at a current density of 100 mA cm⁻². The results revealed that a higher discharge capacity of 7.09 Ah L⁻¹ (close to the theoretical value of 8.04 Ah L⁻¹) could be obtained, as shown in Figure 3.10d. More importantly, the robust cell cycling was demonstrated over 300 cycles with a coulombic efficiency (CE) close to 100% (Figure 3.10e).

The fast mass- and charge-transfer kinetics of the 3MTPA could contribute to the high rate-capability of the RFB systems, as illustrated in Figure 3.10f. The flow cell of 3MTPA exhibited material utilization of ~95% at a current density of 40

mA cm⁻², and 82% of the theoretical capacity was delivered even at a high current density of 140 mA cm⁻², highlighting the superior rate capability considering the relatively low ionic conductivity of non-aqueous media. In Figure 3.10g, the flow cell performance of 3MTPA is compared with that of previously reported ORFBs in terms of cycle number, total capacity retention, and capacity retention per cycle. The capacity retention of most flow cells employing ROMs is typically below 99.98% per cycle, which can be attributed to the chemical instability of ROMs. Although the redox couple of bis(3-trimethylammonio)propyl viologen tetrachloride (BTAMP-Vi)/bis((3-trimethylammonio)propyl)-ferrocene dichloride (BTMAP-Fc) delivered a desirable capacity retention of 99.9989%, the stable cycling performance was only achieved for less than 500 cycles.⁶³ Long-term cycling performance was achieved using a phenazine-based anolyte (7,8-dihydroxyphenazine-2-sulfonic acid, or DHPS); however, a capacity decay of 12% after 1500 cycles (99.9921% per cycle) was recorded, which remains unsatisfactory for highly durable RFBs.⁶⁴ The plot visibly shows that 3MTPA ranks among the highest levels for all of the criteria, which is ascribed to the exceedingly high chemical stability and fast kinetics of the 3MTPA motif.

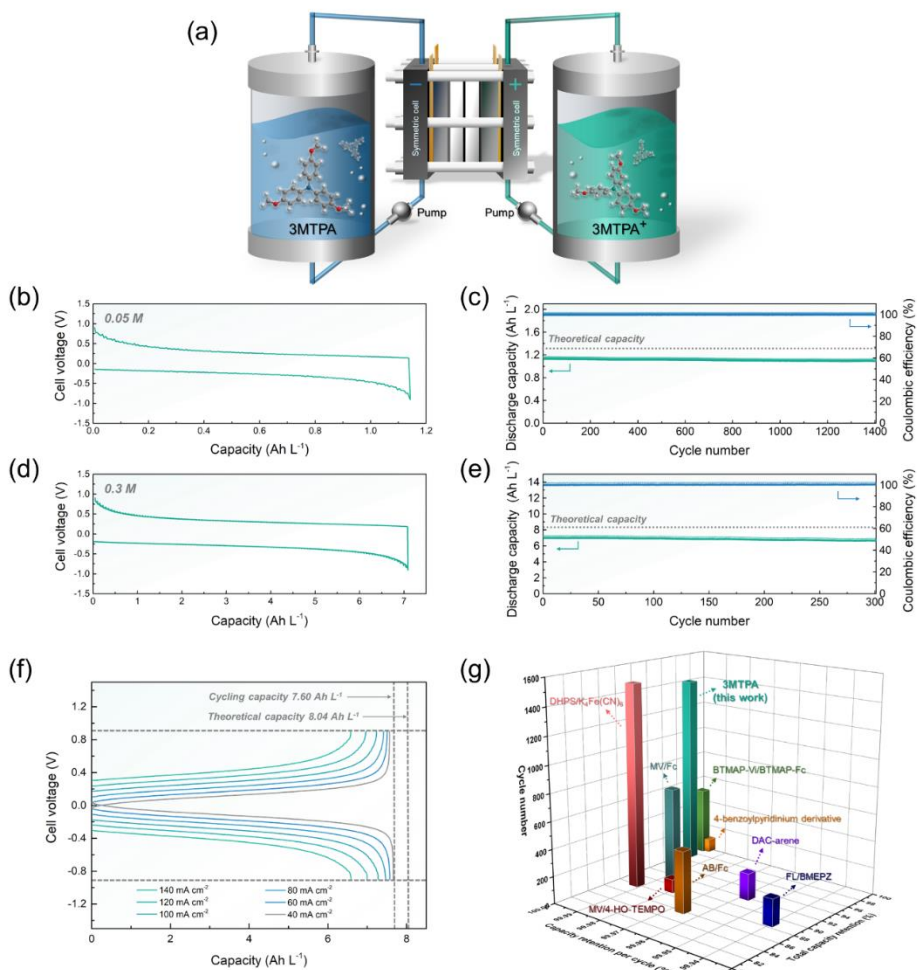


Figure 3.10. Electrochemical performance of flow cell using 3MTPA. a) Schematic illustration of symmetric flow battery exploiting 3MTPA. b) Representative charge/discharge curve for 0.05 M 3MTPA at current density of 60 mA cm⁻². c) Cycling efficiencies and capacities for 0.05 M 3MTPA with respect to cycle number. d) Typical electrochemical profile for 0.3 M 3MTPA at current density of 100 mA cm⁻². e) Cycling efficiencies and capacities for 0.3 M 3MTPA with respect to cycle number. f) Charge/discharge curves for 0.3 M 3MTPA at current

densities from 40 to 140 mA cm⁻². g) Flow cell cycling performance plot of typical redox-active materials in ORFBs.

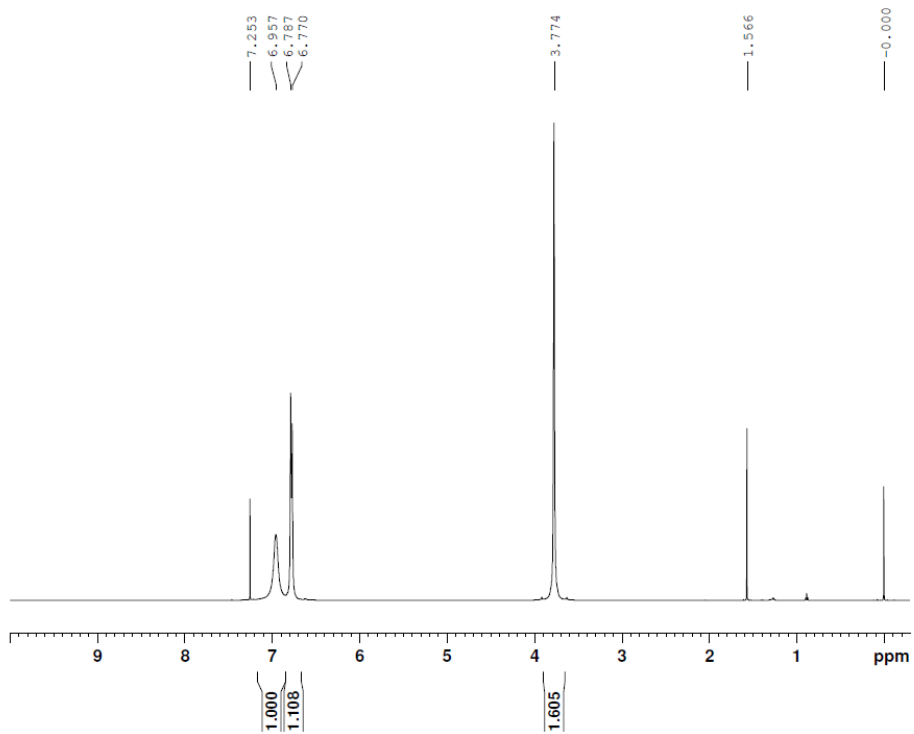


Figure 3.11. 500 MHz ^1H -NMR spectrum of 3MTPA in CDCl_3

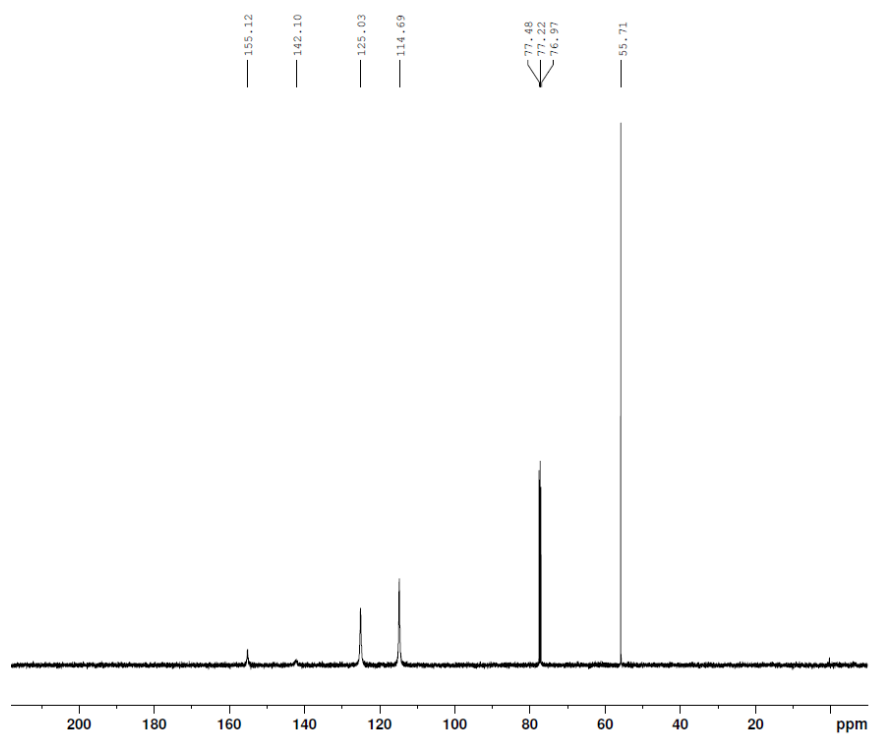


Figure 3.12. 125 MHz ^{13}C -NMR spectrum of 3MTPA in CDCl_3 .

3.4 Concluding remarks

We introduced a highly stable and durable TPA-based ROM, 3MTPA, as a promising catholyte material for high-performance RFBs. 3MTPA displays high chemical stability in the radical state owing to its synergistically designed molecular structure with large conjugation area spread over the entire molecular structure, end-capping, and the mesomeric electron donating effect of methoxy groups. Accordingly, it exhibited highly reversible redox reaction in a MeCN-based electrolyte even under harsh conditions. Interestingly, the stability of the 3MTPA in the charged state was outstanding, with negligible degradation of the cell observed even at elevated temperature after 168 h of aging, which could hardly be achieved by other ROMs reported to date. Benefiting from remarkable stability and kinetic properties, a flow cell using 3MTPA manifested exceptionally robust cycling performance along with superb rate capability, outperforming other previously reported ROMs in ORFBs. These findings on ROM with exceptional radical stability and superior kinetic properties are expected to expedite the development of highly durable and practically feasible ORFBs.

3.5 References

- 1 Dunn, B., Kamath, H. & Tarascon, J.-M. Electrical energy storage for the grid: a battery of choices. *Science* **334**, 928-935 (2011).
- 2 Zhao, H., Wu, Q., Hu, S., Xu, H. & Rasmussen, C. N. Review of energy storage system for wind power integration support. *Appl. Energy* **137**, 545-553 (2015).
- 3 Larcher, D. & Tarascon, J.-M. Towards greener and more sustainable batteries for electrical energy storage. *Nat. Chem.* **7**, 19-29 (2015).
- 4 Badwal, S. P., Giddey, S. S., Munnings, C., Bhatt, A. I. & Hollenkamp, A. F. Emerging electrochemical energy conversion and storage technologies. *Front. Chem.* **2**, 79 (2014).
- 5 Soloveichik, G. L. Flow batteries: current status and trends. *Chem. Rev.* **115**, 11533-11558 (2015).
- 6 Nguyen, T. & Savinell, R. F. Flow batteries. *Electrochem. Soc. Interface* **19**, 54 (2010).
- 7 Noack, J., Roznyatovskaya, N., Herr, T. & Fischer, P. The chemistry of redox-flow batteries. *Angew. Chem., Int. Ed.* **54**, 9776-9809 (2015).
- 8 Perry, M. L. & Weber, A. Z. Advanced redox-flow batteries: a perspective. *J. Electrochem. Soc.* **163**, A5064 (2015).
- 9 Park, M., Ryu, J., Wang, W. & Cho, J. Material design and engineering of next-generation flow-battery technologies. *Nature Reviews Materials* **2**, 1-18 (2016).

- 10 Winsberg, J., Hagemann, T., Janoschka, T., Hager, M. D. & Schubert, U. S. Redox-flow batteries: from metals to organic redox-active materials. *Angew. Chem., Int. Ed.* **56**, 686-711 (2017).
- 11 Lee, S. *et al.* Recent progress in organic electrodes for Li and Na rechargeable batteries. *Adv. Mater.* **30**, 1704682 (2018).
- 12 Ding, Y., Zhang, C., Zhang, L., Zhou, Y. & Yu, G. Molecular engineering of organic electroactive materials for redox flow batteries. *Chem. Soc. Rev.* **47**, 69-103 (2018).
- 13 Leung, P. *et al.* Recent developments in organic redox flow batteries: a critical review. *J. Power Sources* **360**, 243-283 (2017).
- 14 Zhang, C. *et al.* Progress and prospects of next-generation redox flow batteries. *Energy Storage Mater.* **15**, 324-350 (2018).
- 15 Wei, X. *et al.* Radical compatibility with nonaqueous electrolytes and its impact on an all-organic redox flow battery. *Angew. Chem., Int. Ed.* **54**, 8684-8687 (2015).
- 16 Armstrong, C. G. & Toghiani, K. E. Stability of molecular radicals in organic non-aqueous redox flow batteries: A mini review. *Electrochem. Commun.* **91**, 19-24 (2018).
- 17 Hicks, R. G. What's new in stable radical chemistry? *Org. Biomol. Chem.* **5**, 1321-1338 (2007).
- 18 Sevov, C. S. *et al.* Physical organic approach to persistent, cyclable, low-potential electrolytes for flow battery applications. *J. Am. Chem. Soc.* **139**,

- 2924-2927 (2017).
- 19 Fan, H. *et al.* Radical Charge Population and Energy: Critical Role in Redox Potential and Cycling Life of Piperidine Nitroxyl Radical Cathodes in Aqueous Zinc Hybrid Flow Batteries. *ACS Appl. Mater. Interfaces* **12**, 43568-43575 (2020).
- 20 Huang, J. *et al.* Liquid catholyte molecules for nonaqueous redox flow batteries. *Adv. Energy Mater.* **5**, 1401782 (2015).
- 21 Kwon, G. *et al.* Bio-inspired Molecular Redesign of a Multi-redox Catholyte for High-Energy Non-aqueous Organic Redox Flow Batteries. *Chem* **5**, 2642-2656 (2019).
- 22 Back, J. *et al.* Tunable Redox-Active Triazenyl–Carbene Platforms: A New Class of Anolytes for Non-Aqueous Organic Redox Flow Batteries. *ACS Appl. Mater. Interfaces* **12**, 37338-37345 (2020).
- 23 Luo, J., Hu, B., Debruler, C. & Liu, T. L. A π -conjugation extended viologen as a two-electron storage anolyte for total organic aqueous redox flow batteries. *Angew. Chem., Int. Ed.* **57**, 231-235 (2018).
- 24 Blanchard, P., Malacrida, C., Cabanetos, C., Roncali, J. & Ludwigs, S. Triphenylamine and some of its derivatives as versatile building blocks for organic electronic applications. *Polym. Int.* **68**, 589-606 (2019).
- 25 Munshi, M. U., Berden, G., Martens, J. & Oomens, J. Gas-phase vibrational spectroscopy of triphenylamine: the effect of charge on structure and spectra. *Phys. Chem. Chem. Phys.* **19**, 19881-19889 (2017).

- 26 Nelson, R. R. & Adams, R. N. Anodic oxidation pathways of substituted triphenylamines. II. Quantitative studies of benzidine formation. *J. Am. Chem. Soc.* **90**, 3925-3930 (1968).
- 27 Yurchenko, O. *et al.* Electrochemically induced reversible and irreversible coupling of triarylamine. *J. Phys. Chem. B* **116**, 30-39 (2012).
- 28 Wu, J.-T., Hsiang, T.-L. & Liou, G.-S. Synthesis and optical properties of redox-active triphenylamine-based derivatives with methoxy protecting groups. *J. Mater. Chem. C* **6**, 13345-13351 (2018).
- 29 Wang, J., Liu, K., Ma, L. & Zhan, X. Triarylamine: versatile platform for organic, dye-sensitized, and perovskite solar cells. *Chem. Rev.* **116**, 14675-14725 (2016).
- 30 Yen, H.-J. & Liou, G.-S. Recent advances in triphenylamine-based electrochromic derivatives and polymers. *Polym. Chem.* **9**, 3001-3018 (2018).
- 31 Bellmann, E. *et al.* New triarylamine-containing polymers as hole transport materials in organic light-emitting diodes: Effect of polymer structure and cross-linking on device characteristics. *Chem. Mater.* **10**, 1668-1676 (1998).
- 32 Cheng, Y.-J., Liao, M.-H., Shih, H.-M., Shih, P.-I. & Hsu, C.-S. Exciplex electroluminescence induced by cross-linked hole-transporting materials for white light polymer light-emitting diodes. *Macromolecules* **44**, 5968-5976 (2011).
- 33 Swayamprabha, S. S. *et al.* Hole-transporting materials for organic light-

- emitting diodes: an overview. *J. Mater. Chem. C* **7**, 7144-7158 (2019).
- 34 Meira, R. *et al.* Synthesis and optical properties of a new triphenylamine-p-phenylenevinylene-small molecule with applications in high open-circuit voltage organic solar cells. *New J. Chem.* **39**, 7389-7396 (2015).
- 35 Roncali, J., Leriche, P. & Blanchard, P. Molecular materials for organic photovoltaics: small is beautiful. *Adv. Mater.* **26**, 3821-3838 (2014).
- 36 Niu, H. *et al.* Novel soluble polyazomethines with pendant carbazole and triphenylamine derivatives: preparation, characterization, and optical, electrochemical and electrochromic properties. *Polym. Chem.* **2**, 2804-2817 (2011).
- 37 Frisch, M. J. *et al.* Gaussian 09, Revision A. 1, 27. *Gaussian Inc., Wallingford CT*, 34 (2009).
- 38 Lee, C., Yang, W. & Parr, R. G. Development of the Colle-Salvetti correlation-energy formula into a functional of the electron density. *Phys. Rev. B* **37**, 785-789 (1988).
- 39 Becke, A. D. Density-functional thermochemistry. III. The role of exact exchange. *J. Chem. Phys.* **98**, 5648-5652 (1993).
- 40 Stephens, P. J., Devlin, F. J., Chabalowski, C. F. & Frisch, M. J. Ab Initio Calculation of Vibrational Absorption and Circular Dichroism Spectra Using Density Functional Force Fields. *J. Phys. Chem. A* **98**, 11623-11627 (1994).
- 41 Schäfer, A., Horn, H. & Ahlrichs, R. Fully optimized contracted Gaussian

- basis sets for atoms Li to Kr. *J. Chem. Phys.* **97**, 2571-2577 (1992).
- 42 Schäfer, A., Huber, C. & Ahlrichs, R. Fully optimized contracted Gaussian basis sets of triple zeta valence quality for atoms Li to Kr. *J. Chem. Phys.* **100**, 5829-5835 (1994).
- 43 Miertuš, S., Scrocco, E. & Tomasi, J. Electrostatic interaction of a solute with a continuum. A direct utilization of AB initio molecular potentials for the prevision of solvent effects. *Chemical Physics* **55**, 117-129 (1981).
- 44 Scalmani, G. & Frisch, M. J. Continuous surface charge polarizable continuum models of solvation. I. General formalism. *J. Chem. Phys.* **132**, 114110 (2010).
- 45 Macrae, C. F. *et al.* Mercury CSD 2.0—new features for the visualization and investigation of crystal structures. *J. Appl. Crystallograph.* **41**, 466-470 (2008).
- 46 Gryn'ova, G. & Coote, M. L. Origin and scope of long-range stabilizing interactions and associated SOMO–HOMO conversion in distonic radical anions. *J. Am. Chem. Soc.* **135**, 15392-15403 (2013).
- 47 Faulkner, L. R. & Bard, A. J. *Electrochemical methods: fundamentals and applications*. (John Wiley and Sons, 2002).
- 48 Liu, T., Wei, X., Nie, Z., Sprenkle, V. & Wang, W. A total organic aqueous redox flow battery employing a low cost and sustainable methyl viologen anolyte and 4-HO-TEMPO catholyte. *Adv. Energy Mater.* **6**, 1501449 (2016).

- 49 Ding, Y., Zhao, Y., Li, Y., Goodenough, J. B. & Yu, G. A high-performance all-metallocene-based, non-aqueous redox flow battery. *Energy Environ. Sci.* **10**, 491-497 (2017).
- 50 Wei, X. *et al.* A high-current, stable nonaqueous organic redox flow battery. *ACS Energy Lett.* **1**, 705-711 (2016).
- 51 Chen, H. *et al.* Multicore Ferrocene Derivative as a Highly Soluble Cathode Material for Nonaqueous Redox Flow Batteries. *ACS Appl. Energy Mater.* (2020).
- 52 Fan, H. *et al.* Radical Charge Population and Energy: Critical Role in Redox Potential and Cycling Life of Piperidine Nitroxyl Radical Cathodes in Aqueous Zinc Hybrid Flow Batteries. *ACS Appl. Mater. Interfaces* **12**, 43568-43575 (2020).
- 53 Kwon, G. *et al.* Multi-redox molecule for high-energy redox flow batteries. *Joule* **2**, 1771-1782 (2018).
- 54 Huskinson, B. *et al.* A metal-free organic–inorganic aqueous flow battery. *Nature* **505**, 195-198 (2014).
- 55 Weber, A. Z. *et al.* Redox flow batteries: a review. *J. Appl. Electrochem.* **41**, 1137 (2011).
- 56 Yu, J. *et al.* A robust anionic sulfonated ferrocene derivative for pH-neutral aqueous flow battery. *Energy Storage Mater.* **29**, 216-222 (2020).
- 57 Lin, K. *et al.* Alkaline quinone flow battery. *Science* **349**, 1529-1532 (2015).
- 58 Lee, K. *et al.* Phenoxazine as a high-voltage p-type redox center for organic

- battery cathode materials: small structural reorganization for faster charging and narrow operating voltage. *Energy Environ. Sci.* **13**, 4142-4156 (2020).
- 59 Lv, Y. *et al.* Structure reorganization-controlled electron transfer of bipyridine derivatives as organic redox couples. *J. Mater. Chem. A* **7**, 27016-27022 (2019).
- 60 Pearson, R. M., Lim, C.-H., McCarthy, B. G., Musgrave, C. B. & Miyake, G. M. Organocatalyzed atom transfer radical polymerization using N-aryl phenoxazines as photoredox catalysts. *J. Am. Chem. Soc.* **138**, 11399-11407 (2016).
- 61 Xi, J. *et al.* Broad temperature adaptability of vanadium redox flow battery—Part 2: Cell research. *Electrochim. Acta* **191**, 695-704 (2016).
- 62 Zhang, C., Zhao, T. S., Xu, Q., An, L. & Zhao, G. Effects of operating temperature on the performance of vanadium redox flow batteries. *Appl. Energy* **155**, 349-353 (2015).
- 63 Beh, E. S. *et al.* A neutral pH aqueous organic–organometallic redox flow battery with extremely high capacity retention. *ACS Energy Lett.* **2**, 639-644 (2017).
- 64 Hollas, A. *et al.* A biomimetic high-capacity phenazine-based anolyte for aqueous organic redox flow batteries. *Nat. Energy* **3**, 508-514 (2018).

Chapter 4. In-depth understanding of redox flow battery through *in-operando* visualization technique

4.1 Research background

Unprecedented demands for the renewable energy resources become one of the acutest challenges to date, but their intermittent supply is clearly limiting the efficient utilization of these resources¹⁻³. The large-scale energy storage systems (ESSs) thus should be paired to mitigate the intermittency for unstoppable delivery of their full promise. Among state-of-the-art ESSs, redox flow batteries (RFBs), using energy-bearing liquid electrolytes, have drawn significant attentions because of their unique scalable architecture with the design flexibility of decoupling power and energy⁴⁻⁶. In the light of these advantages, extensive researches have been conducted for the commercialization of large-scale RFBs, such as vanadium- and zinc/bromine-based RFBs⁷. Furthermore, new RFB systems based on various redox couples have been introduced in recent years. In particular, the most recent researches have focused on exploiting redox-active organic materials (ROMs) as catholyte/anolyte materials due to their exclusive features of cost-effectiveness, environmental friendliness, and chemical tunability^{8,9}. A number of ROMs, *e.g.*, quinone- and tempo-based derivatives, were successfully demonstrated with extraordinary electrochemical performances, which could rival with the commercial

vanadium- or zinc/bromine-based systems.

Despite of the rapid growth of RFB technologies, the general tools to probe the reaction mechanisms of these various active materials in flow-dynamic electrochemical cell have not been well-established. Considering that the RFB is a dynamic system that the electrochemistry and the fluid dynamics concurrently govern the performance, advanced analytic platforms that can probe the mass- and charge- transport are indispensable for elucidating the complex electrokinetic phenomena of the redox couples. In conventional lithium battery fields, real-time analytic techniques have been widely employed, which could aid in elucidating the hidden intermediate electrochemical reactions, such as the phase transformation/kinetics of electrode materials by high-speed synchrotron X-ray diffractions, thermal runaway mechanism of lithium-ion batteries by X-ray tomography, or observing lithium dendrite growth process in lithium-metal electrode by cryo-TEM analysis, and, *etc*¹⁰⁻¹⁷. While these *in-situ* techniques were valuable unraveling the solid-state reactions occurring in lithium batteries, the dynamic flow of active liquid-state catholyte/anolyte in RFBs require new sets of characterization tools. It is because the electrochemical performance of RFB is dependent on the balancing of the extrinsic flow rate of the active liquids by mechanical pump and the intrinsic charge-transfer kinetics of the active molecules on the electrode. The interplay of these two, which are not commonly considered in conventional lithium batteries, should be considered in devising the strategy to enhance the electrochemical performance, but, however, it has been largely overlooked to date.

Recent attempts to employ *in-situ* characterizations have proven the importance of the real-time observation of the RFB reactions. Zhao *et al.* recently succeeded in probing the redox chemistry of quinone-based ROMs in RFBs by the *in-situ* nuclear magnetic resonance (NMR) metrology, which could unveil the electrolyte decomposition mechanism and quantify the rate of electron transfer¹⁸. Moreover, the crossover of some active materials such as vanadium- and quinone-based materials could be directly witnessed by the *in-situ* optical spectrophotometry and electron paramagnetic resonance (EPR), respectively^{19,20}.

Herein, we introduce *in-operando* visualization of RFB system using a novel microfluidic platform that can concomitantly probe the mass- and charge-transfer of ROMs. The platform made of transparent materials enables a real-time observation inside the cell so that the highly coupled electrochemistry and fluid dynamics could be successfully analyzed. In addition, a laminar interface in microfluidic channel allows a battery operation without a membrane, thus the fundamental flow-dynamic study can be systematically performed^{21,22}. In our demonstration, we chose to investigate the multi-redox organic molecule (5,10-bis(2-methoxyethyl)-5,10-dihydrophenazine (BMEPZ)) possessing two stages of color change depending on charge states, which is highly advantageous for optical *in-operando* visualization. In-depth experimental and numerical kinetic studies successfully identify the presence of the rate-limiting region and propose the electrode design that can address the optimization of the mass- and charge-transfer kinetics of ROMs. This *in-operando* visualization tool employing membrane-free

microfluidic cell is expected to aid in elucidating various electrokinetic reactions in dynamic flow-based electrochemical systems, which can be extended to other similar RFBs.

4.2 Experimental method

4.2.1 Fabrication of cell and preparation of materials

The MFRFB system requires several microscale fabrications for inducing laminar flow during electrochemical reaction²³⁻³². As shown in Figure 4.1a, metal deposition process (Au lift-off process) was conducted on the surface of 4' glass wafer for electrodes patterning. The thickness of Au/Ti electrodes was 1100 Å (Au: 1000 Å and Ti: 100 Å). Ti was priorly deposited as adhesion layer between glass and gold electrode. The glass wafer was diced into a square of 20 mm × 20 mm and it bonded onto a slide glass (2.5 cm × 7.5 cm, Daihan scientific, Korea) using a scotch super glue (3M, USA). Then precut porous carbon felts (200 ± 20 μm thickness, XF30A; TOYOBO, Korea) were overlaid on to the electrodes.

A PDMS block (Slygard 184 silicone elastomer kit, Dow Corning, USA) as a microfluidic RFB cell was molded by predefined silicon master. The master had a microfluidic channel pattern of two bifurcated inlet and outlet. Briefly, PDMS solution was mixed with a curing agent at the ratio of 10:1 and degassed for an hour in the vacuum chamber. The degassed solution was poured into the master and was cured in the oven for four hours at 75 °C. Then, the PDMS block was detached from the master and triangular pieces were cut from the block for connecting external current source. The two inlets and two outlets were punched by biopsy punch (BF-15F, Kai Medical, Japan) to create the holes of 1.5 mm diameter.

Electrodes deposited glass and PDMS block was irreversibly bonded using oxygen plasma (CUTE-MP, Femto Science, Korea) treatment. The process of

fabrications and image of assembled device was shown in Figure 4.1a and 1b.

Acetonitrile (MeCN) and FL were purchased from Sigma-Aldrich and used as received. Bis(trifluoromethane)sulfonimide lithium salt (LiTFSI) was purchased from TCI Chemicals (JAPAN) and dried under vacuum at 180°C for 24 h to remove moisture. BMEPZ was synthesized following previously reported synthetic route²².

4.2.2 Electrochemical measurements

For the electrochemical measurements, the electrolytes were prepared and evaluated in an Ar-filled glove box under an inert atmosphere (<0.5 ppm O₂, H₂O) except the one flow charging experiment. Pipette tips as electrolyte reservoirs were inserted into each inlet and outlet of the PDMS block. Ag wires were glued onto the electrode using conductive epoxy (Silver Conductive epoxy 8330S-21G, MG Chemicals, Canada).

For the one flow charging experiment, molar concentration of electrolyte for *in-operando* visualization of multi-redox experiment was 1.0 x 10⁻³ M and 0.05, 0.075 and 0.1 mA of constant current was applied to the microfluidic RFB by a source measure unit (Keithley 238, USA) via Ag electrodes connected to the Au electrodes. The electrolytes were infused by the syringe pump (Harvard Apparatus PHD 2000 Syringe Pump, Hayward, CA, USA) from inlets to outlets. 1 Minute as a resting time was given for fully filling the microchannel and build-up for laminar interface of electrolytes. After resting time, constant current was applied for 120s. For the measurement of voltage and capacity characteristic, customized LabVIEW program was used. Images and video files of *in-operando* visualization were

captured by a stereomicroscope System (OLYMPUS, SZ61, Japan) and CellSens program.

For the circulation experiment, peristaltic pump (LabV6, SHENCHEN, China) and constant-current mode using a battery test system (WBCS 3000; WonA Tech, Korea) were used. Symmetric redox couple of BMEPZ and BMEPZ⁺ (each 1.0 mM) in the supporting electrolyte of 0.5 M LiTFSI in MeCN (0.5 ml) was used with the flow rate of 1 mL min⁻¹. The volume of electrolytes was 0.7 mL.

CV curves of BMEPZ and FL (10 mM each) were captured using the supporting electrolytes of 0.5 M LiTFSI in MeCN. A three-electrode system (Pt counter electrode, Ag/AgNO₃ reference electrode, and glassy carbon working electrode) was employed with the scan rate of 100 mV s⁻¹. For the UV-vis spectroscopy analysis to verify that diffusive mixing at the laminar interface of electrolytes, absorption spectra of the inlet and outlet catholytes (diluted in MeCN, 5% v/v) were obtained using a UV-vis spectrometer (Agilent Technologies, Cary 5000) with an optical glass cuvette (Quartzl Hellma).

4.2.3 Numerical model details

In the actual microfluidic flow battery of this work, used electrolytes were 10 x 10⁻³ M BMEPZ as catholyte, 20 x 10⁻³ M FL as anolyte and 0.5 M LiTFSI as supporting electrolyte. The supporting electrolyte was an inert salt with a concentration much greater than other electrolyte components. Due to the supporting electrolyte, the transport phenomena of catholyte, anolyte and other related derivatives can be described by the convection–diffusion equation^{33,34}. In the battery

systems, there were five kinds of electrolytic species which were involved in electrochemical reactions; FL, FL⁻, BMEPZ, BMEPZ⁺ and BMEPZ²⁺. Thus, we solved the convection-diffusion equations for each electrolytic species, the continuity equation and the Stokes equations for flow field (\mathbf{u}) and pressure (p) inside numerical domain. For a convenience, each electrolyte concentration was denoted as c_{FL} for FL, c_{FL1} for FL⁻, c_{BM} for BMEPZ, c_{BM1} for BMEPZ⁺ and c_{BM2} for BMEPZ²⁺, respectively. Detailed formulations were given as below.

The convection-diffusion equation for each species was given by

$$\frac{\partial c_i}{\partial t} = -D_i \nabla c_i + c_i \mathbf{u} \quad (1)$$

where c_i is the concentration of i -th species, t is the time, D_i is the diffusivity of i -th species, \mathbf{u} is the flow field. Note that the electrochemical reactions were only on electrode surface so that any reaction terms were omitted in above equation. Instead, the electrochemical reactions were described by the appropriate boundary conditions. The flow field and pressure field were described by the continuity equation and the Stokes equations.

$$\nabla \cdot \mathbf{u} = 0 \quad (2)$$

$$\rho \frac{\partial \mathbf{u}}{\partial t} = -\nabla p + \mu \nabla^2 \mathbf{u} \quad (3)$$

where ρ is the fluid viscosity, p is the pressure and μ is the fluid viscosity.

The boundary conditions on inlet 1 were

$$c_{BM} = 1.0 \times 10^{-3} M \quad (4)$$

$$c_i = 0 \text{ for } i \neq \text{BM} \quad (5)$$

$$\int_0^H u_x dy = UH \quad (6)$$

where H is the half-height of numerical domain, u_x is the x -directional flow field and U is the specific value of averaged flow velocity. Equations (4) and (5) mean only BMEPZ was introduced through inlet 1. Equation (6) is constraint for averaged value. Collaborating with no-slip condition at inert wall and electrode surface, the flow field becomes the Hagen-Poiseuille flow. Similarly, on inlet 2,

$$c_{FL} = 20 \times 10^{-3} M \quad (7)$$

$$c_i = 0 \text{ for } i \neq \text{FL} \quad (8)$$

$$\int_{-H}^0 u_x dy = UH \quad (9)$$

On inert wall, no penetration condition for each electrolyte species and no-slip condition for fluid flow were imposed.

$$\mathbf{n} \cdot \nabla c_i = 0 \quad (10)$$

$$\mathbf{u} = 0 \quad (11)$$

where \mathbf{n} is the outward normal vector. On electrode 1, there were BMEPZ-related electrochemical reactions. Such reactions caused effective electrolyte flux through the boundary. Dealing with the Butler-Volmer equation, the boundary conditions were

$$-\mathbf{n} \cdot \nabla c_{BM} = -\frac{i_{BM}}{F} \left[\frac{c_{BM}}{c_{ref}} \exp\left(\frac{F\eta_{BM}}{2RT}\right) - \frac{c_{BM1}}{c_{ref}} \exp\left(-\frac{F\eta_{BM}}{2RT}\right) \right] \quad (12)$$

$$-\mathbf{n} \cdot \nabla c_{BM1} = -\mathbf{n} \cdot \nabla c_{BM} + \mathbf{n} \cdot \nabla c_{BM2} \quad (13)$$

$$-\mathbf{n} \cdot \nabla c_{BM2} = -\frac{i_{BM1}}{F} \left[\frac{c_{BM1}}{c_{ref}} \exp\left(\frac{F\eta_{BM1}}{2RT}\right) - \frac{c_{BM2}}{c_{ref}} \exp\left(-\frac{F\eta_{BM1}}{2RT}\right) \right] \quad (14)$$

$$\mathbf{n} \cdot \nabla c_{FL} = \mathbf{n} \cdot \nabla c_{FL1} = 0 \quad (15)$$

$$\mathbf{u} = 0 \quad (16)$$

where i_{BM} and i_{BM1} are the exchange current density for related electrochemical reactions of which values are 28.11 A m^{-2} and 5.286 A m^{-2} , F is the Faraday constant, c_{ref} is the experimental concentration of the exchange current measurement (1 mM), η_{BM} and η_{BM1} are the overpotential for electrolytic species, R is the gas constant and T is the absolute temperature. The definitions of overpotential were

$$\eta_{BM1} = V_{BM} - E_{BM1}^{eq} \quad \eta_{BM} = V_{BM} - E_{BM}^{eq} \quad (17)$$

$$\eta_{BM1} = V_{BM} - E_{BM1}^{eq} \quad (18)$$

where V_{BM} is the electrical potential at electrode 1, E_{BM}^{eq} and E_{BM1}^{eq} are the equilibrium potential of which values are -0.18 V and 0.59 V . Since the actual experiments were done in constant current mode, following additional constraint on electrode 1 should solved simultaneously.

$$\int_0^L \mathbf{n} \cdot \nabla c_{BM1} + 2\mathbf{n} \cdot \nabla c_{BM2} dx = -\frac{i_{app}L}{F} \quad (19)$$

where i_{app} is the applied current density as a constant. Similar to electrode 1, the boundary conditions on electrode 2 were given by

$$-\mathbf{n} \cdot \nabla c_{FL} = -\frac{i_{FL}}{F} \left[\frac{c_{FL}}{c_{ref}} \exp\left(\frac{F\eta_{FL}}{2RT}\right) - \frac{c_{FL1}}{c_{ref}} \exp\left(-\frac{F\eta_{FL}}{2RT}\right) \right] \quad (20)$$

$$-\mathbf{n} \cdot \nabla c_{BM1} = \mathbf{n} \cdot \nabla c_{FL} \quad (21)$$

$$\eta_{FL} = V_{FL} - E_{FL}^{eq} \quad (22)$$

$$\int_0^L \mathbf{n} \cdot \nabla c_{BM1} dx = -\frac{i_{app} L}{F} \quad (23)$$

$$\mathbf{u} = 0 \quad (24)$$

where i_{FL} is the exchange current density of which value is 11.19 A m^{-2} , V_{FL} is the electrical potential at electrode 2, E_{FL}^{eq} is the equilibrium potential of which value is -1.33 V ^{35,36}.

4.3 Results and discussions

4.3.1 Concept of microfluidic membrane-free RFB (MFRFB)

To investigate the intrinsic mass- and charge-transfer reactions occurring in RFB, a microfluidic platform was employed, which can implement microfluidic manipulation such as controlling flow rate and tracking of the charge states of catholyte. The fabrication process and the assembled device are schematically illustrated in Figure 4.1a and 4.1b, respectively. In this study, a catholyte through inlet 1 to outlet 1 and an anolyte through inlet 2 to outlet 2 were pumped at the same flow rate (Figure 4.1b). We intentionally designed the microscale dimension of the fluidic system so that two electrolyte streams form a stable fluidic boundary called laminar interface as shown in Figure 4.1c, which is the region of interest in this work. The laminar interface allows the clear separation of the anolyte and catholyte without the need for the membrane materials for the RFB operation. As per the application of external current, the electrochemical reaction begins at both electrodes with the ion-exchange for charge balance through the laminar interface instead of membrane. Since the BMEPZ redox couple has the colorimetry property, displaying color change depending on state-of-charge (SOC) states, the multi redox reaction of the catholyte can be readily detectable by microscopic observations.

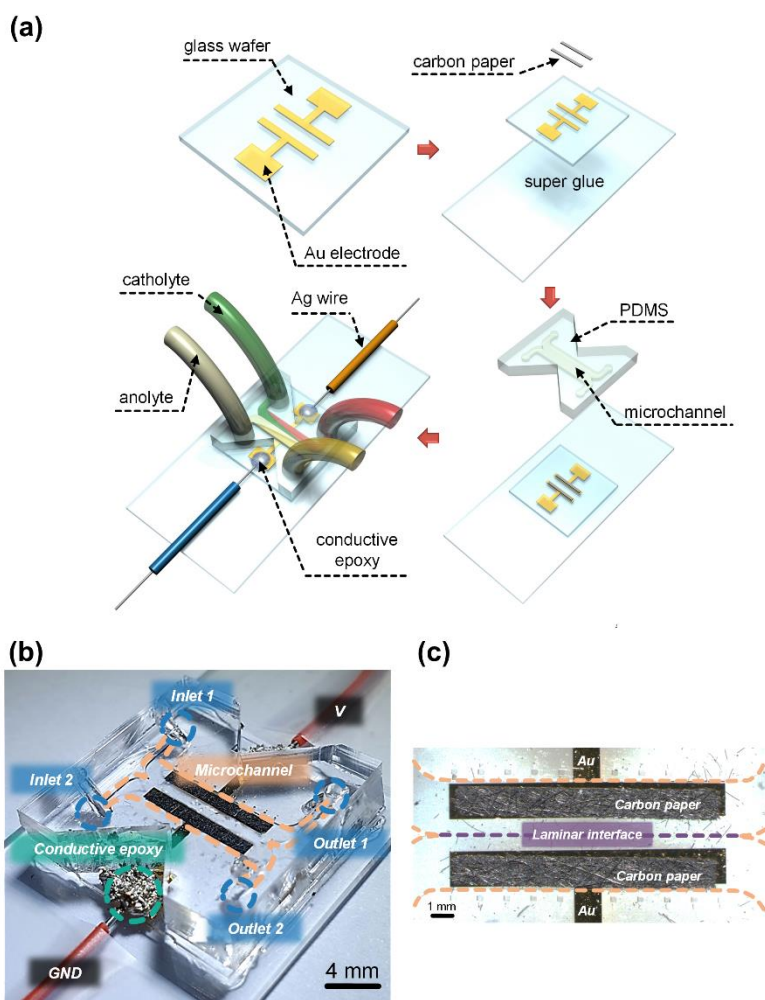


Figure 4.1. a) The microscale fabrication process of the MFRFB device. b) The photo of assembled MFRFB device connected to electrical source. c) The microscopic view of observation area for current study.

4.3.2 In-operando visualization of mass- and charge-transfer in MFRFB

Figure 4.2a shows the cyclic voltammetry of organic redox couple used in the current study. As previously reported, BMEPZ, which is a soluble multi-redox material for catholyte, undergoes two single-electron redox reactions on diazabutadiene motif (N-C=C-N) at the redox potentials of -0.18 V and 0.59 V vs. Ag/Ag⁺ and displays drastic color changes with respect to the charge states^{35,36}. The changes in color occur in two distinct stages, (i) from yellow to green during the first oxidation corresponding to BMEPZ⁺ and (ii) from green to red becoming BMEPZ²⁺. To demonstrate the full cell, 9-fluorenone (FL) was adopted as an active material for anolyte, which does not present apparent color regardless of SOC. FL generally exhibits a single redox reaction at the redox potential of -1.33 V vs. Ag/Ag⁺, enabling the two different full cell voltages of $\Delta E_1 = 1.15$ V and $\Delta E_2 = 1.92$ V for BMEPZ/FL redox couple in RFBs.

Our microfluidic device equipped with the circulation capability could independently control the key kinetic factors in the electrochemical reactions of RFBs, *i.e.*, the applied current density and the flow rate of catholyte/anolytes. During the circulation of the cell with various current densities and flow rates, we carefully tracked the color changes of active materials at the electrode through *in-operando* visualization technique. The systematic alternations of the kinetic parameters were supposed to reveal the migration behavior of the active materials and the electron-transfer rate after they reach the electrodes. Figure 4.2b-c depict the electrochemical

profiles and corresponding images of the microfluidic cell as a function of the current densities at a fixed flow rate of $10 \mu\text{L min}^{-1}$. It clearly illustrates that when the redox plateau appears at the cell voltage of 1.0 V with the current rate of 0.05 mA in Figure 4.2b, the catholyte turns to green color in Figure 4.2c, corresponding to the oxidation reaction of BMEPZ to BMEPZ^{+35} . As higher current rates are applied at the cell such as 0.075 mA and 0.1 mA, the plateau voltage gradually elevates close to the 2.0 V, skipping the characteristic voltage plateau of BMEPZ to BMEPZ^+ at 1.0 V. Moreover, the color of catholyte partially turns into red, indicating the generation of BMEPZ^{2+} . It is noteworthy that when the typical voltage plateau of the second redox (BMEPZ^{2+}) appears at 2.0 V, the signature of the BMEPZ^+ (green color) is still dominantly observable near the electrode even though the 1.0 V plateau is significantly shortened or absent. It implies that the electrochemical oxidation rates exceed the mass-transfer rate at the current rates $> 0.05 \text{ mA}$ (e.g., 0.075 or 0.1 mA), causing the partial over-potential and provoking the second electron-redox reactions. On the other hand, the low current of 0.05 mA was the suitable electron-transfer rate of the single redox reaction at the given mass-transfer rate. Furthermore, we distinctly verified that the apparent cell voltage elevation with the current increase is not simply the results of the over-potential but is accompanied with the second redox reaction of BMEPZ as evidenced by the red color observed by this *in-operando* visualization technique.

To further investigate the effect of mass-transfer, the flow rates of electrolytes were systematically altered to 10, 15, and $20 \mu\text{L min}^{-1}$ at a fixed current rate of 0.1 mA in Figure 4.2d-e. It manifests that at the high flow rate of $20 \mu\text{L min}^{-1}$

¹, the supply of fresh ROMs to the electrode is fast enough to satisfy the given electron-transfer rate (0.1mA), showing the characteristic plateau of the first redox reaction of BMEPZ. This is contrast to the case of Figure 4.2c with 0.1mA, where the second redox reaction was observed. Similarly, as the flow rate gradually decreases, the premature second redox reaction of BMEPZ could be clearly observable with the red color of electrolyte as shown in Figure 4.2e. It indicates that the relative lack of the mass-transfer to the electrode leads to the condition for the excessive electron-transfer. It was additionally noteworthy that the color change to red occurred mostly at the upper side of cathode, which is attributed to the formation of a depletion region^{37,38}. This will be further discussed in the section of numerical study in terms of diffusion and convection. It infers that the consideration of balanced mass- and charge-transfer rate is highly imperative to efficiently utilize the redox-active materials in the RFB cells. Moreover, it was also meaningful that *in-operando* visualization technique was able to provide direct clues to interpret the electrochemical reactions in RFBs.

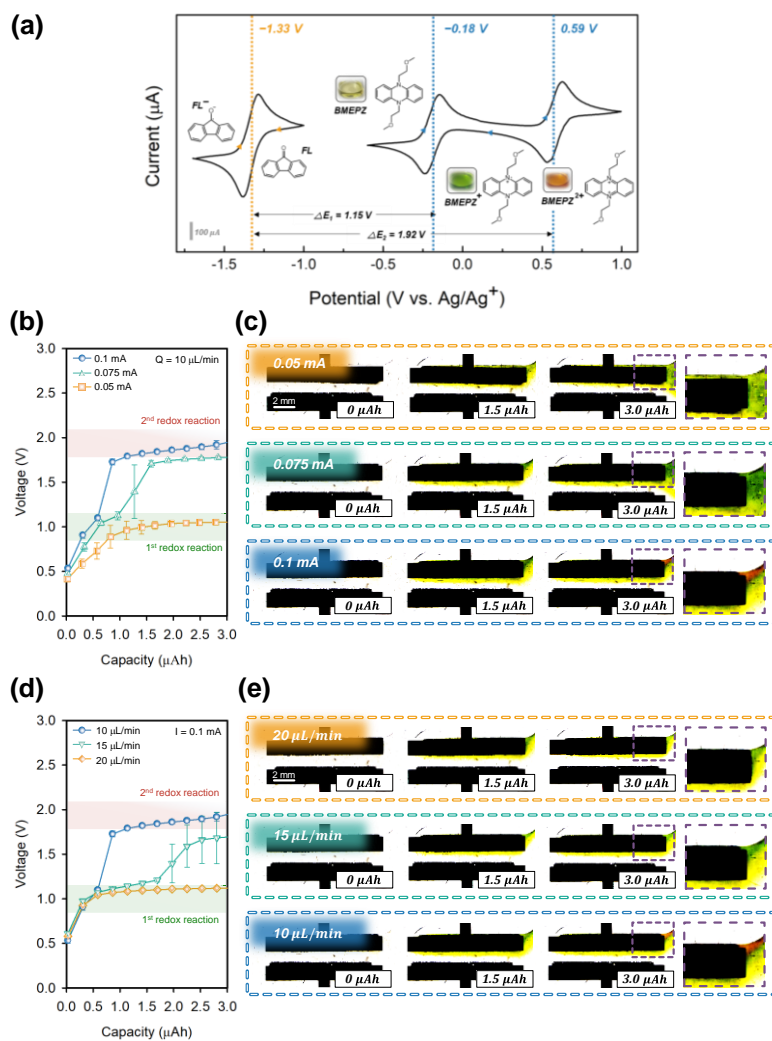


Figure 4.2. Kinetic study of 3MTPA. a) The cyclic voltammetry of multi-redox couple. b) Voltage and capacity profile of BMEPZ in terms of charge transfer. c) In-operando visualization of electrochemical reaction in terms of charge transfer. d) Voltage and capacity profile of BMEPZ in terms of mass transfer. e) In-operando visualization of electrochemical reaction in terms of mass transfer.

4.3.3 Electrokinetic analysis of MFRFB for mass- and charge-transfer

Inspired by the observed coupling of electrochemical reaction and fluid kinetics, we attempted to further understand the physicochemical hydrodynamics behind the battery operation, and conducted the numerical study of the transport phenomena to support our *in-operando* visualization. Figure 4.3a schematically illustrates the numerical domain inside the MFRFB cell, where there are two important regions that affect the electrochemical performance, diffusion region and depletion region³⁷⁻⁴⁰. The diffusion region is formed around the laminar interface due to the diffusive mixing between anolyte and catholyte. On the other hand, the depletion region is formed near electrode surface because of the consumption of reactants during the electrochemical reaction. These two regions expand in y -direction by diffusion and propagate in x -direction by convection as the electrolytes flow toward the outlets, while the diffusion could be either accelerated or decelerated by electrochemical reactions. It is widely known that with the larger depletion region, the reaction kinetics is generally limited, and the expanded diffusion region also leads to significant crossover of active materials, resulting in the deterioration of battery performance^{37,38}.

We conducted two-dimensional (2-D) numerical simulation to elucidate the hydrodynamics during the electrochemical reaction by probing changes in the concentration profiles of active materials. The governing equations for momentum and mass-transfer were Stokes equations and diffusion-convection equation,

respectively, and the reaction kinetics was included as boundary condition by Butler-Volmer relation. Figure 4.3b and 4.3c display the changes in the concentration profiles of BMEPZ, BMEPZ⁺, BMEPZ²⁺, and FL near the electrode (A-A' line for BMEPZ and B-B' line for FL in Figure 4.3a) over time as a function of the location in the microchannel for low-current and high-current density reactions, respectively. Figure 4.3b presents that the low current density prevented the second-redox reaction of BMEPZ, and BMEPZ²⁺ (red color in the figure) were not produced until the end of the simulation (108 seconds), indicating the sufficiently fast charge-transfer reaction, whereas the concentration of BMEPZ⁺ (green color in the figure) increased at the expense of BMEPZ (blue) and FL (yellow) gradually decreased. On the other hand, in the case of the high current density in in Figure 4.3c, it was found that the concentration of BMEPZ and FL decreased more drastically, implying reactants experienced excessive charge-transfer at the same given time (*i.e.*, the same flow rate). This harsh condition led to a concurrent reaction of the first- and the second-redox reactions at the one electrode, where the overall potential was displayed with the second-redox value. It is clearly shown that the pristine BMEPZ disappears rapidly upon the electrochemical reaction, and the BMEPZ⁺ was immediately produced due to the first redox reaction within 36 seconds. However, they are eventually consumed due to the second redox reaction, as indicated with the green arrow in Figure 4.2c, with the accelerated production of the BMEPZ²⁺ afterwards.

Interestingly, the concentration profile of BMEPZ²⁺ in Figure 4.3c resembled a convection-diffusion boundary layer predicted by classical diffusion-

convection theory. In this regard, we experimentally estimated the thickness of BMEPZ²⁺ concentration boundary by the image mapping of the color changes, as shown in Figure 4.3d. In the figure, four windows (i, ii, iii and iv) were selectively prepared in the electrodes so that we can directly observe the reddish boundary through the windows. Through the windows, the color gradient could be witnessed (*i.e.*, upper reddish and lower greenish regions in the inset box of the figure), implying the existence of the depletion region, which is coincident with the *in-operando* visualization in Figure 4.2c and 4.2e. Using this windowed device, we could quantitatively investigate the hydrodynamic effects by carefully extracting the approximated concentration boundaries as a function of flow rate (Q). By assuming our MFRFB has a diffusion-convection transportation without electrochemical reactions, we can employ classical diffusion-convection limit relations to characterize the concentration boundary layer versus flow velocity inside the battery cell as follows⁴¹.

$$\frac{\delta_D}{x} \sim \left(\frac{h}{x}\right)^{\frac{2}{3}} \left(\frac{D}{u_{\max} h}\right)^{\frac{1}{3}} \equiv \left(\frac{h}{x}\right)^{\frac{2}{3}} (Pe)^{-\frac{1}{3}} \quad (25)$$

where δ_D is thickness of concentration boundary layer, D is diffusion coefficient, u_{\max} is maximum velocity of electrolyte, h is height of battery cell and x is horizontal distance. Here Pe is Peclet number which represents the ratio of convective transport to diffusive transport and defined as $u_{\max}h/D$. Based on equation (1), we conducted a scaling analysis. As shown in Figure 4.3e, the experimental data at high Pe limit ($Pe = 1628$) and the theoretical prediction by equation (25) were remarkably well-

matched as a slope of 0.658, while the slopes were deviated as 0.716 at low Pe number region ($Pe = 814$). Since the convection is predominant over diffusion and electrochemical reaction at high Pe limit, one could adapt the classical diffusion-convection theory. However, the contribution of the electrochemical reaction, which can steepen the concentration gradient of reactant, becomes significant to the diffusional migration at low Pe number limit (*e.g.*, slope increased as Pe decreased). This is why the experimental results at relatively low Pe number would have good agreements with numerical simulation which rigorously considered the electrochemical reactions.

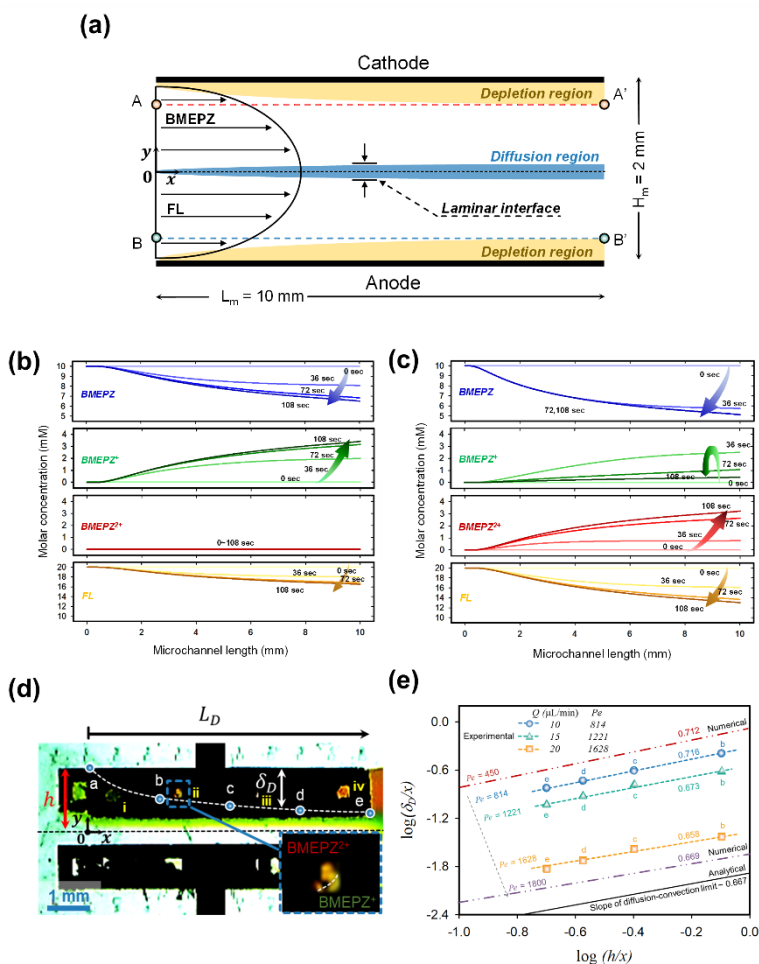


Figure 4.3. a) Schematic of MFRFB and theoretical regions that affect battery performance. b) Numerical results of concentration profiles of BMEPZ for single redox reaction. c) Numerical results of concentration profiles of BMEP for multi-redox reaction. d) Image of scaling analysis for concentration boundary layer of BMEPZ²⁺ at 10 μ L/min and 0.14 mA. e) Comparison of experimental, numerical and analytical slopes of concentration boundary layer relation.

4.3.4 Enhancing battery performance by the redesign of the electrode geometry

2-D numerical simulation and scaling analysis suggested that the depletion region would be easily developed and hinder the electrochemical redox reaction. Based on this analysis, a tapered electrode (*i.e.*, wider beginning and narrower end) has been devised over a normal electrode (*i.e.*, straight beginning and end) as shown in the insets of Figure 4.4a, considering that the shape of depletion boundary is roughly proportional to $x^{1/3}$ (x is horizontal distance). The tapered design was expected (i) to promote the reaction at the wider end of the electrode where a thinner depletion region was formed and (ii) to suppress the reaction at the narrower end where there was a thicker depletion region. In this design, even though the surface areas of tapered- and normal-electrode are kept identical, the effective electrode area becomes wider in the tapered electrode than that of the normal electrode. As shown in capacity-voltage plot (Figure 4.4a; $Q = 10 \mu\text{L min}^{-1}$ and $I = 0.1 \text{ mA}$), two distinct evidences could draw the conclusion that the tapered electrode had a superior performance to that of the normal one. Firstly, the overall over-potential was low in almost entire range of the capacity with the tapered electrode, which meant an energy efficiency was higher. Secondly, and most importantly, the tapered electrode induced the first redox reaction only (*i.e.*, green color), while the second redox reaction was witnessed with the normal electrode (*i.e.*, red color) with the same charge capacity. In other words, the reaction kinetics is more stably and effectively operated with the tapered electrode.

We believe that this kinetic analysis possible from the *in-operando* visualization would serve as the experimental platform enabling an in-depth study about electrokinetic parameters and an effective mean to optimize various types of RFBs. For example, an inevitable diffusive mixing between catholyte and anolyte is a nuisance in a membrane-free (or potentially microporous membrane) platform, thus should be minimized⁴²⁻⁴⁷. Our platform can feasibly suggest how the mixing can be regulated with respect to cell design and flow rate of the catholyte/anolyte in the cell. Figure 4.4b illustrates the criterion of required minimum flow rates for 5% mixing of the catholyte and anolyte as a function of the aspect ratio of the cell for various active-materials having different diffusion coefficients in RFBs; solid line and dotted line denote the case of BMEPZ and other reported active-materials in RFBs, respectively. As the convection of electrolytes needs to dominate over their diffusion for the physical separation of the catholyte and anolyte, the minimum flow rate should increase in proportional to the aspect ratio of cell, because the extent of diffusion increases as length of microchannel. Moreover, as the diffusion coefficient of active-material increases, a higher flow rate is required to maintain the minimum mixing of the electrolyte. When less than 5 % of mixing is allowed in the battery operation, the cell design with the flow rate should lie in the region of the left side of the solid line (as denoted with diffusion negligible in the plot) for BMEPZ catholyte. It indicates that this diagram of the correlation between the flow rate and the cell dimension can be utilized in a versatile manner for various active-materials with different requirements of the RFB design.

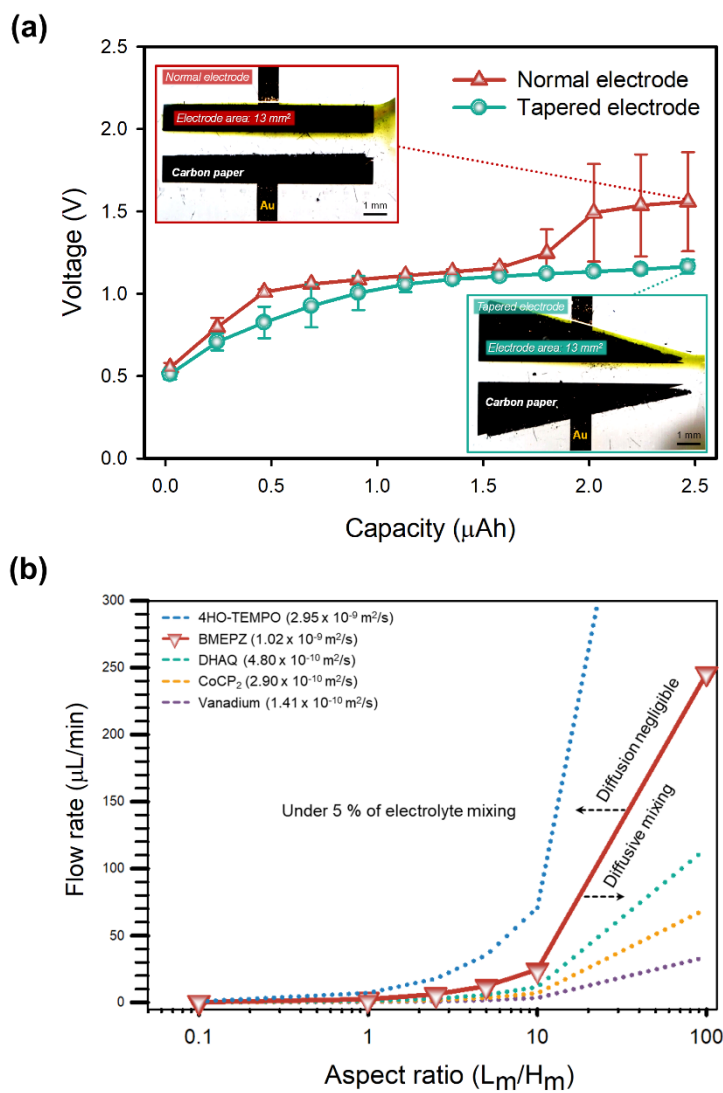


Figure 4.4. a) Comparison of electrochemical performance with respect to the geometric configuration of electrode. b) Phase diagram of required flow rate depending on the aspect ratio of cell for various active-materials in RFBs with corresponding diffusion coefficients.

4.4 Concluding remarks

We successfully demonstrated the MFRFB system that can probe the fundamental electrokinetic correlations of multi-redox ROMs for RFBs. *In-operando* visualization was demonstrated to be a powerful tool since one can directly observe the electrochemical reaction coupled with hydrodynamics. The changes in redox reactions were clearly observed in real-time for the charge- and mass-transfer rates, which are indispensable to elucidate the electrokinetic phenomena in RFBs. Moreover, combined study of 2-D numerical simulation and scaling analysis of concentration boundary layer presented the clue for the bottle-neck regions which can deteriorate the battery performance during electrochemical reaction in convective diffusion system. Based on the insights of the electrokinetic limitations in RFBs, enhanced battery performance was achieved through the redesign of electrode geometry having the tapered geometry with a larger effective electrode area. These investigations present the importance of *in-operando* analysis technique for better understanding of dynamic RFB system.

4.5 References

- 1 Badwal, S. P. S., Giddey, S. S., Munnings, C., Bhatt, A. I. & Hollenkamp, A. F. Emerging electrochemical energy conversion and storage technologies. *Front. Chem.* **2** (2014).
- 2 Larcher, D. & Tarascon, J. M. Towards greener and more sustainable batteries for electrical energy storage. *Nat. Chem.* **7**, 19-29 (2015).
- 3 Zhao, H. R., Wu, Q. W., Hu, S. J., Xu, H. H. & Rasmussen, C. N. Review of energy storage system for wind power integration support. *Appl. Energ.* **137**, 545-553 (2015).
- 4 Nguyen, T. & Savinell, R. F. Flow Batteries. *Electrochem. Soc. Interface* **19**, 54-56 (2010).
- 5 Noack, J., Roznyatovskaya, N., Herr, T. & Fischer, P. The Chemistry of Redox-Flow Batteries. *Angew. Chem. Int. Ed. Engl.* **54**, 9776-9809 (2015).
- 6 Soloveichik, G. L. Flow Batteries: Current Status and Trends. *Chem. Rev.* **115**, 11533-11558 (2015).
- 7 Park, M., Ryu, J., Wang, W. & Cho, J. Material design and engineering of next-generation flow-battery technologies. *Nat. Rev. Mater.* **2** (2017).
- 8 Winsberg, J., Hagemann, T., Janoschka, T., Hager, M. D. & Schubert, U. S. Redox-Flow Batteries: From Metals to Organic Redox-Active Materials. *Angew. Chem. Int. Ed.* **56**, 686-711 (2017).
- 9 Lee, S. *et al.* Recent Progress in Organic Electrodes for Li and Na Rechargeable Batteries. *Adv. Mater.* **30** (2018).

- 10 Morcrette, M. *et al.* In situ X-ray diffraction techniques as a powerful tool to study battery electrode materials. *Electrochim. Acta.* **47**, 3137-3149 (2002).
- 11 Lowe, M. A., Gao, J. & Abruna, H. D. In operando X-ray studies of the conversion reaction in Mn₃O₄ lithium battery anodes. *J. Mater. Chem. A* **1**, 2094-2103 (2013).
- 12 Patel, M. U. M. *et al.* Li-S Battery Analyzed by UV/Vis in Operando Mode. *Chemsuschem* **6**, 1177-1181 (2013).
- 13 Finegan, D. P. *et al.* In-operando high-speed tomography of lithium-ion batteries during thermal runaway. *Nat. Commun.* **6** (2015).
- 14 Ulvestad, A. *et al.* Topological defect dynamics in operando battery nanoparticles. *Science* **348**, 1344-1347 (2015).
- 15 Wood, K. N. *et al.* Dendrites and Pits: Untangling the Complex Behavior of Lithium Metal Anodes through Operando Video Microscopy. *Acs. Central. Sci.* **2**, 790-801 (2016).
- 16 Conder, J. *et al.* Direct observation of lithium polysulfides in lithium-sulfur batteries using operando X-ray diffraction. *Nat. Energy* **2** (2017).
- 17 Guo, J. Z. *et al.* High-energy/power and low-temperature cathode for sodium-ion batteries: in situ XRD study and superior full-cell performance. *Adv. Mater.* **29**, 1701968 (2017).
- 18 Zhao, E. W. *et al.* In situ NMR metrology reveals reaction mechanisms in redox flow batteries. *Nature* **579** (2020).

- 19 Tong, L. C. *et al.* UV-Vis spectrophotometry of quinone flow battery electrolyte for in situ monitoring and improved electrochemical modeling of potential and quinhydrone formation. *Phys. Chem. Chem. Phys.* **19**, 31684-31691 (2017).
- 20 Lawton, J. S., Aaron, D. S., Tang, Z. & Zawodzinski, T. A. Electron Spin Resonance Investigation of the Effects of Vanadium Ions in Ion Exchange Membranes for Uses in Vanadium Redox Flow Batteries. *ECS Trans.* **41**, 53-56 (2019).
- 21 Lee, J. W., Goulet, M. A. & Kjeang, E. Microfluidic redox battery. *Lab. Chip* **13**, 2504-2507 (2013).
- 22 Navalpotro, P., Palma, J., Anderson, M. & Marcilla, R. A Membrane-Free Redox Flow Battery with Two Immiscible Redox Electrolytes. *Angew. Chem. Int. Ed. Engl.* **56**, 12460-12465 (2017).
- 23 Le, T. X. H., Bechelany, M. & Cretin, M. Carbon felt based-electrodes for energy and environmental applications: A review. *Carbon* **122**, 564-591 (2017).
- 24 Goulet, M. A. & Kjeang, E. Co-laminar flow cells for electrochemical energy conversion. *J. Power Sources* **260**, 186-196 (2014).
- 25 Lee, J. W., Hong, J. K. & Kjeang, E. Electrochemical characteristics of vanadium redox reactions on porous carbon electrodes for microfluidic fuel cell applications. *Electrochim. Acta.* **83**, 430-438 (2012).
- 26 Shinkle, A. A., Sleightholme, A. E. S., Thompson, L. T. & Monroe, C. W.

- Electrode kinetics in non-aqueous vanadium acetylacetonate redox flow batteries. *J. Appl. Electrochem.* **41**, 1191-1199 (2011).
- 27 Hanapi, I. H., Kamarudin, S. K., Zainoodin, A. M. & Hasran, U. A. Membrane-less micro fuel cell system design and performance: An overview. *Int. J. Energy Res.* **43**, 8956-8972 (2019).
- 28 Ferrigno, R., Stroock, A. D., Clark, T. D., Mayer, M. & Whitesides, G. M. Membraneless vanadium redox fuel cell using laminar flow. *J. Am. Chem. Soc.* **124**, 12930-12931 (2002).
- 29 Kjeang, E., Michel, R., Harrington, D. A., Djilali, N. & Sinton, D. A microfluidic fuel cell with flow-through porous electrodes. *J. Am. Chem. Soc.* **130**, 4000-4006 (2008).
- 30 Wei, J. C., Liang, P. & Huang, X. Recent progress in electrodes for microbial fuel cells. *Bioresour. Technol.* **102**, 9335-9344 (2011).
- 31 Weber, A. Z. *et al.* Redox flow batteries: a review. *J. Appl. Electrochem.* **41**, 1137-1164 (2011).
- 32 Li, L., Bei, S. Y., Xu, Q., Zheng, K. Q. & Zheng, Y. Role of electrical resistance and geometry of porous electrodes in the performance of microfluidic fuel cells. *Int. J. Energy Res.* **42**, 1277-1286 (2018).
- 33 Deen, W. M. *Analysis of transport phenomena*. 2nd edn, (Oxford University Press, 2012).
- 34 Yan, D., Bazant, M. Z., Biesheuvel, P. M., Pugh, M. C. & Dawson, F. P. Theory of linear sweep voltammetry with diffuse charge: Unsupported

- electrolytes, thin films, and leaky membranes. *Phys. Rev. E.* **95**, 033303 (2017).
- 35 Kwon, G. *et al.* Bio-inspired Molecular Redesign of a Multi-redox Catholyte for High-Energy Non-aqueous Organic Redox Flow Batteries. *Chem* **5**, 2642-2656 (2019).
- 36 Kwon, G. *et al.* Multi-redox Molecule for High-Energy Redox Flow Batteries. *Joule* **2**, 1771-1782 (2018).
- 37 Khabbazi, A. E., Richards, A. J. & Hoorfar, M. Numerical study of the effect of the channel and electrode geometry on the performance of microfluidic fuel cells. *J. Power Sources* **195**, 8141-8151 (2010).
- 38 Tanveer, M. & Kim, K. Y. Effects of geometric configuration of the channel and electrodes on the performance of a membraneless micro-fuel cell. *Energy Convers. Manag.* **136**, 372-381 (2017).
- 39 Lisboa, K. M. & Cotta, R. M. On the mass transport in membraneless flow batteries with flow-by configuration. *Int. J. Heat Mass Transf.* **122**, 954-966 (2018).
- 40 Tanveer, M. & Kim, K. Y. Performance analysis of microfluidic fuel cells with various inlet locations and multiple compartments. *Energy Convers. Manag.* **166**, 328-336 (2018).
- 41 Probst, R. F. *Physicochemical hydrodynamics : an introduction*. 2nd edn, (Wiley, 1994).
- 42 Kjeang, E. *et al.* High-performance microfluidic vanadium redox fuel cell.

- Electrochim. Acta.* **52**, 4942-4946 (2007).
- 43 Okhonin, V., Wong, E. & Krylov, S. N. Mathematical model for mixing reactants in a capillary microreactor by transverse diffusion of laminar flow profiles. *Anal. Chem.* **80**, 7482-7486 (2008).
- 44 Krylova, S. M., Okhonin, V. & Krylov, S. N. Transverse diffusion of laminar flow profiles - a generic method for mixing reactants in capillary microreactor. *J. Sep. Sci.* **32**, 742-756 (2009).
- 45 Sprague, I. B., Byun, D. & Dutta, P. Effects of reactant crossover and electrode dimensions on the performance of a microfluidic based laminar flow fuel cell. *Electrochim. Acta.* **55**, 8579-8589 (2010).
- 46 Goulet, M. A. & Kjeang, E. Reactant recirculation in electrochemical co-laminar flow cells. *Electrochim. Acta.* **140**, 217-224 (2014).
- 47 Ibrahim, O. A. & Kjeang, E. Leveraging co-laminar flow cells for non-aqueous electrochemical systems. *J. Power Sources* **402**, 7-14 (2018).

Chapter 5. Conclusion

The increasing demand for renewable energy resources, such as solar and wind power, necessitates the development of large-scale ESSs. Flow batteries are believed to be the battery technology with the greatest potential to be one of the key elements in the energy transition to a sustainable electricity supply. However, the current state of inorganic-based RFB technology represent only an intermediate step facing various issues such as high cost and the generation of toxic substances, which somewhat restrains the widespread application. For the development of next-generation RFB systems, relying on ROMs is inevitable because of their diversity, cost-effectiveness, and chemical tunability, and thus global research effort is vigorously arising to develop high performance ORFBs for the practically feasible system. Since the research of ORFB is still infancy, the systematic research approach is highly required from ROM design with high electrochemical performance such as energy density and stability to the fundamental study dealing with fluid dynamics.

As a first step for the systematic development of high performance ORFBs, I focused on exploring and designing a novel redox-motif to effectively increase energy density, which is regarded as the most critical battery property. Even though energy density in RFB can be increased by simply elevating the concentration of redox-active materials, the physical properties of electrolytes such as viscosity are generally negatively affected by the concentration. In this regard, exploration of a basic redox motif having the high molar energy density is significantly critical in the

practical system. Inspired by the energy transduction in bio-system, multi-electron redox phenazine molecule, DMPZ, was successfully redesigned and introduced into RFB system and verified its great potential of developing the high energy density ORFBs. Furthermore, by utilizing the unique advantage of organic materials, highly soluble version of DMPZ, denoted BMEPZ, was rationally synthesized and evaluated in flow cell system, which provides a breakthrough to catch up with or outperform the conventional RFBs.

In addition to the energy density, as a next step, chemical stability of ROM was investigated, which critically affects the long-term cycling performance of ORFBs. Highly reactive organic substances (*e.g.* radical species) is prone to be exposed to various unwanted reaction with electrolytes or other redox-active materials, and thus the rational approach of molecular design to prevent such side reaction is highly demanded. Based on the knowledge of charge delocalization effect on the chemical stability of organic materials, I studied TPA motif due to its largely conjugated skeleton preventing the high charge population on a few specific atoms. 3MTPA was designed and successfully synthesized to offer the further chemical stability and solubility of TPA. Comparative study using representative ROMs reported in ORFBs revealed the superior chemical stability of 3MTPA even in the high temperature condition. These finding on developing the highly persistent ROM can offer great intuition for the demonstration of durable ORFBs.

For the demonstration of high performance ORFBs, understanding fundamental aspects of electrochemical reaction occurring battery operation is

crucial as well. In particular, unlike solid-state battery system, RFB is a dynamic system where the electrolytes keep flowing, and thus simultaneous consideration of electrochemistry and fluid dynamics is highly required. To directly observe the electrochemical reaction occurring at the electrodes in real-time, a custom microfluidic cell fabricated using the transparent PDMS was utilized. *In-operando* visualization was successfully demonstrated using microscopic technique with novel ROM showing reversible color change. Observation of different redox behavior was visually presented depending on the charge- and mass-transfer, and implication of such kinetics on electrochemical performance was carefully studied. Moreover, it was confirmed that the cell geometry is highly critical in battery performance through scaling analysis of convective-diffusion model supported by the numerical simulation.

In this dissertation, I suggested multidisciplinary research strategy of developing high performance ROMs and in-depth understanding of the system with the aim of developing high performance ORFBs. Although the research on ORFBs is currently infant stage and there are still remaining challenges for the practical application, I hope this dissertation contributes to the demonstration of next-generation ESSs and provide strong research insight for scientific understanding of ORFB.

국 문 초 록

화석 연료 사용으로 인한 환경 문제로 인해, 지속 가능한 에너지 자원에 대한 꾸준히 증가하는 수요는 현재까지 세계적인 큰 관심사 중 하나가 되고 있다. 그러나 해당 자원의 간헐적인 에너지 공급은 자원의 효율적인 활용을 상당히 제한하고 있으므로, 대규모 에너지 저장 시스템은 이를 보완하고 상시 이용을 위해 필요하다. 많은 에너지 저장 장치 중 액체 전해질을 활용한 레독스 흐름 전지는 액체 전지 라는 차별화된 시스템으로 인해 큰 주목을 받고 있다. 전해질 저장소와 배터리 셀의 공간적 분리를 통해 전력과 에너지를 분리하여 설계가 가능하기 때문에, 필요에 따라 스케일을 유연하게 제어 할 수 있다. 따라서 대용량 에너지 저장장치 용으로 레독스 흐름 전지 분야에서 상당한 연구 개발이 이루어지고 있다.

특히, 레독스 흐름 전지 용 산화 환원 활성 물질에 대한 연구는 배터리 성능에 큰 영향을 미치기 때문에 매우 중요하다고 여겨진다. 이와 관련하여, 철/크롬 산화 환원 커플을 시작으로 다양한 종류의 산화 환원 활성 물질이 지난 수십 년 동안 광범위하게 연구되어오고 있다. 대표적으로 바나듐 및 징크/브롬 기반 산화 환원 활성 물질은 연구 분야에서 큰 가능성을 보였으며, 실제 응용 분야에서도 사용되고 있다. 그럼에도 불구하고 이러한 무기 재료 기반의 산화 환원 활성 물질의 사용은 환경 문제와 비용 문제라는 현실적인 한계점을 가지고 있다. 또한 이론적 한계 (즉, 제한된 용해도 및 산화 환원 전위)에 거의 도달한 상태이므로, 차세대 고성능 레독스 흐름 전지 개발을 위해 새로운 산화 환원 물질의 개발 및 도입이 절실히 필요하다. 이런 시점에서, 레독스

흐름 전지의 산화 환원 물질 개발에 대해 지속 가능하고 환경 친화적인 유기물 활물질에 관심이 집중되고 있다.

레독스 흐름 전지 용 유기물 활물질은 기존 활물질들과 차별화된 장점을 가지고 있다. 유기물 활물질은 주로 탄소, 수소, 산소 및 질소와 같은 지구에 풍부한 원소로 구성되어 있기 때문에 잠재적으로 비용 측면에서 효율적이고 환경친화적이다. 또한 용해도 및 산화 환원 전위와 같은 다양한 물리적 특성을 조정하는 것 역시 유기 합성을 통해 가능하다. 이런 점에서, 레독스 흐름 전지 용 활물질 선택의 다양화와 고성능 전지 개발에 대한 큰 가능성을 가지고 있다. 하지만, 다양한 장점에도 불구하고 유기물 활물질에 대한 연구는 초기 단계이며 전지 성능은 아직 기존 레독스 흐름 전지에 비해 뒤떨어져 있다.

따라서, 기존 시스템에 비해 더 우수한 성능을 가지면서 최종적으로 상용화가 되기 위해서는 새로운 유기물 활물질을 설계하는 체계적인 연구가 필요하다. 이 학위 논문에서는, 새로운 유기 활물질을 활용하여 전지 성능을 향상시키는 다차원적인 전략을 주요 주제로 다루고 있다. 먼저, 바이오 시스템에서 영감을 받아, 효과적인 방법으로 높은 에너지 밀도를 달성하기 위한 다중 산화 환원 유기물질을 설계하고 레독스 흐름 전지에 도입하였다. 단일 전자 산화 환원 반응만 가능한 기존 물질들과 달리, 다중 산화 환원 분자를 사용하면 주어진 농도에서 두 배 이상의 용량 발현이 가능하다. 이는 체계적인 분석을 통해 레독스 흐름 전지에 성공적으로 적용 됨이 입증되었다. 나아가, 유기 합성을 진행하여 용해도 향상도 성공적으로 이끌어 내었으며, 이를 통해 실제 상용화 측면에서도 큰 가능성을 보여주었다. 또한, 수명 특성 측면에서, 많은 공명 구조를 가지며 넓은 전하 분포를 가지는 유기물 활물질을 설계하는 전략을 바탕으로 고수명 유기물 레독스 흐름 전지 개발에 대한 가능성을 확인하였다. 마지막으로, 실시간 시각화 기술을 도입하여

유기물 레독스 흐름 전지의 전기 화학 반응에 대한 기초 연구를 수행하였다. 이 학위 논문에서 진행된 유기물 레독스 흐름 전지의 설계 전략에 대한 심층적 이해를 토대로, 본 연구는 고성능 유기물 레독스 흐름 전지 개발에 대한 가이드 라인을 제시하며 해당 연구 영역을 광범위하게 확장 할 수 있는 연구적인 통찰력을 제공해 줄 것이다.

주요어: 이차 전지, 레독스 흐름 전지, 산화 환원 유기물, 유기물 레독스 흐름 전지, 전기 화학

학 번: 2016-20765